受入
89-5-52
高工研図書室

EUROPEAN ORGANIZATION FOR NUCLEAR RESEARCH

CERN-EP/89-47
29 March 1989

JET PHYSICS AT THE CERN INTERSECTING STORAGE RINGS

Vincenzo Cavasinni

Dipartimento di Fisica, Università degli Studi di Pisa,
Istituto Nazionale di Fisica Nucleare, Pisa, Italy
and
CERN, Geneva, Switzerland

ABSTRACT

Here we review the most relevant physics results obtained at the CERN Intersecting Storage Rings (ISR) when studying the hard interactions between beam-particle constituents and their subsequent fragmentation into hadrons (Jet Physics). The main emphasis is on the results obtained in the 1980s. Whenever possible the measurements at the ISR will be compared with the data of the CERN and Fermilab Colliders, at energies up to thirty times as large. The direct comparison of results from different initial-state particles (proton–proton, antiproton–proton, light ions) was a unique feature of the ISR, and one that can provide a deeper insight into the elementary interaction mechanisms.

(To appear in La Rivista del Nuovo Cimento)

1. THE BIRTH OF THE LARGE-p_T PHYSICS—A HISTORICAL SURVEY

The first observation of the departure of the transverse momentum (p_T) single-particle distribution from the thermal spectrum [$E(d\sigma/dp^3) \approx \exp(-bp_T)$; $b \approx 6\ GeV^{-1}$], which is indicative of the emergence of a scattering '*à la* Rutherford', was reported in 1972 by three experiments working independendly at the CERN Intersecting Storage Rings (ISR)[1-3]. An example is shown in Fig. 1 for the π^0 production at the five ISR energies. The large-p_T spectrum exhibited two salient features:

i) for $p_T \sim 1$ GeV/c, the π^0 yield is well above the solid line, which represents the exponential behaviour extrapolated from low p_T;

ii) in contrast to the negligible $\sqrt{s}$ dependence of the distribution at low p_T, the large-p_T yield increases with energy, and even more so with larger p_T. This feature is shown more dramatically in Fig. 2, where the inclusive π^0 production, as measured at the ISR [4], is compared with that measured by the UA2 Collaboration experiment at the CERN $p\bar{p}$ Collider at an energy one order of magnitude higher [5].

This historical result suggested that the large-p_T particle production took place through an interaction between point-like elementary constituents of the proton (similar to the Rutherford scattering) that could not be of an electromagnetic nature as formerly proposed by Berman, Bjorken and Kogut [6], but the large value of the ISR cross-section suggested that this interaction was mediated by the strong force.

The parton model [7] constituted a first fruitful framework for interpreting the large-p_T phenomena: the wave function of the colliding hadrons is the sum of subfields—the partons—weakly interacting with each other. At high-p_T, the reaction occurs through a hard binary collision of partons, with a subsequent fragmentation of both the struck (active) partons and those not directly involved in the hard collision (spectators). Since the interaction time of the hard scattering is much less than the time scale of the initial-state weak interaction among partons and of the final-state hadronization (impulse approximation), the three steps of the process could be assumed to factorize.

The ingredients of the process are shown schematically in Fig. 3. The structure function $F_{Aa}(x)$ [$F_{Bb}(x)$] gives us the probability that a parton a (b) could be found in a hadron A (B) carrying a fraction x of its momentum; $d\sigma/d\hat{t}$ is the elementary cross-section for the interaction between a and b ($\hat{s}$, $\hat{t}$, $\hat{u}$ are the Mandelstam variables in the hard subprocess); and G_{cC} (z, Q_T) describes the probability that parton c, in its hadronization, yields a particle C with longitudinal momentum fraction z and transverse momentum Q_T relative to the parent parton. The Lorentz-invariant cross-section for the inclusive production of particle C can be expected to scale as

$$E\frac{d\sigma}{dp^3}[A + B \rightarrow C + X] = \frac{K}{p_T^N} f(x_T, \theta) \ , \qquad (1)$$

where $x_T = 2p_T/\sqrt{s}$, and θ is the emission angle. The partons are assumed to be point-like, and the only momentum scales in the problem are (neglecting the masses of hadrons) p_T and $\sqrt{s}$, and for dimensional arguments one expects to have $N = 4$ (as in the Rutherford scattering).

These relatively simple ideas stimulated a large amount of successful theoretical and experimental work, most of which was performed at the ISR, with the aim to shed light on each of the three steps contributing to the large-p_T production. Several questions were raised:

- Does the experimental observation that $N = 8$ (for meson production), instead of 4, indicate that the scattering process did not (or not yet) probe the elementary constituents, but rather some more composite fields? (scattering parton-meson, as suggested by the CIM model [8]).
- Do the structure and the fragmentation functions depend also on Q^2, the squared momentum transfer released in the hard process? (scaling violations).

- Can the structure functions be taken directly from the measurements performed in lepton deep-inelastic scattering?

Quite early on, it was realized that it was important to study, in association with the single-particle yield, the characteristics of the whole collimated bunch of hadrons (a jet) that emerges from the fragmentation of the struck partons, both in the hemisphere of the large-p_T trigger particle (toward jet) and in the opposite one (away jet). First proof of the existence of jets correlated with the large-p_T trigger particle came in the middle 70s [9]. During the same period, other important experimental support for the existence of jets came from the SLAC storage ring, SPEAR, where jet-like structures were found in the hadronic final states produced in high-energy electron-positron annihilation [10].

Triggering with large-p_T single particles as originally done at the ISR introduced also another effect, known as the 'trigger bias' [11]. This effect arises from competition between the fragmentation frunction G(z) and the steeply falling p_T spectrum of the parton (jet). Because of the falling cross-section for any given p_T, it is cheapest to produce the trigger particle with a p_T as close as possible to the p_T of the jet; owing to the fact that also G(z) is a rapidly falling function of z, these fragmentations are very rare and these events represent only a small fraction ($\leq 1/100$) of the total number of events with a jet of a given p_T — hence the necessity of designing experiments with efficient trigger possibilities for jets rather than for single particles only.

We remind the reader of the already existing excellent reviews of large-p_T physics performed at the ISR in the 70s [12–14]. However, here we prefer to cover the results obtained at the ISR in the last five years of data-taking. During this period, the consolidation of the theoretical framework [quantum chromodynamics (QCD)], the exploitation of more powerful and dedicated detectors, and finally the competition of the CERN Collider — allowed the ISR to give important contributions in hard-collision physics.

Before reviewing the results, we shall introduce in the next section the fundamental elements of QCD in order to assess the proper language for discussing the experimental data.

2. THE QCD APPROACH

Although the parton model was used very successfully in many qualitative predictions, it is today generally recognized that it must be considered as a first-order approximation of a more complete gauge-invariant field theory of the strong interactions: the QCD. For example this theory can answer the questions posed in the previous section. Here we will recall only the basic elements of QCD, and refer the interested reader to more specialized papers [15].

In QCD, the constituents of hadrons (quark and gluons) carry a new quantum number (colour) in addition to the quantum numbers that are relevant to electroweak interactions, spin, isospin, and charge (flavour). The quarks, which carry fractionary charge (2/3 and 1/3 *à la* Gell-Mann and Zweig), are supposed to exist in colour triplets and obey the group of symmetry SU(3). Ordinary hadrons must have zero net colour, i.e. $q\bar{q}$ (mesons) and qqq (baryons) wave functions must be colourless singlet states. Strong interactions between coloured quarks are mediated by an octet of coloured vector fields — the gluons — which do not carry flavour. In contrast to quantum electrodynamics (QED), the non-Abelian character of SU(3) allows Feynman vertices to exist between gluon and gluon, in addition to the quark–quark and quark–gluon ones. The strength of all the interactions between quarks and gluons is specified by just one universal coupling: α_s. The gluon self-coupling is mainly responsible for the 'asymptotic freedom', a unique feature of non-Abelian local-gauge theories, which means that the interaction strength α_s becomes smaller as the distance d between two quarks lessens [or as Q^2 becomes larger: $d \approx 1/\sqrt{Q^2}$); for $Q^2 \to \infty$, the theory becomes a free field-theory (in contrast to QED)]. The explicit dependence of α_s on Q^2 can be calculated using the so-called 'leading log approximation' (LLA) [15], and is expressed as $\alpha_s = 12\pi/(33 - 2N_F) \times$

$\log(Q^2/\Lambda^2)$, where N_F is the number of flavour families of quarks; Λ is the only free parameter in the theory; it has to be fixed by experiment by measuring the α_s dependence on Q^2. From the expression for α_s, we see that at large Q^2 ('large' being determined by Λ), α_s becomes small, and perturbative techniques can be applied (perturbative QCD). On the contrary, at low Q^2 the strong interaction is indeed strong, and a perturbative analysis cannot be performed—for example, in the case of the interaction binding quarks inside hadrons (non-perturbative QCD). This permits also a crude estimate of Λ: we know that at distances equal to the typical dimension of the proton r_p, the coupling must be large, i.e. for $Q^2 \approx \langle r_p^2 \rangle^{-1} \approx (0.8\ \text{fm})^{-2} \approx (0.3\ \text{GeV})^2$. Therefore $\Lambda^2 \approx 0.3\ \text{GeV}^2$, and indeed this value is not far from the experimental determination [16].

At first order in α_s, quarks (q) and gluons (g) can interact through eight fundamental processes:

Process		$\lvert M\rvert^2\ (\theta^* = 90°)$
$q_iq_i \to q_iq_i$		3.26
$q_i\bar{q}_i \to q_i\bar{q}_i$		2.59
$q_i\bar{q}_i \to gg$		1.04
$q_i\bar{q}_i \to q_j\bar{q}_j$	$(i \neq j)$	0.22
$q_iq_j \to q_iq_j$	$(i \neq j)$	2.22
$q_i\bar{q}_j \to q_i\bar{q}_j$	$(i \neq j)$	
$gg \to q_i\bar{q}_i$		0.15
$q_ig \to q_ig$		6.11
$gg \to gg$		30.38

(2)

The QCD cross-section for the above elementary α_s^2 processes is well known [17], and can be expressed as

$$d\sigma/d\cos\theta^* = \pi\alpha_s^2/2\,\hat{s}|M|^2\ , \tag{3}$$

where θ^* is the scattering angle, and $\hat{s}$ is the square of the total energy in the centre of mass of the two partons, and M is the amplitude of the process. To understand the relative importance of the various processes, we have listed in processes (2) also the numerical value of $|M|^2$ at $\theta^* = 90°$. It is evident that terms involving initial gluons are dominant whenever the gluon density in the incident hadron is comparable to that of quarks. This occurs at small values of Q^2/s, such as those accessible with the luminosities obtainable at the CERN and Fermilab Colliders. In contrast, the ISR—thanks to its higher luminosity—could get data at transverse momenta near to the phase-space limit and thus explore the physics of quark–quark interactions. Higher-order α_s corrections, still yielding two partons in the final state, are also present. In the leading-order approximation [15], all such corrections containing powers in $\alpha_s \ln(Q^2)$ are summed, and their contribution can be incorporated as a Q^2-dependence of the structure function, i.e. $F(x) \to F(x,Q^2)$. 'Non-leading order' terms are difficult to calculate, and they are referred to as corrective factors (K-factors, $K \leq 2$) [18].

Subsequent to the QCD interaction, coloured quarks and gluons fragment into the observed jets of colourless hadrons, and this is a soft process in which perturbative QCD is not applicable.

QCD results can be expressed in a revised parton-model language as follows:

i) the structure functions are not only functions of (x) (scaling), they depend also on Q^2; in LLA this dependence is determined by a Q^2 evolution equation for the structure functions [19];

ii) also the fragmentation function G(z) is affected by higher α_s contributions that depend on Q^2 of the probing current. Hence $G(z) \to G(z,Q^2)$, obeying an evolution equation similar to that of the structure function [20].

The QCD theoretical framework, although promising, does not have very restrictive predictions (K-factors, etc.). It is the task of experiments to provide more inputs to theory. We shall discuss what the ISR contribution has been in this respect.

3. JET TRIGGER STUDIES

Direct measurements of jets were performed at the ISR by two experiments, which were able to trigger on the transverse-energy deposition in electromagnetic and hadronic calorimeters with a large enough solid angle with respect ot the jet size and sufficient isolation from the beam fragmentation. The experiment of the Axial Field Spectrometer (AFS) Collaboration was equipped with a uranium–copper calorimeter with full azimuthal acceptance, arranged in a square structure (Fig. 4) that allowed a pseudorapidity (η) coverage varying with azimuth between $|\eta| < 0.7$ and $|\eta| < 1.2$. The detector could benefit from the excellent energy resolution of the uranium calorimeter, $\sigma(E)/E = 16\%/\sqrt{E}$ for electromagnetic showers and $37\%/\sqrt{E}$ (E in GeV) for hadronic showers, together with good granularity. The detector also featured good track capability.

The CCOR*) experiment (see Fig. 5) was equipped with a superconducting solenoid enclosing a system of cylindrical drift chambers. Four azimuthal modules of lead/scintillator shower counters were located inside the magnet. The detection of electromagnetic showers was completed by two left–right lead-glass walls located outside the magnet. The r.m.s. energy resolution for the lead-glass and the shower counter was $(4.3/\sqrt{E} + 2)\%$ and $16\%/\sqrt{E}$ (E in GeV), respectively. This apparatus ideally measures energy coming only from particles giving electromagnetic showers, mainly π^0's.

A first evidence for jet production, using a technique that was free from instrumental biases, was obtained by UA2 at the CERN $p\bar{p}$ Collider [21]. The observed total transverse energy (ΣE_T) distribution measured by the UA2 calorimeter (Fig. 6) shows a clear departure from an exponential when ΣE_T exceeds 60 GeV [22].

An investigation of the pattern of energy distribution in the events was also carried out by UA2 by tagging clusters of energy deposition in each event, and by ordering them in decreasing transverse energies ($E_{T1} > E_{T2} > E_{T3}$). Figure 7 shows the mean values of the fractions $h1 = E_{T1}/\Sigma E_T$ and $h2 = (E_{T1} + E_{T2})/\Sigma E_T$ as a function of ΣE_T. As ΣE_T increases (i.e. for $\Sigma E_T > 60$ GeV), a very substantial fraction of ΣE_T is shared, on the average, by two clusters with roughly equal transverse energies. These energy clusters appear to be associated with collimated multiparticle systems, as was found by reconstructing the charged-particle tracks in these events.

At the ISR, disclosing directly jets in large-ΣE_T events was more difficult owing to the lower energy. The ΣE_T region where jet–jet events were found to become dominant at the SPS Collider ($\sim$ 60 GeV) is just the end of phase space at the ISR. The onset of dijets is at lower transverse energy, but the effect is relatively less and less important with decreasing ΣE_T. The CCOR Collaboration measured the total E_T distribution for neutral particles (ΣE_T^0) at $\sqrt{s} = 62.3$ GeV [23], as shown in Fig. 8. The spectrum deviates from a simple exponential above $\Sigma E_T^0 \approx 20$ GeV, indicating that the transverse energy at which the transition to the jet regime occurs depends on $\sqrt{s}$.

Figure 9 shows the distributions of ΣE_T measured by the AFS at $\sqrt{s} = 30$, 45, and 63 GeV [24]. Here the spectra are consistent with an exponential fall-off up to $\Sigma E_T \sim 40$ GeV. The AFS experiment studied also the event shape, by means of the parameter called circularity (C) [24]. For each event the momentum tensor, made up of the contribution of the transverse momentum of each energy cluster in the calorimeter, is diagonalized. The parameter C is calculated from the eigenvalues A and B ($A > B$) as $C = 1 - [(A-B)/(A+B)]$; $C = 1$ for circular (non-jet events), $C = 0$ for

*) Over the years, the composition of this Collaboration has changed according to the participating Institutes, and has had other slightly different names such as COR, CMOR, and BCMOR.

perfect pencil-like events. Figure 10 shows the C-distribution at $\sqrt{s}$ = 30, 45, and 63 GeV and for different total E_T bins. At these three energies, the C-distribution depends only slightly on E_T for E_T < 25 GeV; it is only when E_T > 25 GeV that the fraction of events with low circularity increases strongly with increasing E_T. This effect is hardly recognizable at $\sqrt{s}$ = 30 GeV, but at $\sqrt{s}$ = 45, and especially at $\sqrt{s}$ = 63 GeV, the peak at low C for E_T > 25 GeV is evidence of jet-like events. Figure 11a shows the average value of C versus ΣE_T at the three energies; in Fig. 11b the quantity $\Sigma E_T/\langle p_T \rangle$ is plotted, where $\langle p_T \rangle$ is the average transverse momentum of particles measured in the drift chamber. This quantity is proportional to the particle multiplicity of the event. From Figs. 11 we see that the mean value of C is constant within errors, despite the increasing multiplicity, up to ΣE_T = 25 GeV, where it starts decreasing strongly. The event multiplicity for ΣE_T > 25 GeV remains constant, resulting in higher-p_T particles. From Figs. 10 and 11 one may understand why the large-acceptance calorimeter experiments to search for jets, performed at the CERN SPS [25] and at Fermilab [26], gave negative results: they explored E_T regions in which the contribution of normal (non-jet) events is much larger than the hard-jet contribution.

An analysis similar to that performed by UA2 (Fig. 7) was made at the ISR by the COR and AFS Collaborations. Figure 12a shows the fraction of ΣE_T^0 in the two largest clusters, and in the largest cluster measured by COR [23] at $\sqrt{s}$ = 63 GeV. The fraction of events with more than 60% of their ΣE_T^0 in two non-overlapping regions of Δy = 1 and $\Delta\phi$ = 60° is shown in Fig. 12b [24]. From both Fig. 12a and Fig. 12b we see a clear two-jet dominance at high E_T.

4. INCLUSIVE JET PRODUCTION

The single-jet inclusive cross-section was measured at the ISR by the ASF Collaboration [24, 27]. The jet cross-section was extracted by analysing the shape of the thrust distributions, as shown in Fig. 13. The thrust (T) of the event was defined as

$$T = \sum^{N} |\vec{E} \cdot \vec{p}_i| / \sum^{N} |\vec{p}_i| \ , \tag{4}$$

where $\vec{E}$ is the versor (i.e. the vector of unit length) obtained by summing all the momenta of the N reconstructed clusters, and $\vec{p}_i$ is the momentum of each individual cluster. In Fig. 13 we see that the contribution of a single jet (shaded area) to the total thrust distribution increases steadily as ΣE_T increases. This is similar to the effect seen in Fig. 11. The jet cross-section is extracted from Fig. 13 with the help of a QCD-based Monte Carlo, and is plotted in Fig. 14 for $\sqrt{s}$ = 45 and 63 GeV. As a comparison, Fig. 14 shows also the yield of inclusive π^0 at $\sqrt{s}$ = 63 GeV. At $\sqrt{s}$ = 63 GeV, the jet/π^0 ratio increases from about 200 to about 1500 as p_T goes from 6 to 14 GeV/c. Superimposed on Fig. 14 are also the jet cross-sections predicted by a QCD calculation [28] that uses the single-parton effective structure function as parametrized by Bayer et al. [29] and jet fragmentation functions according to the Feynman–Field model [30]. The agreement between QCD and data is good; in particular, the theoretical model reproduces well the growth of the cross-section at a given p_T as the c.m. energy increases. This effect is more spectacularly visible in Fig. 15, which reports the jet cross-sections at $\sqrt{s}$ = 63 [24, 27], 540 [21, 22], and 1800 GeV [31]. The dashed curves are the QCD predictions of Horgan and Jacob [32] prior to both the CERN Collider and the ISR data; the dashed-dotted curve is the QCD prediction at $\sqrt{s}$ = 1800 GeV. Also shown in Fig. 15 is a band of QCD predictions at $\sqrt{s}$ = 540 GeV (solid lines), which illustrates the theoretical uncertainty given mainly by the choice of structure functions and Q^2 scale; a similar theoretical uncertainty holds also at $\sqrt{s}$ = 1800 GeV. In spite of these uncertainties, the agreement between data and theory is remarkable, considering that the theory describes data more than one order of magnitude different in c.m. energy and spanning seven orders of magnitude in cross-section size.

Ignoring the Q^2 dependence of the structure functions and of α_s (naïve parton model), the invariant jet cross-section should obey the scaling relation

$$E \frac{d\sigma}{dp^3} = A p_T^{-N} f(x_T) , \tag{5}$$

with $x_T = 2p_T/\sqrt{s}$ and $N = 4$. This comparison is made in Fig. 16a, where data taken at the ISR ($\sqrt{s} = 45$ and 63 GeV) [27] and at the CERN Collider ($\sqrt{s} = 540$ and 630 GeV) [33] are compiled. From Fig. 16a we see that the naïve scaling expectation is not confirmed, as expected. A best fit of the form

$$E \frac{d\sigma}{dp^3} = p_T^{-N} f(x_T), \quad f(x_T) = A(1 - x_T)^m/x_T^2 \tag{6}$$

gives $N = 4.74 \pm 0.06$, $m = 6.54 \pm 0.15$, and $A = (8.3 \pm 0.4) \times 10^{-27}$ [33]. The inclusive cross-sections scaled with $N = 4.74$ are shown in Fig. 16b. This empirical scaling law is well satisfied. The deviation of N from 4 can be well accounted for by scaling-violation effects in the structure function.

5. DIRECT-PHOTON PHYSICS

If in a QCD diagram one of the strong couplings is replaced by the electromagnetic one, a direct photon can be produced, instead of a jet. The lowest-order QCD contributions are sketched in Fig. 17. QCD calculations at the leading order have been performed [34] and also next-to-leading order calculations are available [35]. In these interactions, the event picture is simplified since one of the two final jets is just a single particle (the photon). Of course, one has to pay for this advantage with production cross-sections that are much lower (by 10^{-3}–10^{-4}) than that of a hadron jet at the same p_T.

The major experimental problem when measuring direct photons is to distinguish them from γ's originating from the decay of π^0/η particles. At the ISR, two methods were employed: i) experiments R806 and R807 [36] could resolve the $\pi^0 \to \gamma\gamma$ process directly by means of a liquid-argon calorimeter with fine granularity; ii) instead, experiment R108 (CCOR Collaboration) [37] exploited the fact that the single direct γ has a conversion probability lower than that of the γ pair from π^0 decay. The study of the non-conversion probability of a sample of events allows to derive the fractions of direct γ's. Figure 18a shows the observed ratio γ/π^0 as a function of p_T at $\sqrt{s} = 63$ GeV measured by experiment R806; Fig. 18b shows a similar result obtained by experiment R108 at $\sqrt{s} = 44.8$ and 62.4 GeV. In both cases we observe the onset of a clear signal of direct photon production when p_T increases.

In addition to the processes shown in Fig. 17, there could be (again of order α_s) a competing contribution from the electromagnetic bremsstrahlung of a scattered quark. These events should be signalled by the existence of a jet which accompanies the photon. This contribution was measured at the ISR by experiment R807 [38] and was found to be small.

The relative contribution of the two dominant processes can be determined by comparing direct-photon production in antiparticle and particle beams. At intermediate x-values, $q\bar{q}$ annihilation dominates in $p\bar{p}$ interactions, while gq Compton scattering dominates in pp ones. This investigation was performed at $\sqrt{s} = 53$ GeV by the AFS experiment, by comparing direct photon cross-sections in pp and $p\bar{p}$ collisions [39]. Figure 19 shows the experimental results together with QCD predictions. A statistically significant difference between γ production in pp and $p\bar{p}$ collisions is not visible, however the predicted effect is modest and the data errors are large. As a consequence, the results are in reasonable agreement with QCD.

The measurement of the double inclusive cross-section for high-p_T prompt photons accompanied by an opposite-side hadron jet allows a determination of x_1 and x_2 of the two incoming partons. Under the assumption that the prompt-photon production is dominated by the gluon Compton process (in pp), the determination of the gluon structure function becomes possible since the quark structure function is known. This analysis was performed by the AFS Collaboration [40]. The resulting gluon structure function is shown in Fig. 20 and compared with the equivalent structure function measured in deep-inelastic scattering experiments [41]: it is clear from this figure that one finds a softer gluon distribution from direct photon data than in deep inelastic scattering.

Figure 21 summarizes the measurement of direct-photon inclusive cross-sections at the ISR [36–39]. The experimental data are compared with a QCD calculation up to next-to-leading order in α_s [42]: different curves are obtained with different gluon structure functions [42].

Scaling-violation effects can be investigated by comparing single-photon inclusive cross-sections at different c.m. energies as a function of the scaling variable $x_T = 2p_T/\sqrt{s}$. This is done in Fig. 22a, which shows the scaled inclusive cross-sections $p_T^4[E(d\sigma/dp^3)]$ in $p\bar{p}$ interactions at $\sqrt{s} = 24.3$ GeV [43], 53 GeV [39], and 630 GeV [44]. Figure 22a clearly exhibits the effect of scale breaking in the structure functions, similar to what is observed in inclusive jet production. Again we can parametrize this effect using the form

$$E(d\sigma/dp^3) = p_T^{-N} f(x_T) \ , \tag{7}$$

where the departure of N from 4 is a measure of the size of the scale breaking. We may retain the ansatz $N = 4.74$ taken from jet production, and in Fig. 22b we present the scaled cross-section with $N = 4.74$. Within the errors, the $p\bar{p}$ data at the three energies appear to be described by a universal curve, suggesting that a similar scale-breaking mechanism is at work for both jet and γ production.

6. TWO- AND THREE-JET FINAL STATES

The dijet cross-section $d\sigma/dmd\eta_1 d\eta_2$ at $\eta_1 = \eta_2 = 0$ at $\sqrt{s} = 63$ GeV, where m is the invariant mass of the dijet system and η_1, η_2 are the pseudorapidities of the two jets, is presented in Fig. 23 [45]. The curves in this figure represent leading-order QCD calculations of the cross-section, with two sets of structure functions parametrized by Duke and Owens [46]. Again, the agreement between the data and the theoretical calculations is good, both in shape and in absolute magnitude.

The distribution in relative azimuthal angle between the two jets is shown in Fig. 24 [23] for neutral-jet E_T in the range 26–30 GeV. The back-to-back nature of the two jets is evident, and the width of the distribution is indicative of the imbalance of p_T carried by the two colliding partons.

In QCD the term next to the two-jet final state could give rise to three-jet final states in which a gluon has been radiated. The observation of this effect is a crucial test of the theory. Gluon radiation was investigated in e^+e^- experiments as well as in hadron–hadron collisions. In lowest-order QCD the strength of the $2 \to 2$ and $2 \to 3$ processes is α_s^2 and α_s^3, respectively. Thus the relative 3-jet yield allows a determination of the strong-coupling constant. With this procedure the systematic uncertainties in the structure functions will largely cancel. This study was made at the CERN $p\bar{p}$ Collider by experiments UA1 [47] and UA2 [48], and at the ISR by the AFS [49] and CMOR [50] Collaborations. The most important condition is that events must be sampled at the same subprocess energy. This is a very critical point at the ISR because the total jet-E_T spectrum falls very steeply. Moreover, using Monte Carlo calculations, one has to take into account, as well as possible, the efficiency of the experimental algorithm for defining a jet, the contribution to the jet E_T coming from particles belonging to the underlying event, and so on. For a three-jet event, after a transverse boost to obtain zero transverse momentum, the AFS Collaboration defines the Dalitz variables x_1, x_2, x_3 as:

$$x_1 = 2p_{T1}/\Sigma p_T \; ; \quad x_2 = 2p_{T2}/\Sigma p_T \; ; \quad x_3 = 2p_{T3}/\Sigma p_T \; ; \quad \text{and} \quad x_1 > x_2 > x_3 \; .$$

At a given ΣE_T, the structure of a three-jet event (in the transverse plane) is described by two dimensionless numbers, say x_1, x_2, or x_3, and ω, the angle between the second and the third jet in the transverse plane. Figure 25a shows the Dalitz plot of three-jet events. Only those with $x_3 > 0.25$ and $\omega > 40°$ are included. Figure 25b gives a survey of the geometry of three-jet events. A class of so-called 'star' 3-jet events, with $x_3 \geqslant 0.40$ and $\omega \geqslant 60°$ is also defined. Figure 25c is the Dalitz plot for the full Monte Carlo sample with the three-jet events included, whilst Fig. 25d is obtained by excluding the three-jet events from the event generator, but still reconstructing three-jet events on the simulated events. It is clear from Figs. 25a, c, and d that the three-jet events are not only identified by their topology, but that they are the result of a genuine dynamical effect. In particular the star 3-jet events cannot be just fluctuations of the fragmentation of two high-p_T jets. The value of α_s obtained with this procedure is based on the exact lowest-order (LO) QCD formulae for the $2 \to 2$ and $2 \to 3$ processes, neglecting highest-order corrections, i.e. K factors. Thus the measured $\alpha_s(LO) = \alpha_s(HO) \times K(3\text{ jets})/K(2\text{ jets})$. The numerical value found is: $\alpha_s(LO) = 0.18 \pm 0.03 \pm 0.04$ at $Q^2 = 300$ GeV. The CMOR Collaboration at the ISR has also investigated three-jet production at $\sqrt{s} = 62$ GeV [50]. In this experiment, a global energy trigger was employed. The measured value for α_s is: $\alpha_s(K_3/K_2) = 0.19 \pm 0.02 \pm 0.04$ at $Q^2 = -t \simeq 300$ (GeV/c)^2, in good agreement with the AFS measurements. These results can be compared with $\alpha_s(LO) = 0.23 \pm 0.02 \pm 0.04$ (UA1) and $\alpha_s(LO) = 0.23 \pm 0.01 \pm 0.04$ (UA2) measured at higher energy and Q^2. There are large uncertainties in the determination of α_s, which come from the different choices of the Q^2 scale and from the structure functions, the jet algorithm, and the background contamination in the various experiments. However, the data indicate an increase of $\alpha_s(LO)$ going from the ISR to the Collider. A possible explanation of this effect is that at the ISR quark–quark interactions are probed, whilst at the Collider gluon–gluon interactions dominate the process: α_s increases because the gluons carry a larger colour charge than the quarks.

7. FOUR JETS AND THE DOUBLE-PARTON SCATTERING

There are two mechanisms that could yield, at the parton level, four jets in the final state: i) the QCD, order α_s^4, double-bremsstrahlung scattering (DBS); and ii) the double-parton scattering (DPS), $2 \times$ order α_s^2, as depicted in Fig. 26. There are 29 DBS processes that contribute to four jets [51]; also DPS yields have been calculated by several authors [52]. Although QCD bremsstrahlung events are a further powerful test of the theory, the investigation of DPS contributions gives access to more detailed information on the proton structure.

The AFS Collaboration at the ISR made a measurement of DPS production at $\sqrt{s} = 63$ GeV [53]. The main characteristic feature of four-jet events produced by a $2(2 \to 2)$ DPS mechanism, in contrast to a $2 \to 4$ DBS one, is that the four jets can be combined into two 2-jet systems, in each of which the two jets approximately balance their transverse momenta. Therefore, an 'imbalance' variable F was introduced, defined by

$$F = \frac{1}{2}\left(\vec{p}_{T1}^{\,2} + \vec{p}_{T2}^{\,2}\right) , \tag{8}$$

where $\vec{p}_{T1,2}^{\,2}$ are the total p_T of the two-jet systems, selected from the three possible combinations in each event in order to minimize F. For DPS events, F is expected to be small.

Figures 27a–d give the distribution of the imbalance F for various cuts on the smallest interjet angle ω and on the E_T of the smallest jet. These figures also indicate the Monte Carlo calculated contributions of QCD–DBS and DPS events. The best description of the data is obtained by the sum of the two components; DPS is dominating especially when the minimum-jet E_T is increased to

5 GeV. From the distributions in Fig. 27, a sample of DPS events could be extracted and compared with a model in which the DPS cross-section is defined by folding the two-parton spectrum once with itself, and dividing by a parameter σ_{eff} that has the dimension of an area. For a total transverse energy deposition of $\Sigma E_T = 31$ GeV, we have $\sigma_{eff} = 5$ mb. This area represents the effective size of the proton in which the hard interacting partons are confined.

A similar analysis was performed at the Collider by the UA2 Collaboration [54]. No evidence of DPS contribution was found at $\sqrt{s} = 630$ GeV in $p\bar{p}$ collisions; UA2 translates this result into a limit $\sigma_{eff} > 10$ mb (90% CL). But this value is not incompatible with the ISR measurement, since the ΣE_T deposition of jets required in the UA2 experiment is ≥ 60 GeV (twice that at the ISR), and already at the ISR a strong ΣE_T dependence of the fraction of DPS events contributing to the four-jet yield was observed, DPS being important at small jet energies.

8. THE COLLIDING PARTONS

The jets produced at the ISR emerge only at transverse momenta of 12 to 15 GeV/c, and they are expected to be predominantly due to u-quarks and d-quarks. The relative contributions of quarks and gluons are calculated in ref. [32], and are shown in Fig. 28a. In contrast, at the SPS Collider, although jets in excess of 100 GeV can now be produced routinely, the dominant contribution comes from gluon jets, as can be seen in Fig. 28b [32]. Under the assumption that u-quarks (charge $+2/3$) will yield more positive particles than d-quarks (charge $-1/3$), we expect naïvely that in pp collisions at the ISR the number of positive leading particles in a jet will be twice that of negative particles. A charge ratio $N^+/N^- = 1$ is instead expected for gluon jets. This charge ratio has been measured by the CMOR Collaboration as a function of the angle θ_j between a fragment and the direction of the jet [23]; this is shown in Fig. 29a. The charge ratio increases from 1 to about 1.4 as the particle approaches the core of the jet ($\theta_j \sim 0$). The AFS Collaboration has studied the charge ratio as a function of $z = 2\vec{p}\cdot\vec{n}/W$, with $\vec{p}$ the momentum of the charged fragment, $\vec{n}$ the direction of the jet, and W the c.m. energy of the dijet system [55]. The results are shown in Fig. 29b and confirm the hypothesis that at the ISR the jets come from charged partons. The scalar/vector nature of the coupling between constituents can be investigated by looking at the angular distribution of produced jets. The CCOR Collaboration has measured π^0 pair events at the ISR, and was able to show that the leading π^0 carries most of the momentum of the scattered parton [56]. Given this fact, the axis of the dipion system follows closely the direction of the scattered constituents and can be used to determine the angular dependence of the hard-scattering subprocess. The result of this analysis is shown in Fig. 30 for fixed $\pi^0\pi^0$ invariant mass m and p_T ranges. A QCD-motivated form was used to fit the data, where

$$\frac{d\sigma}{dm\, d\cos\theta^*} = \frac{A'}{m^N} G(x) \left[\frac{1}{(1 - \cos\theta^*)^a} + \frac{1}{(1 + \cos\theta^*)^a} \right] , \qquad (9)$$

where $\cos\theta^*$ is the average of the cosines of the polar angles between the π^0's and the proton axis in the frame where the dipion system has no net longitudinal momentum, $x = m/\sqrt{s}$. The fit gave $a = 2.97 \pm 0.05$, in agreement with QCD expectation. The relative contributions of quark and gluon scattering could be also extracted from the data; they are shown in Figs. 31a,b, again confirming that the ISR is essentially a quark collider. Another proof of the vector-coupling origin of parton interactions is shown in Fig. 32 [50]. In this figure a mixture of 64% qq and 36% qg can reproduce the experimental distribution of two jets. A similar analysis was performed also at the Colliders by UA1 [57], UA2 [58], and CDF [59], where gluon–gluon interactions dominate. It should be stressed, however, that all qq, $q\bar{q}$, qg, and gg angular distributions have approximately a universal $\sin^{-4}\theta/2$ shape, and they are essentially different only by the relative colour factors.

The SFM Collaboration at the ISR found a way of separating the various QCD hard subprocesses*). The experimental approach is based on tagging hard-scattered quarks [61] and gluons [62] by their identified leading fragments. The u (d) quarks are tagged by high-p_T π^+/K^+ (π^-) triggers, whilst K^- (= $s\bar{u}$), which do not share any valence quark with the proton, are predominantly leading fragments of hard-scattered gluons. Furthermore, use was made of parton-parton kinematics: in the case of quark-quark scattering, owing to the balanced structure functions, the two resulting jets will be collinear on average (back-to-back) in the pp rest system. Instead, if the elementary collision occurs between a quark and a gluon, then because of the soft gluon structure function, there will be on the average a Lorentz boost between the primary partons and the beam particles rest frames and the two jets will tend to be produced in the same pp c.m. rapidity hemisphere in the laboratory (back-to-antiback).

Figure 33 shows the density ratio for positive and negative particles associated with K^+ and π^+ triggers, measured at rapidity $y = 0.6$, as a function of the approximate fragmentation variable $x_E = p_T/p_T^{trig}$ for $y < 0$ (back-to-back) and $y > 0$ (back-to-antiback).

A ratio approaching 2 at $x_E \approx 0.7$ is found for the collinear configuration (u dominance in qq scattering). In the back-to-antiback topology, a lower ratio is measured owing to the larger contribution from gluons recoiling against the 'triggering' u-quark. In contrast, a larger charge ratio is observed in the back-to-antiback configuration for K^- triggers; this is attributed to u-quark jets recoiling against scattered gluons tagged by the K^- trigger.

The SFM Collaboration studied also the proton yields relative to the π^+ yield: they found that this ratio depends on p_T at fixed θ, on θ at fixed p_T, and on $\sqrt{s}$ at fixed $x_T = 2p_T/\sqrt{s}$ and θ. In contrast, relative K^+ and $\bar{p}$ yields are nearly independent of the kinematical variables. Hence, protons are not produced predominantly by hard scattering of quarks and gluons, but by interactions in which one or two of the incoming partons are bound states of two quarks. This hypothesis can be further investigated by looking at the flavour composition of spectator jets at $\theta \approx 0°$ for triggering $\pi^\pm$ mesons and protons at forward angles [63]. These spectator jets should be due to a system of two valence quarks in the case of a positive-meson trigger and to single valence quarks for a proton trigger from hard diquark scattering. The density ratios of positive and negative secondary particles associated with protons [$\varrho^\pm$ (p)] and $\pi^\pm$ mesons [$\varrho^\pm(\pi^\pm)$], respectively, were investigated:

$$R^+(p/\pi^\pm) = \frac{\varrho^+(p)}{\varrho^+(\pi^\pm)} \quad \text{and} \quad R^-(p/\pi^\pm) = \frac{\varrho^-(p)}{\varrho^-(\pi^\pm)} \,. \tag{10}$$

If protons were produced by diquark scattering, we could expect R^+ decreasing as the Feynman variable x_F increases, while R^- should be insensitive to x_F. The experimental results shown in Figs. 34a–d support the hypothesis of diquark scattering.

A significant signal for Δ^{++} production in the trigger jet indicates a non-negligible (uu) scattering component in addition to the dominant (ud) contribution to proton production [64]. The recoiling (away) jets produced with proton triggers are similar to those for pion triggers—valence quark and gluon fragmentations look quite similar.

*) The Split Field Magnet (SFM) set-up was able to perform measurement in a nearly full solid angle of the charges and momenta of the particles produced in the interactions [60]. An angular region of the detector was also equipped with Cherenkov counters that allowed a separation between π and K/p particles.

9. JET FRAGMENTATION

The investigation of the fragmentation properties of jets allows several QCD assumptions to be tested, such as the universality of quark–gluon fragmentation independent of the initial state (parton–parton or e^+e^-), Q^2-dependent scale-breaking effects, no flavour correlation between away and towards jets.

The AFS Collaboration measured the longitudinal jet fragmentation function

$$D(z) = \frac{1}{N_{jet}} \frac{dn}{dz}, \tag{11}$$

where n is the number of particles at $z = 2p_L/m$, with p_L the momentum component of the particle parallel to the direction of the momentum of the jet, and m the invariant mass of the dijet (m/2 is a measure of the energy of each jet in events with balanced transverse jet energy) [45]. The data are presented in Fig. 35. Superimposed on the figure are the fragmentation functions measured in e^+e^- interactions at comparable jet energies [65] and at the SPS Collider [66]. The ISR data are similar to the e^+e^- results, whilst the $p\bar{p}$ data have a steeper variation with z, indicating that, in contrast to ISR and e^+e^-, mainly gluon jets are measured at the SPS Collider.

Figure 36 shows a comparison of the mean charged multiplicity of jets with a curve fitting the multiplicity measured in e^+e^- hadronic annihilation. The overall agreement is not bad, especially for the high-$\sqrt{s}$ data [67]. For lower $\sqrt{s}$, the data show a larger mean multiplicity at the ISR by about one unit [68], and again this may be regarded as a sign of gluon jets.

An analysis of the jet recoiling against a large-p_T π^+ was performed at the SFM [69]. The π^+ data covered polar angles from 10° to 50° and p_T between 2 and 8 GeV/c. The mean values of the away-jet particle rapidities are plotted in Fig. 37 as a function of the θ of the π^+ trigger and for three values of the parton c.m. energy $\sqrt{\hat{s}}$. A slight back-to-back structure ($\langle y \rangle = 0$) is observed. The data are compared with model predictions from elementary ug → gu, ug → ug, gg → gg, uu → uu, and gu → gu. The data seem to favour a prevalence of ug → ug processes. The hypothesis that the recoiling jet be a gluon jet is also supported by the charge structure of the away jet. Figures 38a–c show the ratio R of positive and negative particle densities as a function of the away-jet particle rapidity y, fragmentation variable x_E, and c.m. energy $\sqrt{\hat{s}}$ for $\theta(\pi^+) = 47°$ and 18°. The ratio R is higher at $\theta(\pi^+) = 47°$; the gluon component is stronger at lower $\theta(\pi^+)$. The ratio is also increasing with x_E; this could be explained by a softer gluon fragmentation function relative to that of the u-quark.

The average value of the momentum component q_T of charged particles transverse to the jet axis is shown as a function of z in Fig. 39 [45]. An increase from $q_T \approx 0.3$ GeV at $z = 0.1$ to $q_T \approx 0.5$ GeV at $z > 0.3$ GeV is observed, in agreement with measurements in e^+e^- interactions [65] and at the SPS Collider [66]. The measurements are also consistent with the superimposed ISAJET Monte Carlo curve.

The overall charge structure of the dijet system was studied in terms of the normalized charge compensation ψ as a function of the rapidity along the direction of the jet axis, after a Lorentz boost to align the jet axis back-to-back [45]. The charge correlation function was defined as

$$\phi(y,y') = \left(\frac{d^2\sigma}{dy\,dy'}\right)_{OC} - \left(\frac{d^2\sigma}{dy\,dy'}\right)_{SC} \tag{12}$$

between two charged particles at rapidities y and y′ along the jet axis [OC (SC) stands for opposite charge (same charge)]. Figure 40 shows the normalized charge-compensation function:

$$\psi(y) = \frac{\int \phi(y,y')dy'}{\int (d\sigma/dy')dy'} \tag{13}$$

as a function of y, for a) positive and b) negative particles in y′ intervals ▬ as indicated in Fig. 40.

A short-range charge compensation is seen for both charges of the test particles, but for leading particles (large y's) the correlation is strongest for negative particles, reflecting that the jet has an overall positive charge. At $y < 0$ the compensation is of opposite sign and roughly equal magnitude for both positive and negative test particles, indicating that the charge distribution in the opposite jet is largely independent of the leading charge (flavour independence), and reflecting the overall larger density of positive particles. The curves superimposed on Fig. 40 are the predictions of ISAJET Monte Carlo, including only qq subprocesses. The agreement is good and excludes a large contribution from qg and gg subprocesses.

The AFS Collaboration studied also the correlations between pairs and triplets of identical charged particles within jets [70]. The size and the structure of this 'Bose-Einstein enhancement' is similar to those observed in minimum-bias events [71] and jets from e^+e^- annihilation [72]. All these results show that the source of the hadronization process has a size of about 1 fm.

The jet content of scalar, vector, and tensor particles is a measure of the probability of quark-antiquark pairs to recombine into a particle of given spin. This measurement was performed by the SFM Collaboration [73]: the production of $\varrho(770)$, $K^*(892)$, $\bar{K}^*(892)$, and $f_2(1270)$ as leading particles in jets was measured; and from then the fragmentation parameters vector/pseudoscalar for the u,d quarks $[(V/P)_{u,d}]$ and for the s quark $[(V/P)_s]$, and tensor/vector (T/V) could be extracted. The naïve expectation for V/P and T/V from counting the available spin states regardless of dynamics would be 3 and 5/3 respectively. The measured values: $(V/P)_{u,d} = 1.66 \pm 0.18 \pm 0.63$ from the ϱ/π production ratio; $(V/P)_s = 0.90 \pm 0.13 \pm 0.27$ from K^*/K production ratio; and $T/V = 0.30 \pm 0.08$ from f_2/ϱ, differ substantially from the naïve prediction and point to the existence of strong dynamical mechanisms suppressing high-spin final states.

10. SPECTATOR JETS

The study of the jet of particles generating from the fragmentation of partons not interacting directly (spectator jets) can provide an independent and complementary way of checking the parton model concepts. A strong correlation between the quantum number of the trigger (active quark) and spectator jets is expected. This effect was investigated in Ref. [74] by triggering on a large-p_T single particle. Figure 41 shows an example of this study: the ratio of the rapidity distribution of positive secondary particles for a π^+ trigger to that obtained with a π^- trigger is shown. The trigger particle is at $y \approx 2$. For $y > 2$, where the spectator fragments dominate, a clear excess of positive particles associated with the π^- trigger is visible; this effect agrees with the fact that the spectator quark system is of the uu type.

The global characteristics of spectator jets, such as p_T distribution and two-particle correlation, are similar to those obtained in normal inelastic events [75]. This indicates that similar fragmentation mechanisms act in both cases.

11. JETS IN $p\bar{p}$ AND LIGHT-ION COLLISIONS

The investigation of hard collisions from the pp initial state at the ISR was limited by the much lower integrated luminosity collected for $p\bar{p}$, compared with that for pp*).

The p_T spectrum of single particles has been found to be identical for pp and $p\bar{p}$ interactions up to p_T of 4–5 GeV/c at $\sqrt{s} = 53$ GeV, and the total neutral and charged transverse spectrum are found to be very similar [77]. As already mentioned in Section 5, differences in direct photon production, within the limited p_T range accessible, were not visible.

---

*) A comprehensive review of the results of $p\bar{p}$ physics at the ISR can be found in Ref. [76].

However, an interesting analysis performed by the CMOR Collaboration showed that a difference does indeed exist between pp and $p\bar{p}$ in large-p_T phenomena [78]. Figure 42 shows the ratio $p\bar{p}/pp$ for the neutral ΣE_T^0 spectra. A linear fit to the data points in Fig. 42 shows an increase of the ratio as ΣE_T^0 increases. Following the jet-finding algorithm and the subsequent sphericity definition of the event, the CMOR Collaboration divided the events into two sets, depending on whether the sphericity was below 0.2 (jet-like) or above 0.2 (isotropic). The ratio of $p\bar{p}$ to pp spectra for low sphericity is shown in Fig. 43a: the fit is perfectly consistent with unity. On the contrary, the $p\bar{p}$ to pp ratio for isotropic events (Fig. 43b) is consistently above unity, with a mean of 1.08 ± 0.01. This effect indicates a larger isotropic component in the $p\bar{p}$ sample relative to the pp one. This result can be traced back to the observation, at the ISR, of a larger mean multiplicity and stronger short-range rapidity correlation in $p\bar{p}$ than in pp [79]. These observations are most likely related to the larger probability of producing isotropic events in $p\bar{p}$ collisions. Collectively, this effect can be understood as being due to $p\bar{p}$ annihilation — a highly inelastic and high-multiplicity event.

Results on inclusive π^0 and η^0 meson production in pp and $p\bar{p}$ collisions were obtained by the AFS Collaboration [80]. No difference was found between the π^0 and η^0 production cross-sections in pp and $p\bar{p}$ collisions. The average ratio between these cross-sections was found to be 0.55 ± 0.04, in good agreement with previous results. We note that the QCD prediction for π^0 and η^0 production naturally gives the same cross-sections for pp and $p\bar{p}$, since at these intermediate x_T the mesons are mostly fragments of gluons, which have the same structure function for protons and antiprotons.

A particular point of interest in large-p_T physics with nuclei*) was the finding that with these complex initial states, large-p_T particle production grows faster than linearly with the nucleon numbers of the target (in contrast with the naïve expectation that is valid for all types of hard collisions). The result had formerly been obtained at FNAL [82]. This effect was also investigated at the ISR in $\alpha\alpha$, αp, and dd collisions, and was found to be consistent with the extrapolation of the FNAL data [83, 84]. However, there have been indications from one of the ISR experiments [85] that in αp interactions the inclusive cross-section for π^0 production at $p_T > 5$ GeV/c is lower than expected, as is also the case for dd collisions at $3.2 < p_T < 9$ GeV/c, whilst in $\alpha\alpha$ interactions it is higher. Figure 44 is an example of these measurements: the figure reports the ratio of invariant cross-sections in $\alpha\alpha$ and pp collisions for single-particle production at the same c.m. energy (15 GeV) per nucleon. For $p_T \geq 2$ GeV/c this ratio lies well above 16, which is the value expected from a linear dependence on the atomic number A. This departure may probably be ascribed either to collective phenomena in nuclei, which increases the parton density (structure function) [86], or to multiple scattering of partons before exiting from the nuclear matter [87].

Another interesting phenomenon can also occur in nucleus–nucleus scattering: the multiple nucleon–nucleon interactions in the same event can yield several jets in the final state. If this is the case, the correct quantity for the experimental investigation is the total energy instead of the single-particle momentum. This analysis was performed by the BCMOR Collaboration by looking at the total neutral transverse-energy distributions, ΣE_T^0, for $\alpha\alpha$, dd, and pp interactions [88]. Figure 45 shows these distributions: the ratio between $\alpha\alpha$ and pp ΣE_T^0 spectra goes from 100 at $\Sigma E_T^0 = 5$ GeV to 10^5 at $\Sigma E_T^0 = 15$ GeV. This result can actually be accounted for by a multiple nucleon–nucleon collision, with each collision producing an E_T spectrum (shown in Fig. 45) for pp interactions [88].

A consequence of parton rescattering would be an angular widening of the jet and a softening of the p_T distribution of particles belonging to it, compared with pp interactions. This comparison was made in Refs. [84] and [89]. The authors of Ref. [89] conclude that rescattering cannot be excluded at the level of up to 20% in αp and 40% in $\alpha\alpha$ collisions.

---

*) A general review of physics with α particles at the ISR can be found in Ref. [81].

12. CONCLUSIONS

Large-p_T phenomena were first found at the ISR, however it was not until some years later that the experimental unbiased way to look for jets was discovered. At that time a larger-energy machine (the CERN $p\bar{p}$ Collider) was brought into operation. This limited the role of the ISR in this field of physics. Nevertheless, the ISR provided a great number of large-p_T physics results, which I have tried to summarize here. The lack of space has meant that many other interesting data could not be included in this review, and for this I apologize to the authors.

In my opinion the ISR was shut down prematurely: because of its high luminosity, it could still have played a unique role in exploring the regions of extreme phase space where valence-quark interactions dominate, which are not accessible to the present Colliders. A consistent set of such data comparing pp and $p\bar{p}$ interactions would have been of great value.

Acknowledgements

I participated in experiments at the ISR, from its inauguration in 1971 until it was dismantled (1983). During these years I could appreciate the superb professionalism of the ISR staff, which led to the excellent performance that was obtained.

I am grateful to the physicists of the various experiments for their collaboration in helping me to prepare this review. Finally, I would like to thank G. Bellettini for the many enlightening discussions and for his advice.

REFERENCES

[1] B. Alper et al., Phys. Lett. **44B**, 521 and 527 (1973).

[2] M. Banner et al., Phys. Lett. **44B**, 537 (1973).

[3] F.W. Büsser et al., Phys. Lett. **46B**, 471 (1973).

[4] C. Kourkoumelis et al., Z. Phys. **C5**, 95 (1980).

[5] M. Banner et al. (UA2 Collab.), Z. Phys. **C27**, 329 (1985).

[6] S. Berman, J.D. Bjorken and J. Kogut, Phys. Rev. **D4**, 3388 (1971).

[7] R.D. Feynman, Photon-hadron interactions (Benjamin, New York, 1972).

[8] R. Blankenbecler, S.J. Brodsky and J.F. Gunion, Phys. Lett. **39B**, 649 and Phys. Rev. **D6**, 2652 (1972); Phys. Lett. **42B**, 461 and Phys. Rev. **D8**, 287 (1973); Phys. Rep. **23C**, 1 (1976).

[9] G. Finocchiaro et al., Phys. Lett. **50B**, 367 (1974).
P. Darriulat et al., Nucl. Phys. **B107**, 429 and **B110**, 365 (1976).
M. Della Negra et al., Nucl. Phys. **B104**, 365 (1976) and **B127**, 1 (1977).
R. Kephart et al., Phys. Rev. **D14**, 2909 (1976).
M.G. Albrow et al., Nucl. Phys. **B135**, 461 and **B145**, 305 (1978), and **B160**, 1 (1979).

[10] G. Hanson et al., Phys. Rev. Lett. **35**, 1609 (1975).

[11] J.D. Bjorken, Acta Phys. Pol. **B5**, 145 (1974).
M. Jacob and P. Landshoff, Nucl. Phys. **B113**, (1976) 395.

[12] G. Giacomelli and M. Jacob, Phys. Rep. **55**, 1 (1979).

[13] P. Darriulat, Annu. Rev. Nucl. Part. Sci. **30**, 159 (1980).

[14] N.A. McCubbin, Rep. Prog. Phys. **44**, 1027 (1981).

[15] A comprehensive review of quantum chromodynamics theory can be found in M. Jacob (ed.), Perturbative quantum chromodynamics (North Holland, Amsterdam, 1982).
For more recent progress see, for example, J.C. Collins and D.E. Soper, Annu. Rev. Nucl. Part. Sci. **37**, 383 (1987).

[16] See, for example, B. Adeva et al., Phys. Rev. Lett. **54**, 1750 (1985).

[17] B.L. Combridge, L. Kripfganz and J. Ranft, Phys. Lett. **70B**, 234 (1977).
R. Cutler and D. Sivers, Phys. Rev. **D17**, 196 (1978).

[18] See, for example, M. Furman, Nucl. Phys. **B197**, 413 (1982).

[19] G. Altarelli and G. Parisi, Nucl. Phys. **B126**, 298 (1977).

[20] H. Georgi and H.D. Politzer, Phys. Rev. Lett. **40**, 3 (1978).
T. Vermat, Phys. Lett. **79B**, 97 (1978).
J.F. Owens, Phys. Lett. **76B**, 85 (1978).

[21] M. Banner et al. (UA2 Collab.), Phys. Lett. **B118**, 203 (1982).

[22] P. Bagnaia et al. (UA2 Collab.), Phys. Lett. **B138**, 430 (1984).
For a general review of jets, see L. Di Lella, Annu. Rev. Nucl. Part. Sci. **35**, 107 (1985).

[23] A.L.S. Angelis et al. (COR Collab.), Phys. Lett. **126B**, 132 (1983) and Nucl. Phys. **B244**, 1 (1984).

[24] T. Åkesson et al. (AFS Collab.), Phys. Lett. **128B**, 354 (1983).

[25] C. De Marzo et al. (NA5 Collab.), Phys. Lett. **128B**, 173 (1982) and Nucl. Phys. **B211**, 375 (1983).

[26] B. Brown et al., Phys. Rev. Lett. **49**, 711 (1982).

[27] T. Åkesson et al. (AFS Collab.), Phys. Lett. **118B**, 185 and 193 (1982) and **123B**, 133 (1983).

[28] F.E. Paige and S.D. Protopopescu, Proc. DPF Summer Study on Elementary particles and Future Facilities, Snowmass, Colo., 1982 (Amer. Phys. Soc., New York, 1983), p. 471, and various corrections 1982–85.

[29] A. Bayer et al., Z. Phys. **C2**, 265 (1979).

[30] R. Feynman and R. Field, Nucl. Phys. **B136,** 1 (1978).
[31] F. Abe et al. (CDF Collab.), Phys. Rev. Lett. **62,** 613 (1989).
[32] R. Horgan and M. Jacob, Nucl. Phys. **B179,** 441 (1981).
[33] J.A. Appel et al. (UA2 Collab.), Phys. Lett. **160B,** 349 (1985).
[34] F. Halzen and D. Scott, Phys. Lett. **78B,** 318 (1978).
[35] P. Aurenche et al., Phys. Lett. **140B,** 87 (1984).
[36] M. Diakonou et al., Phys. Lett. **87B,** 292 (1979) and **91B,** 296 (1980).
E. Anassontzis et al., Z. Phys. **C13,** 277 (1982).
[37] A.L.S. Angelis et al. (CCOR Collab.), Phys. Lett **94B,** 106 (1980).
[38] T. Åkesson et al. (AFS Collab.), Phys. Lett. **118B,** 178 (1982) and **123B,** 367 (1983).
A.L.S. Angelis et al. (CCOR Collab.), Phys. Lett. **98B,** 115 (1981).
[39] T. Åkesson et al. (AFS Collab.), Phys. Lett. **158B,** 282 (1985) and contribution to the Int. Europhysics Conf. on High-Energy Physics, Bari, 1985.
[40] T. Åkesson et al. (AFS Collab.), Z. Phys. **C34,** 293 (1987).
[41] H. Abramowicz et al., Z. Phys. **C12,** 289 (1982).
[42] P. Aurenche et al., Nucl. Phys. **B297,** 661 (1988).
[43] A. Bernasconi et al. (UA6 Collab.), Phys. Lett. **206B,** 163 (1988).
[44] R. Ansari et al. (UA2 Collab.), Z. Phys. **C41,** 395 (1988).
[45] T. Åkesson et al. (AFS Collab.), Z. Phys. **C30,** 27 (1986).
[46] D.W. Duke and J.F. Owens, Phys. Rev. **D30,** 49 (1984).
[47] G. Arnison et al. (UA1 Collab.), Phys. Lett. **158B,** 494 (1985).
[48] J.A. Appel et al. (UA2 Collab.), Z. Phys. **C30,** 341 (1986).
[49] T. Åkesson et al. (AFS Collab.), Z. Phys. **C32,** 317 (1986).
[50] A.L.S. Angelis et al. (CMOR Collab.), Nucl. Phys. **B303,** 569 (1988).
[51] Z. Kunszt and W.J. Stirling, Phys. Lett. **171B,** 307 (1986), and references therein.
[52] See, for example, B. Humpert and R. Odorico, Phys. Lett. **154B,** 211 (1985).
[53] T. Åkesson et al. (AFS Collab.), Z. Phys. **C34,** 163 (1987).
[54] See, for example, the presentation of V. Cavasinni (UA2 Collab.) at the DPF Meeting, Storrs, Conn., 1988, to be published in the Proceedings.
[55] T. Åkesson et al. (AFS Collab.), Z. Phys. **C25,** 13 (1984).
[56] A.L.S. Angelis et al. (CCOR Collab.) Nucl. Phys. **B209,** 284 (1982).
[57] G. Arnison et al. (UA1 Collab.), Phys. Lett. **136B,** 294 (1984).
[58] P. Bagnaia et al. (UA2 Collab.), Phys. Lett. **144B,** 283 (1984).
[59] L. Pondrom (CDF Collab.), presented at the DPF Meeting, Storrs, Conn., 1988, to be published in the Proceedings.
[60] M. Della Negra et al. (SFM Collab.), Nucl. Phys. **B127,** 1 (1977).
[61] D. Drijard et al. (SFM Collab.), Nucl. Phys. **B156,** 309 (1979).
A. Breakstone et al. (SFM Collab.), Z. Phys. **C25,** 21 (1984).
[62] A. Breakstone et al. (SFM Collab.), Z. Phys. **C27,** 205 (1985).
[63] A. Breakstone et al. (SFM Collab.), Phys. Lett. **147B,** 237 (1984); Z. Phys. **C28,** 335 (1985) and **C35,** 159 (1987).
D. Bender et al., Phys. Rev. **D31,** 1 (1985).
[64] A. Breakstone et al. (SFM Collab.), Z. Phys. **C36,** 567 (1987).
[65] M. Althoff et al., Z. Phys. **C22,** 307 (1984).
[66] G. Arnison et al. (UA1 Collab.), Phys. Lett. **132B,** 223 (1983).
[67] M.G. Albrow et al., Nucl. Phys. **B160,** 1 (1980).
[68] A.G. Clark et al., Nucl. Phys. **B160,** 397 (1980).
[69] A. Breakstone et al. (SFM Collab.), Z. Phys. **C33,** 475 (1987).

[70] T. Åkesson et al. (AFS Collab.), Z. Phys. **C36,** 317 (1987).
[71] A. Breakstone et al. (SFM Collab.), Phys. Lett. **162B,** 400 (1985) and Z. Phys. **C33,** 333 (1987).
[72] M. Althoff et al., Z. Phys. **C30,** 355 (1986).
[73] A. Breakstone et al. (SFM Collab.), preprint CERN-EP/89-21 (1989).
[74] D. Drijard et al. (SFM Collab.), Nucl. Phys. **B156,** 309 (1979).
[75] D. Drijard et al. (SFM Collab.), Nucl. Phys. **B155,** 269 (1979) and **B166,** 233 (1980).
[76] L. Camilleri, Phys. Rep. **144,** 51 (1987).
[77] T. Åkesson et al. (AFS Collab.), preprints CERN-EP/82-104 (1982) and Nucl. Phys. **B228,** 409 (1983).
A.L.S. Angelis et al. (COR Collab.), Phys. Lett. **B126,** 217 (1982).
[78] A.L.S. Angelis et al. (CMOR Collab.), Nucl. Phys. **B263,** 228 (1986).
[79] V. Cavasinni, Proc. Moriond Workshop on Antiproton-Proton Physics and the W discovery, La Plagne, 1983 (Éd. Frontières, Gif-sur-Yvette, 1983), p. 171.
V. Cavasinni et al., Z. Phys. **C21,** 299 (1984).
[80] T. Åkesson et al. (AFS Collab.), Phys. Lett. **B158,** 282 (1985).
[81] M.A. Faessler, Phys. Rep. **115,** 1 (1984).
[82] J.W. Cronin et al., Phys. Rev. **D11,** 3105 (1975).
L. Kluberg et al., Phys. Rev. Lett. **38,** 670 (1977).
D. Antreasyan et al., Phys. Rev. **D19,** 764 (1979).
[83] A. Karabarbounis et al., Phys. Lett. **104B,** 75 (1981).
W. Bell et al., Phys. Lett. **112B,** 271 (1982).
[84] T. Åkesson et al. (AFS Collab.), Nucl. Phys. **B209,** 309 (1982).
[85] A.L.S. Angelis et al. (COR Collab.), Phys. Lett. **116B,** 379 (1982) and **185B,** 213 (1987).
[86] See, for example, A. Krzywicki, Phys. Rev. **D14,** 152 (1976).
[87] See, for example, P.M. Fishbane et al., Phys. Rev. **D16,** 122 (1977).
[88] A.L.S. Angelis et al. (BCMOR Collab.), Phys. Lett. **B141,** 140 (1984).
[89] W. Bell et al., Z. Phys. **C30,** 513 (1986).

Figure captions

Fig. 1 Inclusive π^0 yield at large p_T. The solid line is an exponential extrapolation from $p_T \leq 1$ GeV/c.

Fig. 2 Comparison of the inclusive π^0 yield at the ISR and at the CERN $p\bar{p}$ Collider at $\sqrt{s} = 540$ GeV.

Fig. 3 Diagram of parton interaction between two incident hadrons A and B yielding the large-p_T final-state particle C.

Fig. 4 The AFS detector: the calorimeter modules and the inner tracking chamber are shown.

Fig. 5 The COR detector: the superconductive solenoid is shown, together with the chamber system and the lead-glass array.

Fig. 6 Total transverse energy distribution (ΣE_T) measured in UA2 at $\sqrt{s} = 540$ GeV. At $\Sigma E_T \gtrsim 60$ GeV, a departure from the exponential behaviour measured at lower energy is clearly visible.

Fig. 7 UA2 Collaboration: fraction of total transverse energy taken by the two leading jets $[(E_T^1 + E_T^2)/\Sigma E_T]$ and by the leading jet $(E_T^1/\Sigma E_T)$ at $\sqrt{s} = 540$ GeV.

Fig. 8 COR Collaboration: distribution of ΣE_T^0 deposition at $\sqrt{s} = 62.3$ GeV. A deviation from an exponential fall-off occurs at $\Sigma E_T^0 \gtrsim 20$ GeV.

Fig. 9 AFS Collaboration: ΣE_T deposition distribution at $\sqrt{s} = 30$, 45, and 63 GeV.

Fig. 10 AFS Collaboration: circularity distribution (see text) at $\sqrt{s} = 30$, 45, and 63 GeV, and for three intervals of ΣE_T. As $\sqrt{s}$ and $\langle \Sigma E_T \rangle$ increase, the circularity peaks to zero, indicating the presence of jet events.

Fig. 11 a) AFS Collaboration: mean circularity at $\sqrt{s} = 30$, 45, and 63 GeV versus ΣE_T. b) AFS Collaboration: ratio of ΣE_T to the average particle momentum in the event $\langle p_T \rangle$.

Fig. 12 a) COR Collaboration: the mean fraction of ΣE_T^0 contained in the two most energetic clusters (full circles) and the mean fraction of ΣE_T^0 contained in the most energetic cluster (empty circles) versus ΣE_T^0. b) AFS Collaboration: fraction of events with more than 60% of their ΣE_T in two non-overlapping regions of $\Delta\phi = 60°$ and $\Delta y = 1$, versus ΣE_T.

Fig. 13 AFS Collaboration: thrust distribution at $\sqrt{s} = 45$ and 63 GeV for several intervals of ΣE_T. The shaded areas represent the fitted QCD jet component.

Fig. 14 AFS Collaboration: Inclusive jet cross-section measured at $\sqrt{s} = 45$ and 63 GeV. QCD predictions are compared with the data points. As a comparison, the inclusive π^0 cross-section is also shown.

Fig. 15 Inclusive jet cross-section at $\sqrt{s} = 63$ GeV [AFS], 540 GeV [UA1, UA2], and 1800 GeV [CDF]. The data are compared with QCD predictions, dashed and dashed-dotted curves. Uncertainties in theoretical predictions are also shown as the two solid curves at $\sqrt{s} = 540$ GeV.

Fig. 16 a) Scaled jet cross-section $p_T^4 E(d\sigma/dp^3)$ at $\sqrt{s} = 45$, 63, 540, and 630 GeV; b) same as (a) but the cross-sections are scaled as $p_T^{4.74} E(d\sigma/dp^3)$.

Fig. 17 The two QCD lowest-order diagrams (Compton and annihilation) for direct-photon production.

Fig. 18 a) Experiment R806: observed γ/π^0 ratio, as a function of p_T at $\sqrt{s} = 63$ GeV. b) Experiment R108: γ/all ratio, as a function of p_T at $\sqrt{s} = 44$ and 63 GeV.

Fig. 19 AFS Collaboration: γ/π^0 ratio as a function of p_T at $\sqrt{s} = 53$ GeV for pp and $p\bar{p}$ initial states. The curves are QCD predictions (solid for pp, dashed for $p\bar{p}$).

Fig. 20 AFS Collaboration: gluon structure function as extracted in photon–jet events. The dashed curve is the gluon structure function measured in deep-inelastic scattering.

Fig. 21 Inclusive prompt-photon cross-section measured by AFS, R806, and CCOR at $\sqrt{s}$ = 63 GeV. The curves are different theoretical predictions with different structure functions as an input.

Fig. 22 a) Inclusive direct photon cross-section at $\sqrt{s}$ = 24, 53, and 630 GeV in $p\bar{p}$ collisions scaled as p_T^{-4}; b) same as 22a, but scaled as $p_T^{-4.74}$.

Fig. 23 AFS Collaboration: dijet invariant mass distribution at $\sqrt{s}$ = 63 GeV. The two curves are QCD predictions with two sets of structure functions as parametrized by Duke and Owens.

Fig. 24 COR Collaboration: distribution of azimuthal angle between two neutral jets carrying an E_T between 26 and 30 GeV.

Fig. 25 AFS Collaboration: Dalitz plot x_2 versus x_1 for three-jet events in the transverse plane: a) AFS experimental data. The 'star' three-jet events are those with $x_3 \geqslant 0.40$ and $\omega \geqslant 60°$. b) The geometry of three-jet events in the Dalitz plot. The inset shows the definition of the interjet angle ω. Lines of constant x_3 or ω are indicated. The small diagrams are examples of the momentum vectors of the jets in three-jet events. c) Monte Carlo. The event generator produces both two-jet and multijet events, which are passed through the detector simulation. d) Monte Carlo. The event generator produces two-jet events only. The region of 'star' three-jet events is shown — it is virtually empty.

Fig. 26 Schematic diagrams illustrating the two possible mechanisms for yielding four jets: i) bremsstrahlung: QCD-scattered quarks (or gluons) radiate gluons: ii) double-parton scattering: two pairs of quarks from the incident hadron interact in two separate QCD scatterings.

Fig. 27 AFS Collaboration: distribution of the imbalance parameter F (see text) for uncorrected data compared with the bremsstrahlung and DPS model predicitons. These figures correspond to various cuts in the E_T of jet No. 4 (E_T^4) and in interjet angles, as indicated. The data are fitted to a sum of the two components. The results of the fit are the fractions of DPS as shown.

Fig. 28 QCD calculation showing the relative importance of gluon and quark jets: a) at the ISR and b) at the CERN $p\bar{p}$ Collider.

Fig. 29 a) CMOR Collaboration: the charge ratio N^+/N^- as a function of the angle θ_j between a fragment and the parent jet direction. b) AFS Collaboration: same as (a); the dashed areas are the QCD predictions coming from different elementary interactions: qq, qg, gg.

Fig. 30 CCOR Collaboration: angular distribution of pion pairs as a function of the $\cos\theta^*$ and for different dipion invariant-mass bins.

Fig. 31 CCOR Collaboration: relative contributions of valence quark–valence quark (qq–qq), gluon–valence quark (gq–gq), and gluon–gluon (gg–gg, gg–qq) scattering. Curves labelled (1) and (2) use gluon fragmentation functions of $(1-z)^2$ and $(1-z)^3$, respectively: a) $\sqrt{s}$ = 44.8 GeV, b) $\sqrt{s}$ = 62.4 GeV.

Fig. 32 CMOR Collaboration: angular distribution of two-jet events at $\sqrt{s}$ = 62.4 GeV. The curve is a QCD fit with an input of an admixture of qq (64%) and qg (36%) interactions.

Fig. 33 SFM Collaboration: ratio of densities of positive to negative particles for K^- and K^+/π^- in the back-to-antiback configuration, and K^+/π^+ triggers in the back-to-back configuration, as a function of $x_E = p_T/p_T^{trigger}$.

Fig. 34 SFM Collaboration: ratios of positive spectator secondaries associated with proton and pion triggers at $\theta \approx 10°$, and with $p_{lab} \geq 13$ GeV/c: a) π^+ trigger, b) π^- trigger. The shaded regions indicated at large x_F are predictions based upon deep-inelastic neutrino scattering data, c) and d) are the same as (a) and (b) but for negative spectator secondaries.

Fig. 35 AFS Collaboration: jet fragmentation distribution D(z) as a function of z. The ISR data are compared with the fragmentation distribution measured in e^+e^- at $\sqrt{s} = 22$ and 34 GeV and in $p\bar{p}$ at $\sqrt{s} = 540$ GeV.

Fig. 36 Jet multiplicities as a function of jet–jet energy measured at the ISR in pp interactions. The solid line is a fit to the jet multiplicity in e^+e^- annihilations.

Fig. 37 SFM Collaboration: mean values of the away-side rapidity distribution in events with π^+ triggers as a function of θ. The data are shown for three different values of $\langle\sqrt{\hat{s}}\rangle$. Typical QCD predictions for $\langle\sqrt{\hat{s}}\rangle = 16$ GeV are also indicated.

Fig. 38 SFM Collaboration: away-side charge ratio R for π^+-triggered events: a) as a function of the rapidity y; b) as a function of $\langle\sqrt{\hat{s}}\rangle$; c) as a function of the fragmentation variable x_E. Data at $\langle\theta\rangle = 47°$ and $\langle\theta\rangle = 18°$ are shown separately.

Fig. 39 AFS Collaboration: average value of the momentum component $\langle q_T\rangle$ perpendicular to the jet axis as a function of the fragmentation variable z. The solid line is a model prediction.

Fig. 40 AFS Collaboration: study of the charge compensation (see text). Left side: charge density as a function of the particle rapidity and for four different rapidity positions of a positive test particle. Right side: same as left side, but the test particle was negative.

Fig. 41 SFM Collaboration: ratio of the distribution of spectator fragments for a π^+ trigger $[(1/\sigma)(d\sigma/dy)_{\pi^+}] \equiv \varrho(y/\pi^+)$ and for a π^- trigger $\varrho(y/\pi^-)$ as a function of rapidity.

Fig. 42 CMOR Collaboration: ratio between ΣE_T^0 spectrum in $p\bar{p}$ and pp interactions. The upper solid line is a fit to the data points.

Fig. 43 Same as Fig. 42, but the events were classified as a) low sphericity and b) large sphericity samples. The solid lines indicate the unit reference.

Fig. 44 AFS Collaboration: ratio between invariant cross-sections in $\alpha\alpha$ and αp interactions as a function of p_T at the same nucleon c.m. energy.

Fig. 45 BCMOR Collaboration: ΣE_T^0 distribution in $\alpha\alpha$ and pp interactions at the same nucleon–nucleon energy, at $\sqrt{s} = 15$ GeV.

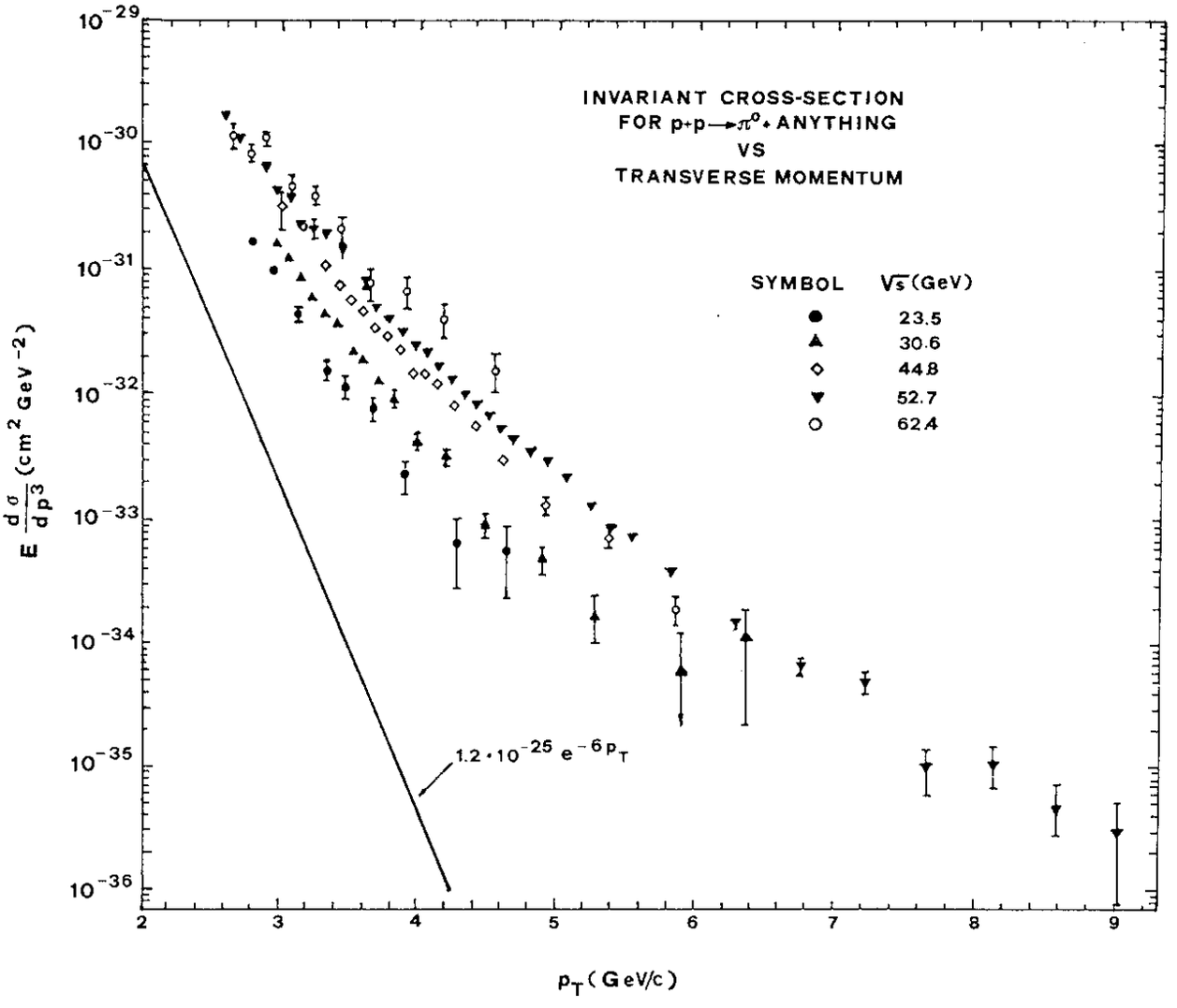
INVARIANT CROSS-SECTION
FOR p+p→π⁰+ ANYTHING
VS
TRANSVERSE MOMENTUM
SYMBOL
√s (GeV)
23.5
30.6
44.8
52.7
62.4
1.2·10⁻²⁵ e⁻⁶ᵖᵀ
E dσ/dp³ (cm² GeV⁻²)
pT (GeV/c)

Fig. 1

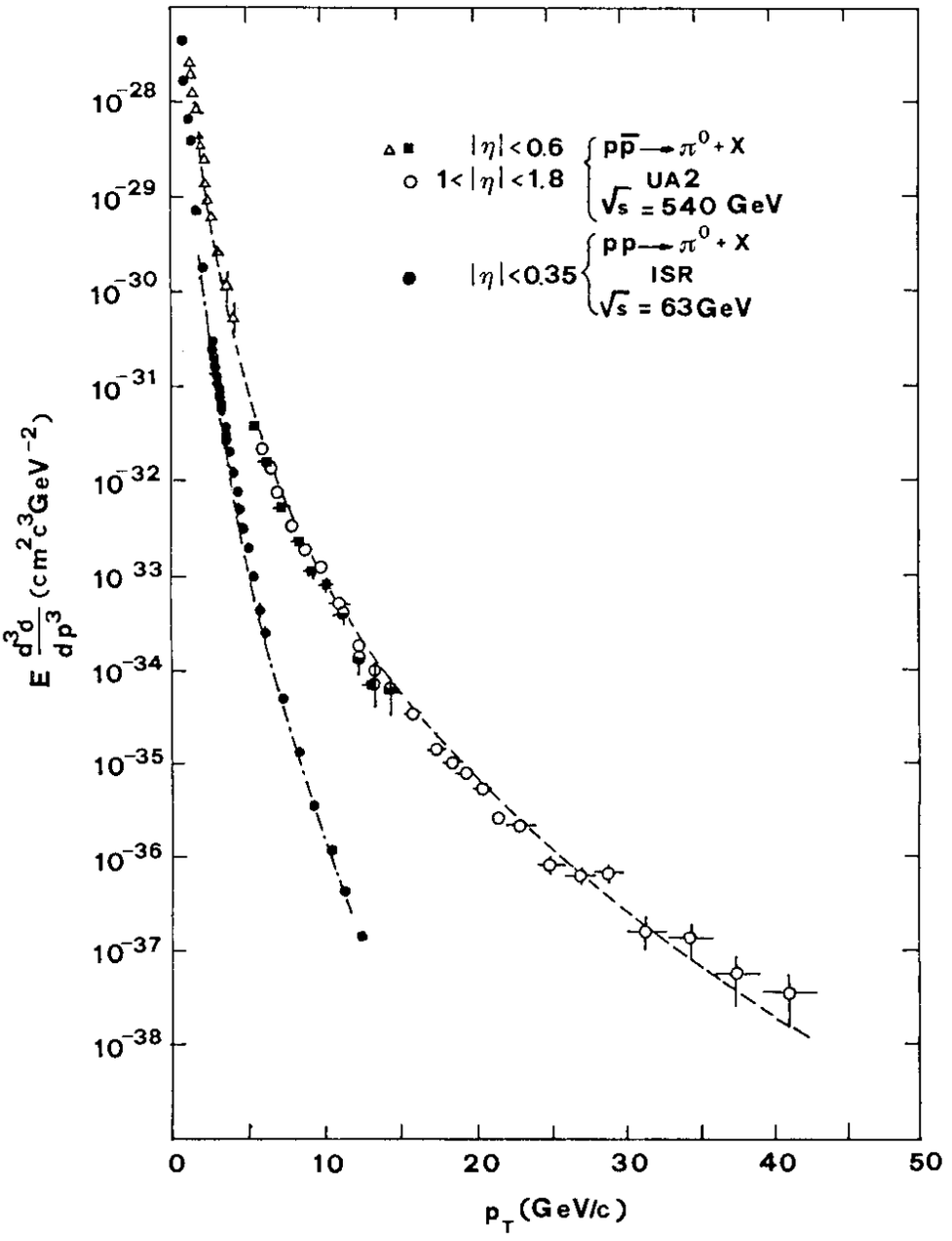
10^{-28}
10^{-29}
10^{-30}
10^{-31}
10^{-32}
10^{33}
10^{-34}
10^{-35}
10^{-36}
10^{-37}
10^{-38}
$E\frac{d^3\sigma}{dp^3}$ (cm^{2}c^{3}GeV^{-2})
$|\eta|<0.6$ $p\bar{p}\rightarrow\pi^0+X$
$1<|\eta|<1.8$ UA2
$\sqrt{s}$ = 540 GeV
$|\eta|<0.35$ $pp\rightarrow\pi^0+X$
ISR
$\sqrt{s}$ = 63GeV
0
10
20
30
40
50
p_T (GeV/c)

Fig. 2

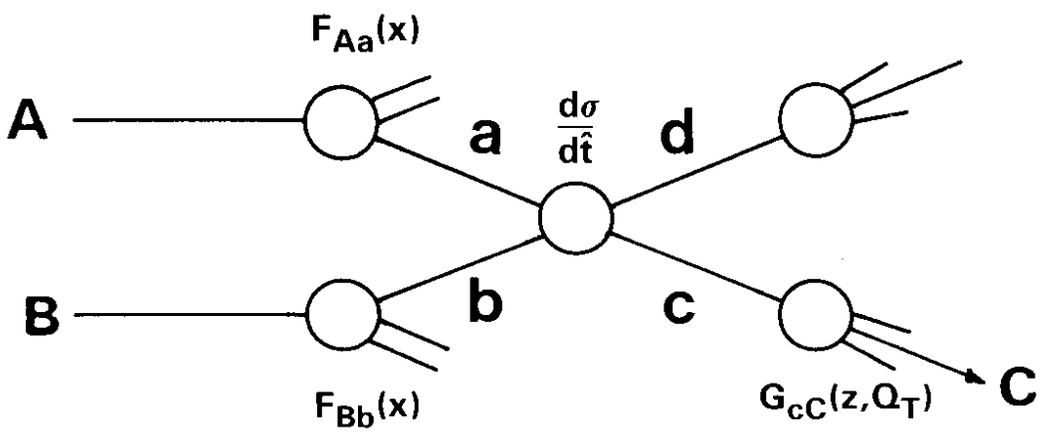
$F_{Aa}(x)$
A
a
$\frac{d\sigma}{d\hat{t}}$
d
B
b
c
C
$F_{Bb}(x)$
$G_{cC}(z,Q_T)$

Fig. 3

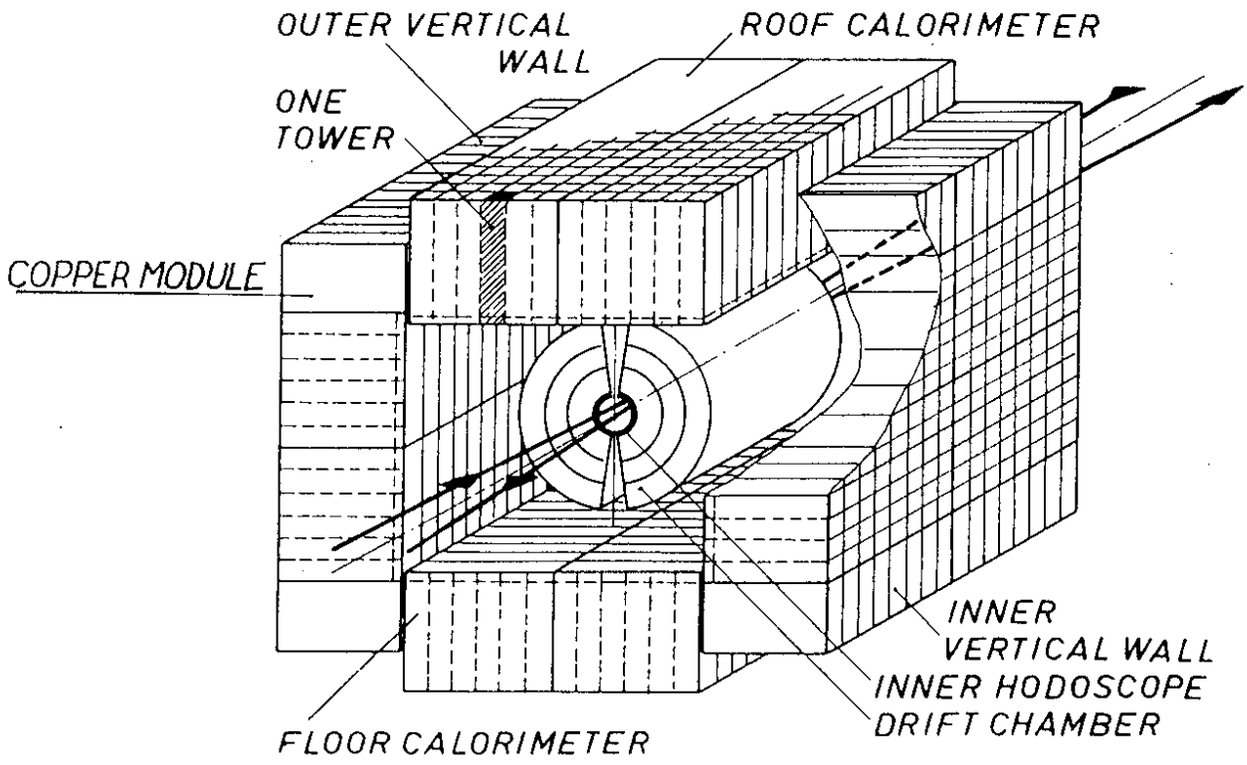
OUTER VERTICAL WALL
ROOF CALORIMETER
ONE TOWER
COPPER MODULE
INNER VERTICAL WALL
INNER HODOSCOPE
DRIFT CHAMBER
FLOOR CALORIMETER

Fig. 4

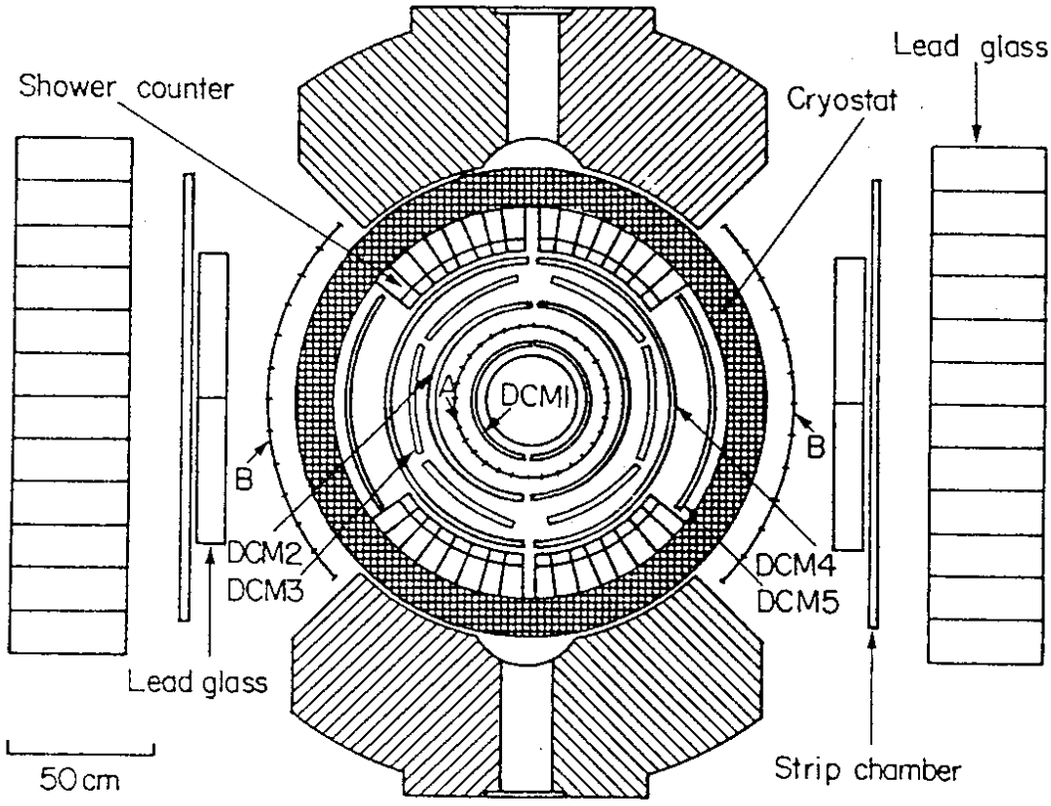
Shower counter
Lead glass
Cryostat
DCMI
B
B
DCM2
DCM3
DCM4
DCM5
Lead glass
Strip chamber
50 cm

Fig. 5

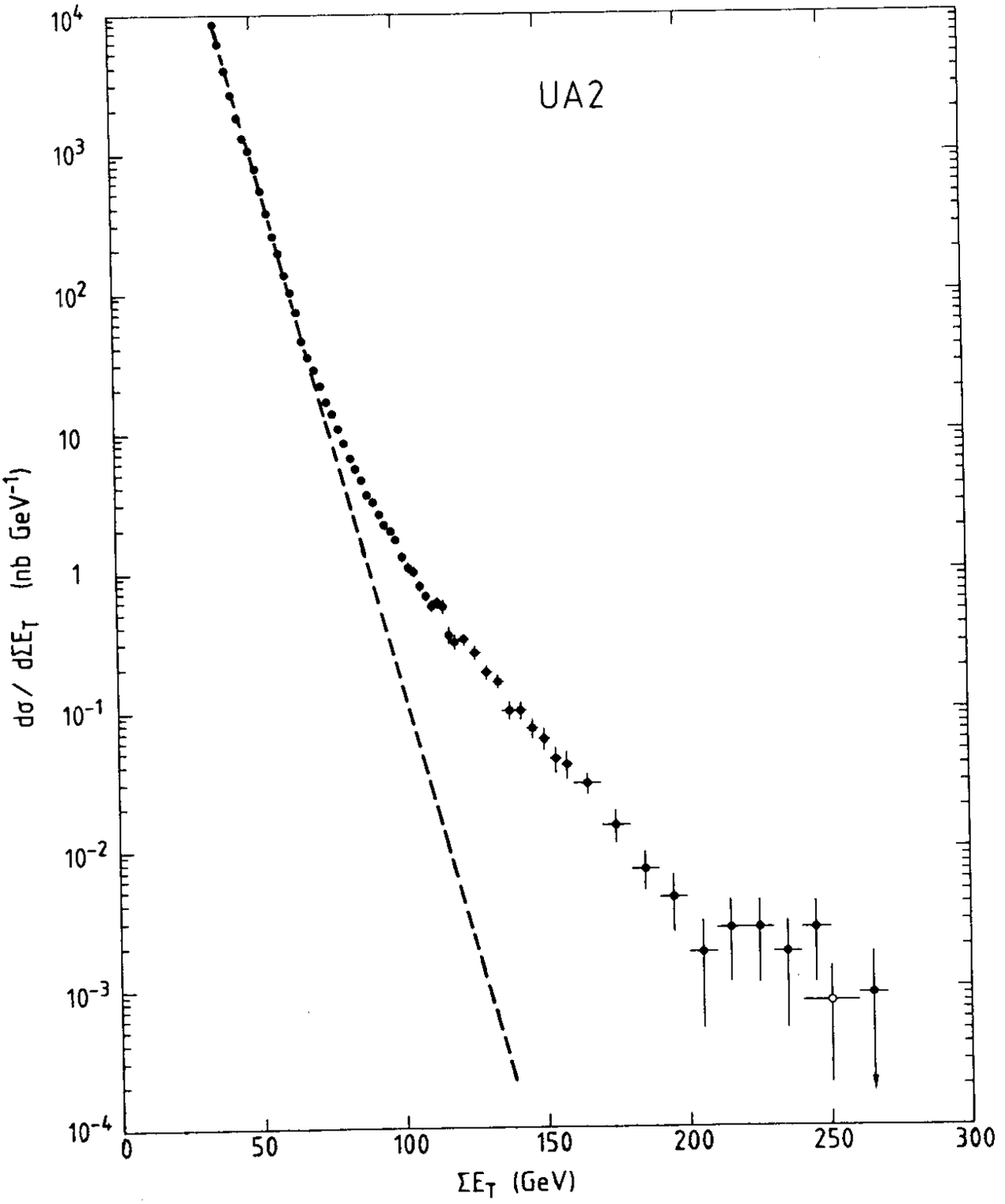
UA2
10^4
10^3
10^2
10
1
10^{-1}
10^{-2}
10^{-3}
10^{-4}
$d\sigma / d\Sigma E_T$ (nb GeV^{-1})
0
50
100
150
200
250
300
ΣE_T (GeV)

Fig. 6

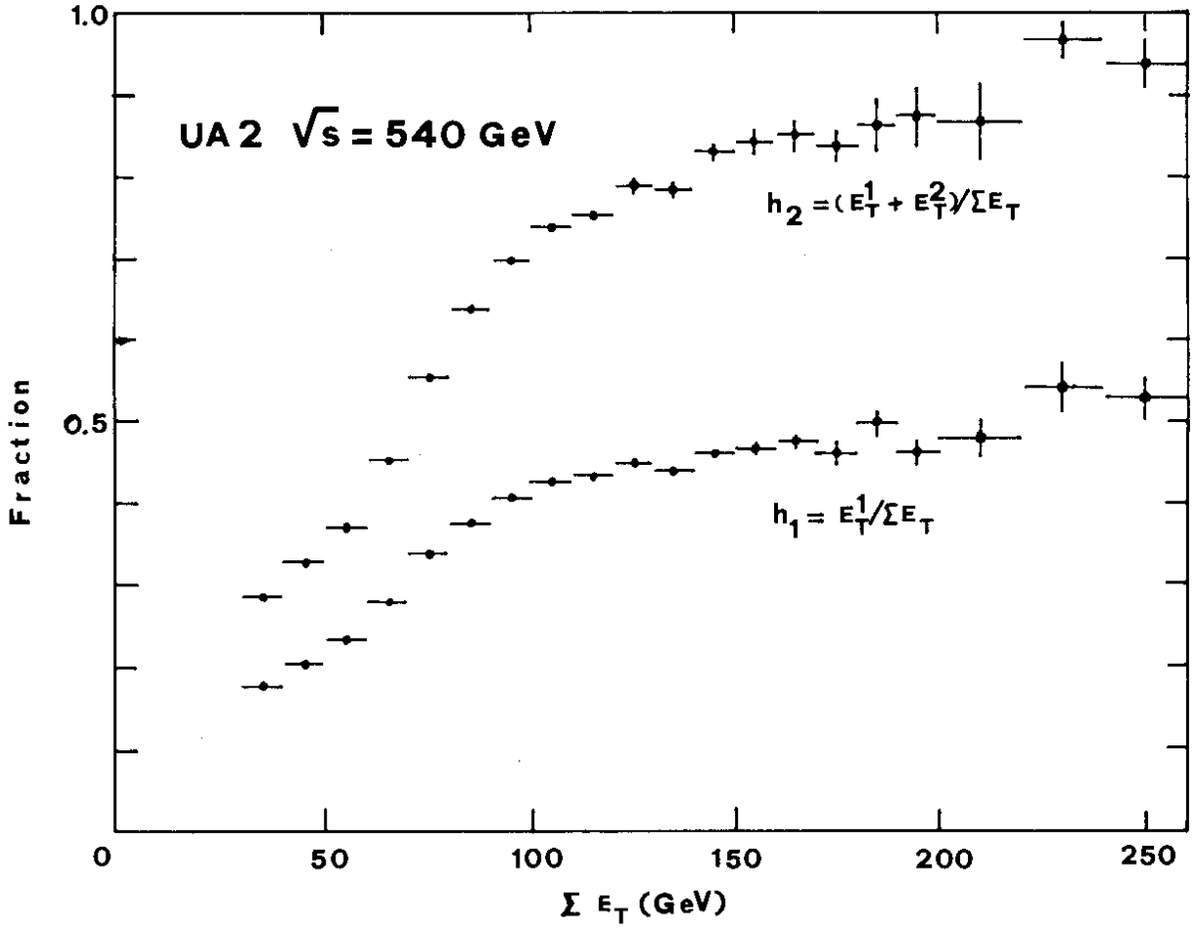
UA 2 √s = 540 GeV
h2 = (E1T + E2T)/ΣET
h1 = E1T/ΣET
Fraction
1.0
0.5
0
50
100
150
200
250
Σ ET (GeV)

Fig. 7

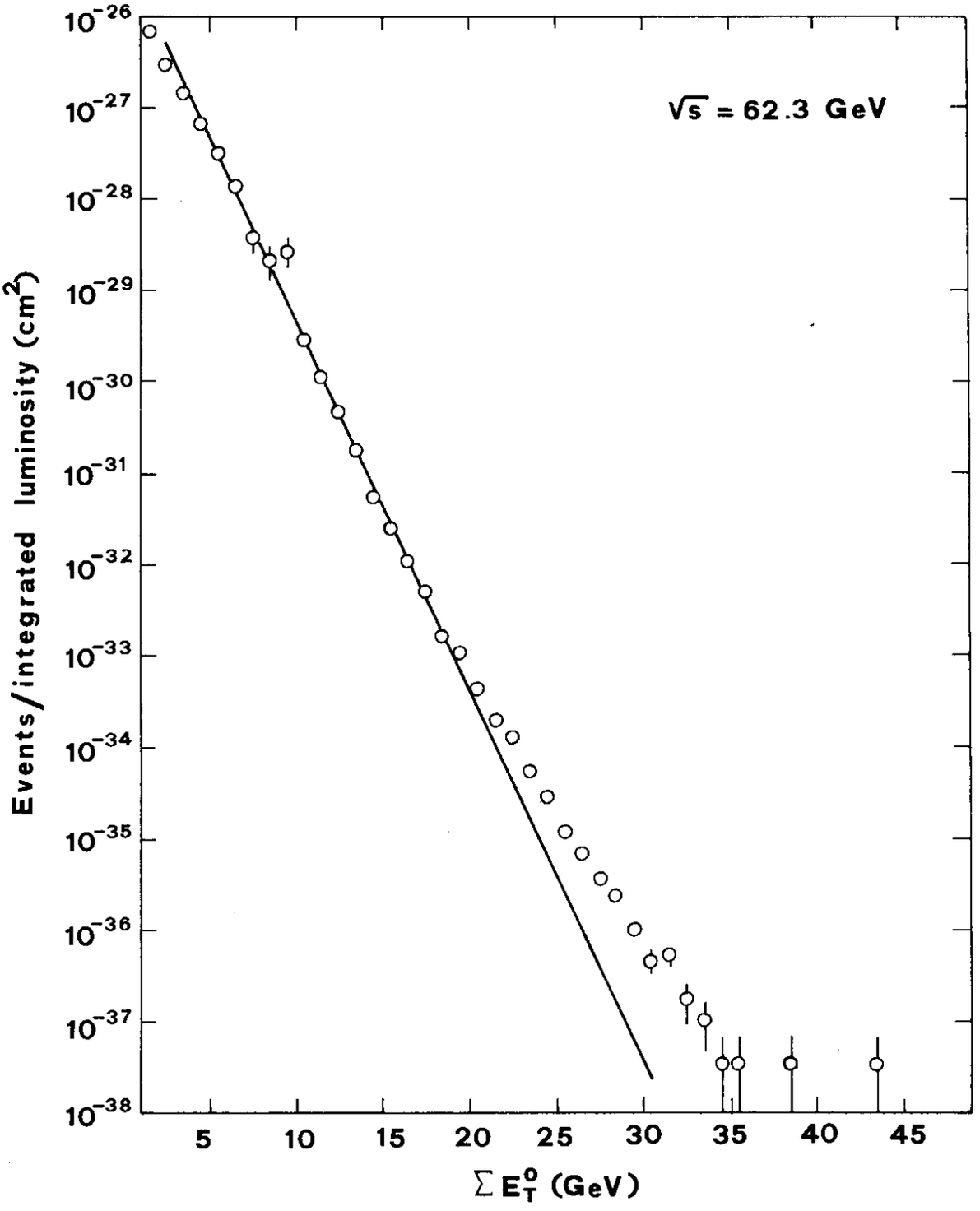
$\sqrt{s}$ = 62.3 GeV
Events/integrated luminosity (cm^2)
10^{-26}
10^{-27}
10^{-28}
10^{-29}
10^{-30}
10^{-31}
10^{-32}
10^{-33}
10^{-34}
10^{-35}
10^{-36}
10^{-37}
10^{-38}
5
10
15
20
25
30
35
40
45
ΣE_T^0 (GeV)

Fig. 8

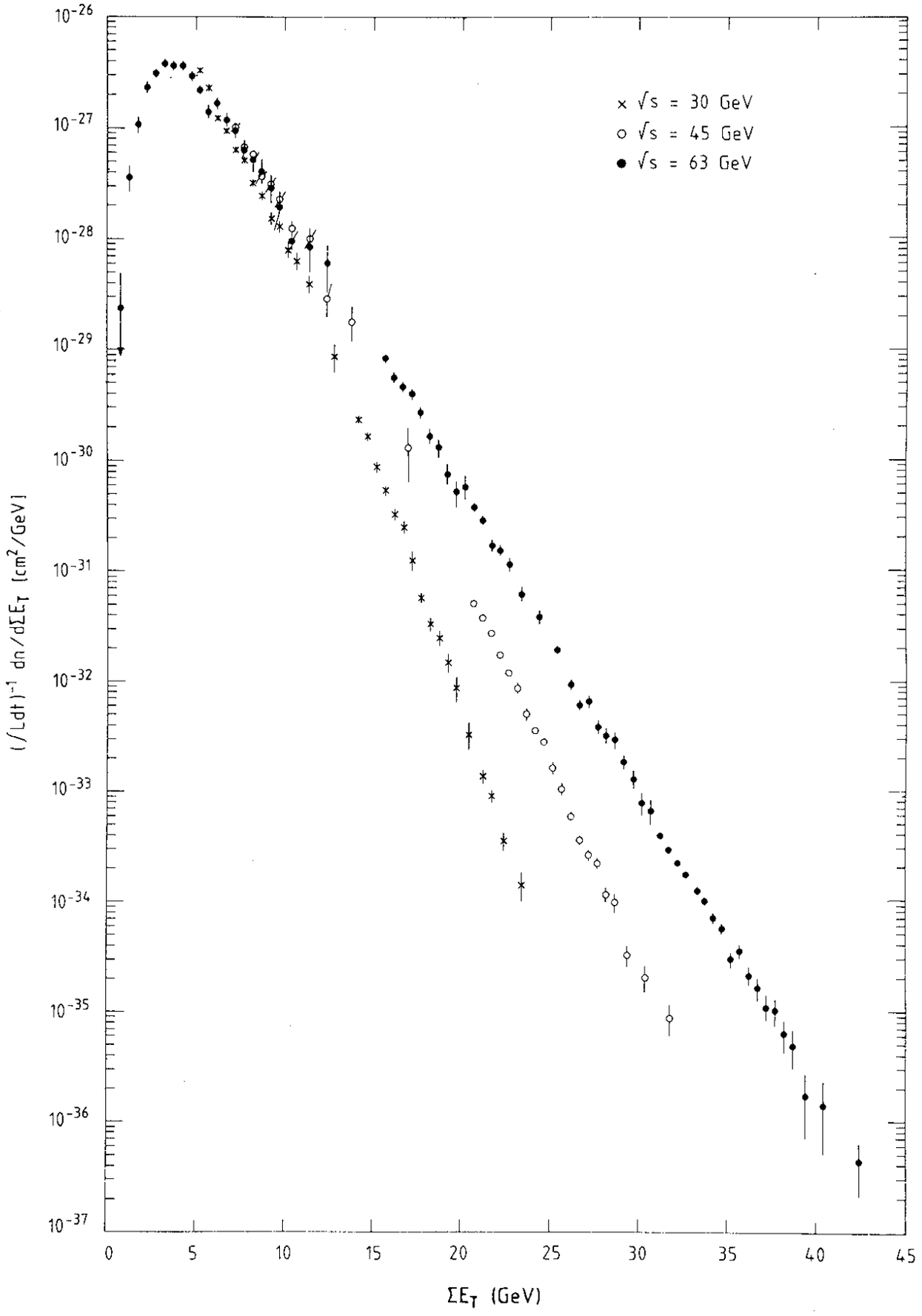
× √s = 30 GeV
○ √s = 45 GeV
● √s = 63 GeV
(∫Ldt)⁻¹ dn/dΣE_T [cm²/GeV]
ΣE_T (GeV)
10⁻²⁶
10⁻²⁷
10⁻²⁸
10⁻²⁹
10⁻³⁰
10⁻³¹
10⁻³²
10⁻³³
10⁻³⁴
10⁻³⁵
10⁻³⁶
10⁻³⁷
0
5
10
15
20
25
30
35
40
45

Fig. 9

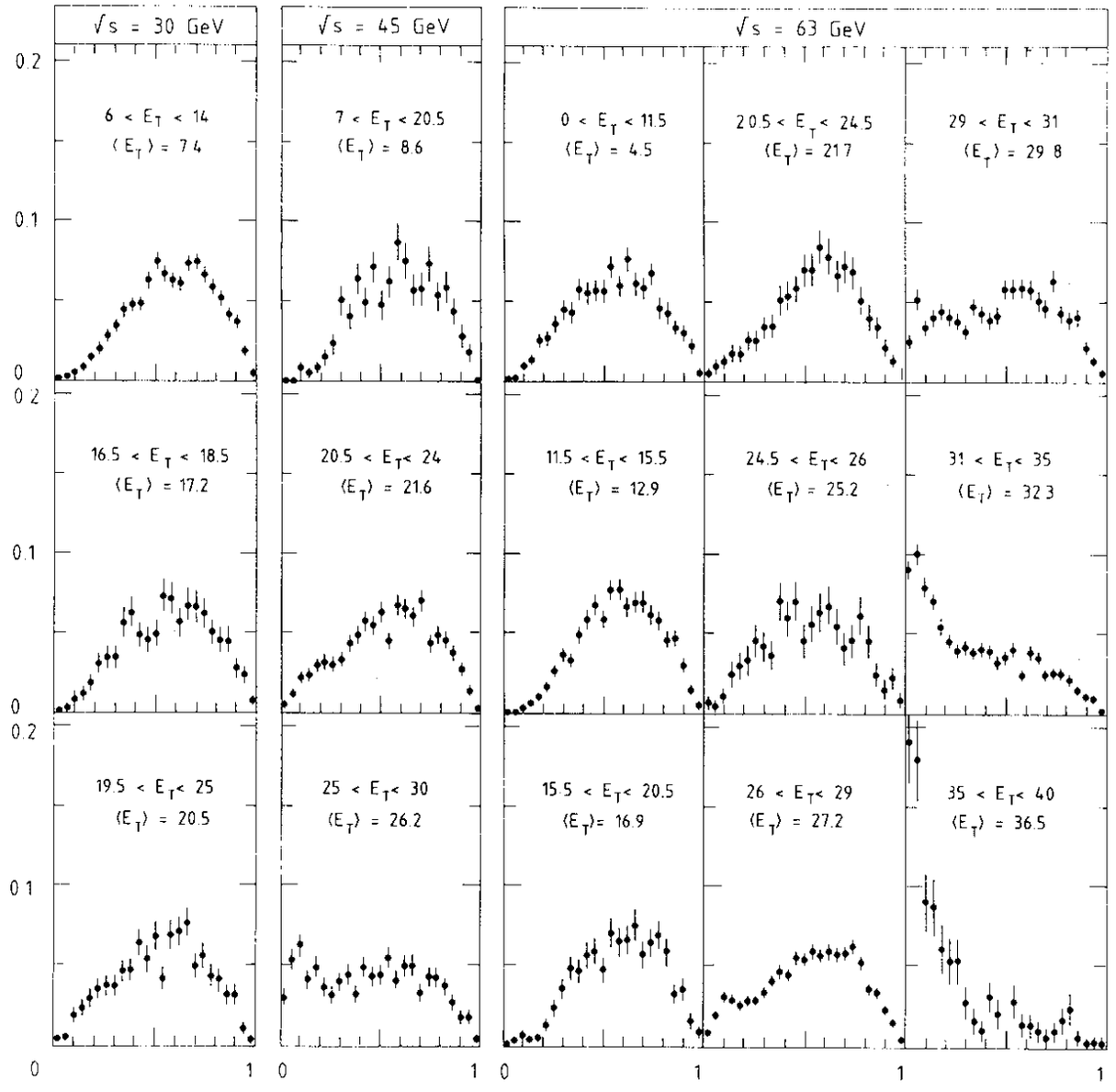
√s = 30 GeV
√s = 45 GeV
√s = 63 GeV
6 < E_T < 14
⟨E_T⟩ = 7.4
7 < E_T < 20.5
⟨E_T⟩ = 8.6
0 < E_T < 11.5
⟨E_T⟩ = 4.5
20.5 < E_T < 24.5
⟨E_T⟩ = 21.7
29 < E_T < 31
⟨E_T⟩ = 29.8
16.5 < E_T < 18.5
⟨E_T⟩ = 17.2
20.5 < E_T < 24
⟨E_T⟩ = 21.6
11.5 < E_T < 15.5
⟨E_T⟩ = 12.9
24.5 < E_T < 26
⟨E_T⟩ = 25.2
31 < E_T < 35
⟨E_T⟩ = 32.3
19.5 < E_T < 25
⟨E_T⟩ = 20.5
25 < E_T < 30
⟨E_T⟩ = 26.2
15.5 < E_T < 20.5
⟨E_T⟩ = 16.9
26 < E_T < 29
⟨E_T⟩ = 27.2
35 < E_T < 40
⟨E_T⟩ = 36.5
0.2
0.1
0
1

Fig. 10

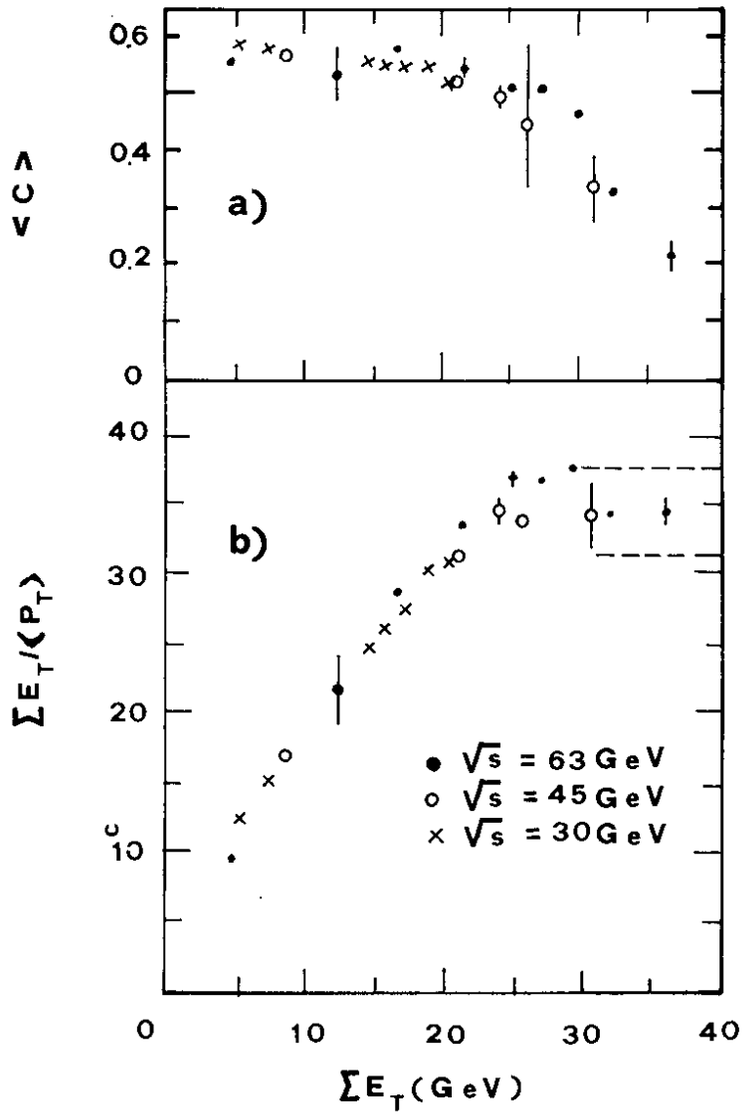
0.6
0.4
0.2
0
a)
< C >
40
30
20
10
b)
$\Sigma E_T/\langle P_T \rangle$
$\sqrt{s}$ = 63 GeV
$\sqrt{s}$ = 45 GeV
$\sqrt{s}$ = 30 GeV
0
10
20
30
40
ΣE_T (GeV)

Fig. 11

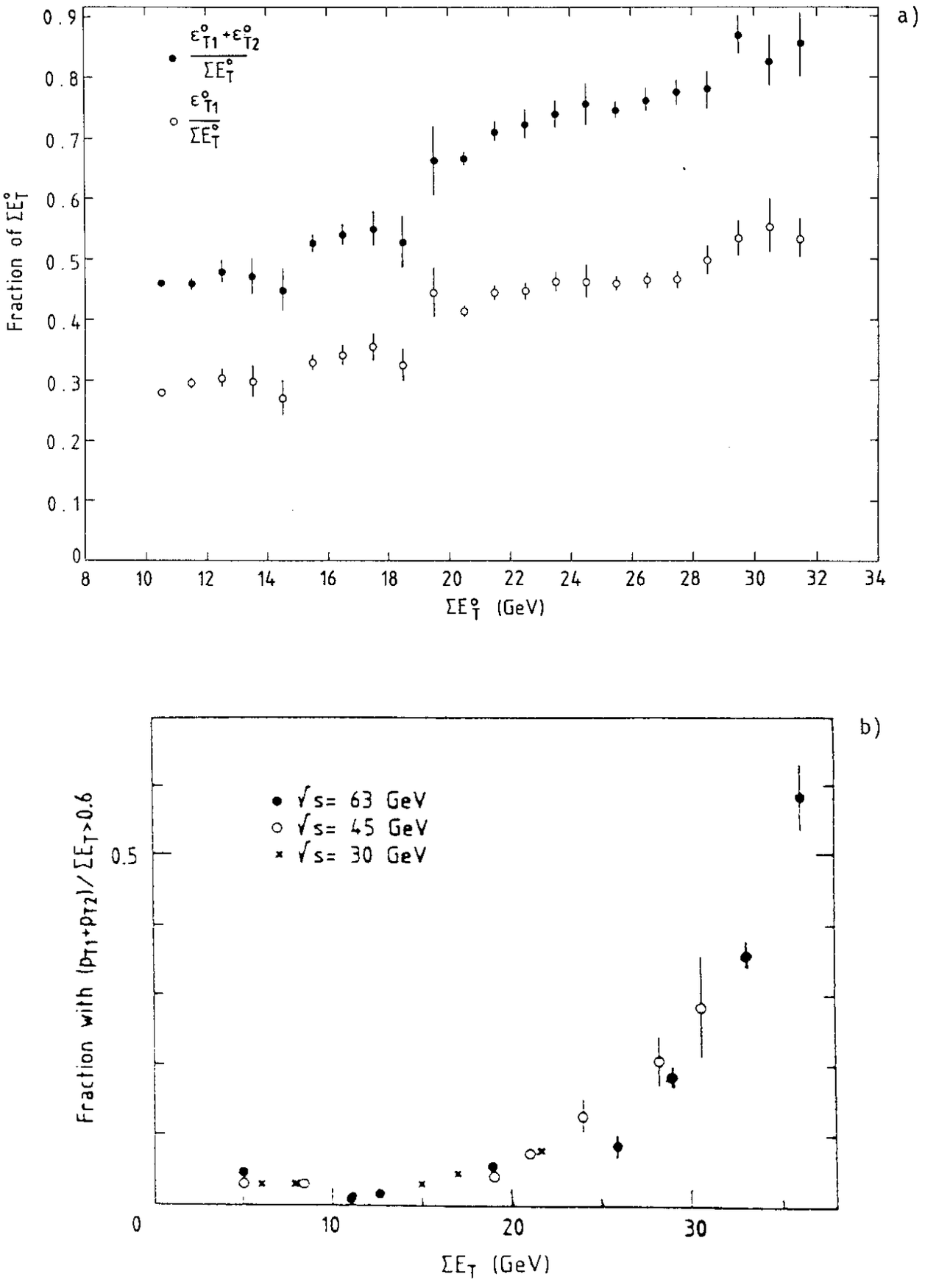
a)
Fraction of ΣE_T°
$\frac{\epsilon_{T1}^\circ + \epsilon_{T2}^\circ}{\Sigma E_T^\circ}$
$\frac{\epsilon_{T1}^\circ}{\Sigma E_T^\circ}$
ΣE_T° (GeV)
b)
Fraction with $(p_{T1}+p_{T2})/\Sigma E_T > 0.6$
$\sqrt{s}$= 63 GeV
$\sqrt{s}$= 45 GeV
$\sqrt{s}$= 30 GeV
ΣE_T (GeV)

Fig. 12

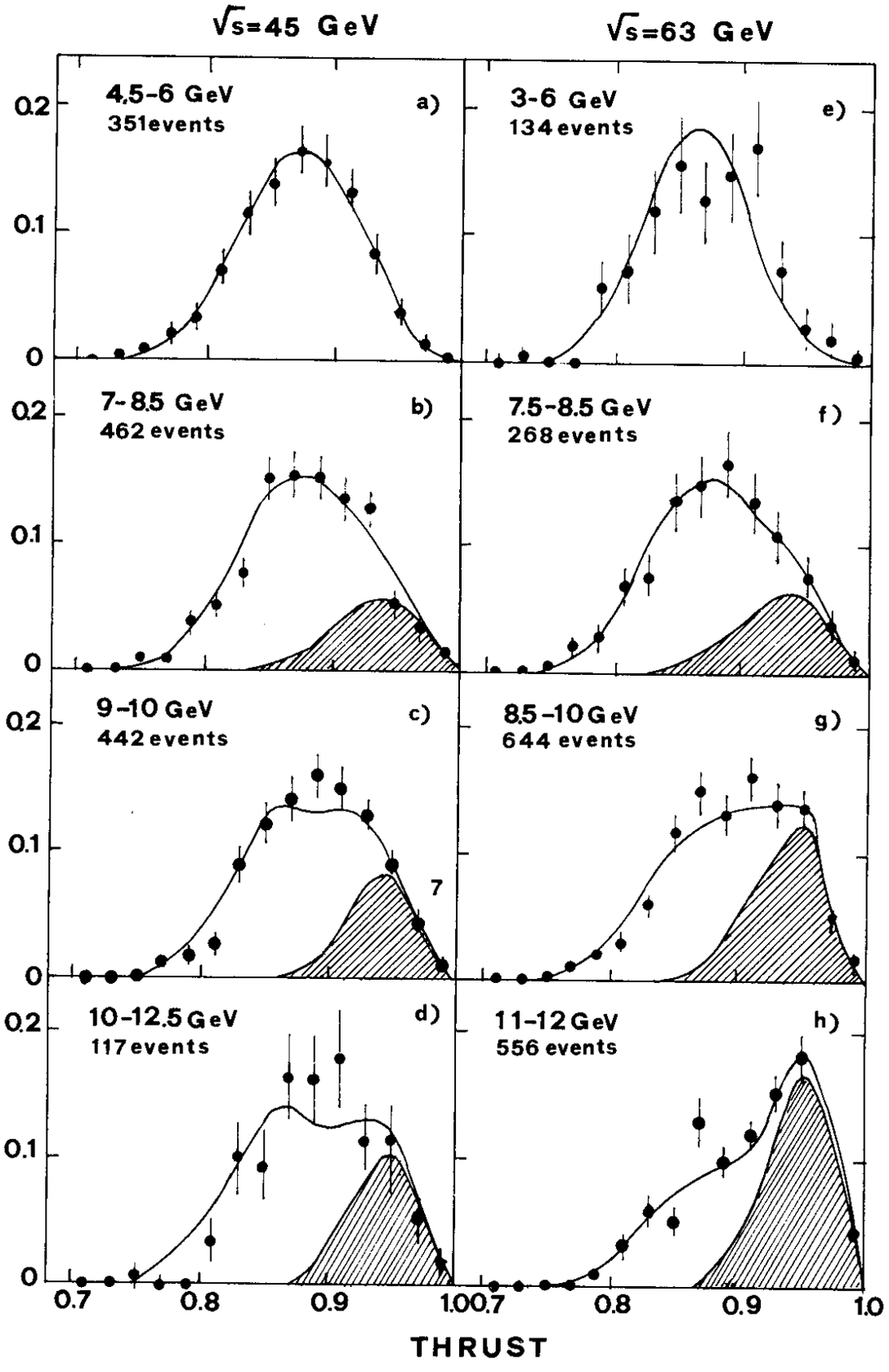
√s=45 GeV
√s=63 GeV
4.5-6 GeV
351events
a)
3-6 GeV
134 events
e)
7-8.5 GeV
462 events
b)
7.5-8.5 GeV
268 events
f)
9-10 GeV
442 events
c)
8.5-10 GeV
644 events
g)
10-12.5 GeV
117 events
d)
11-12 GeV
556 events
h)
0.2
0.1
0
0.7
0.8
0.9
1.0
THRUST

Fig. 13

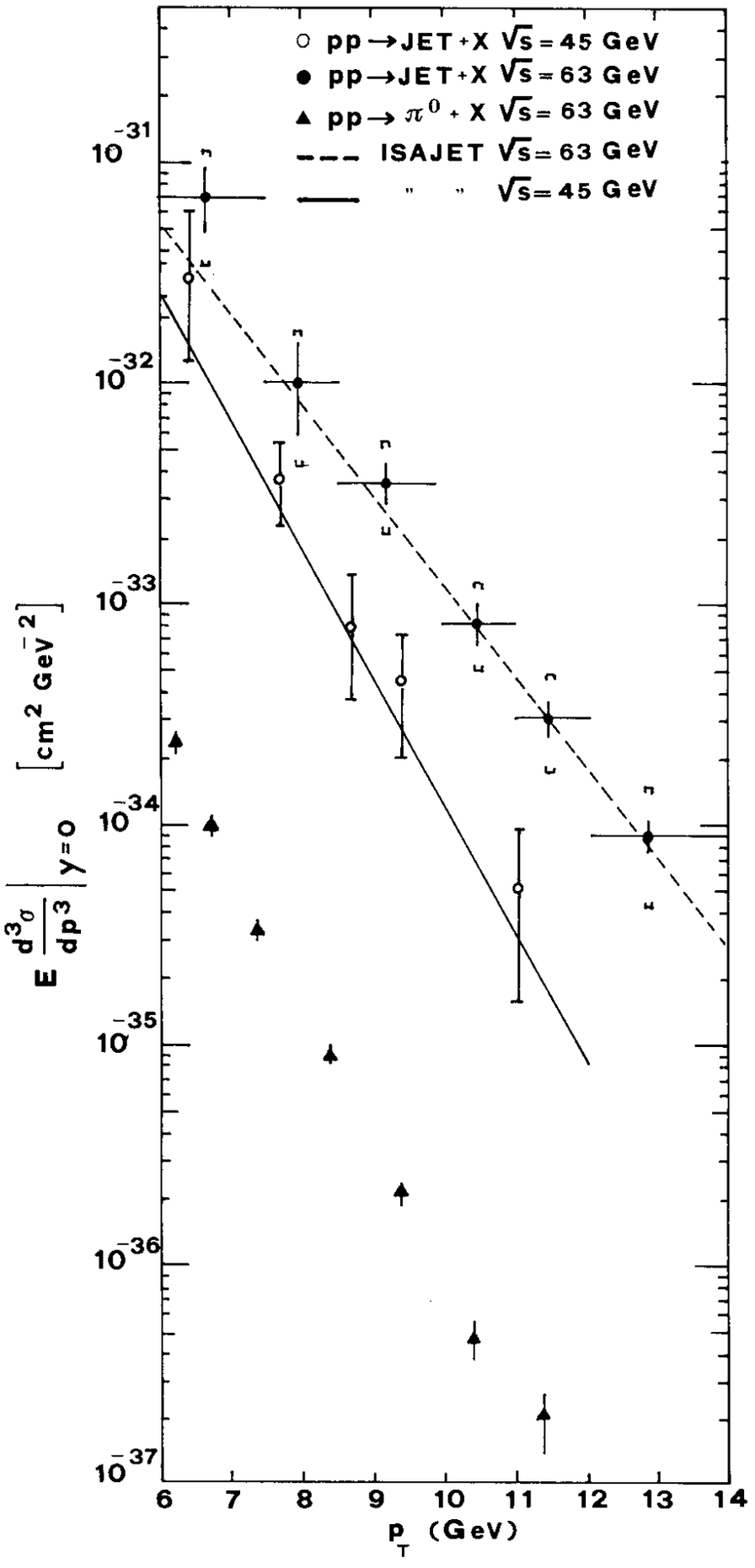
pp → JET + X √s = 45 GeV
pp → JET + X √s = 63 GeV
pp → π⁰ + X √s = 63 GeV
ISAJET √s = 63 GeV
" " √s = 45 GeV
E d³σ/dp³ | y=0 [cm² GeV⁻²]
10⁻³¹
10⁻³²
10⁻³³
10⁻³⁴
10⁻³⁵
10⁻³⁶
10⁻³⁷
6
7
8
9
10
11
12
13
14
p_T (GeV)

Fig. 14

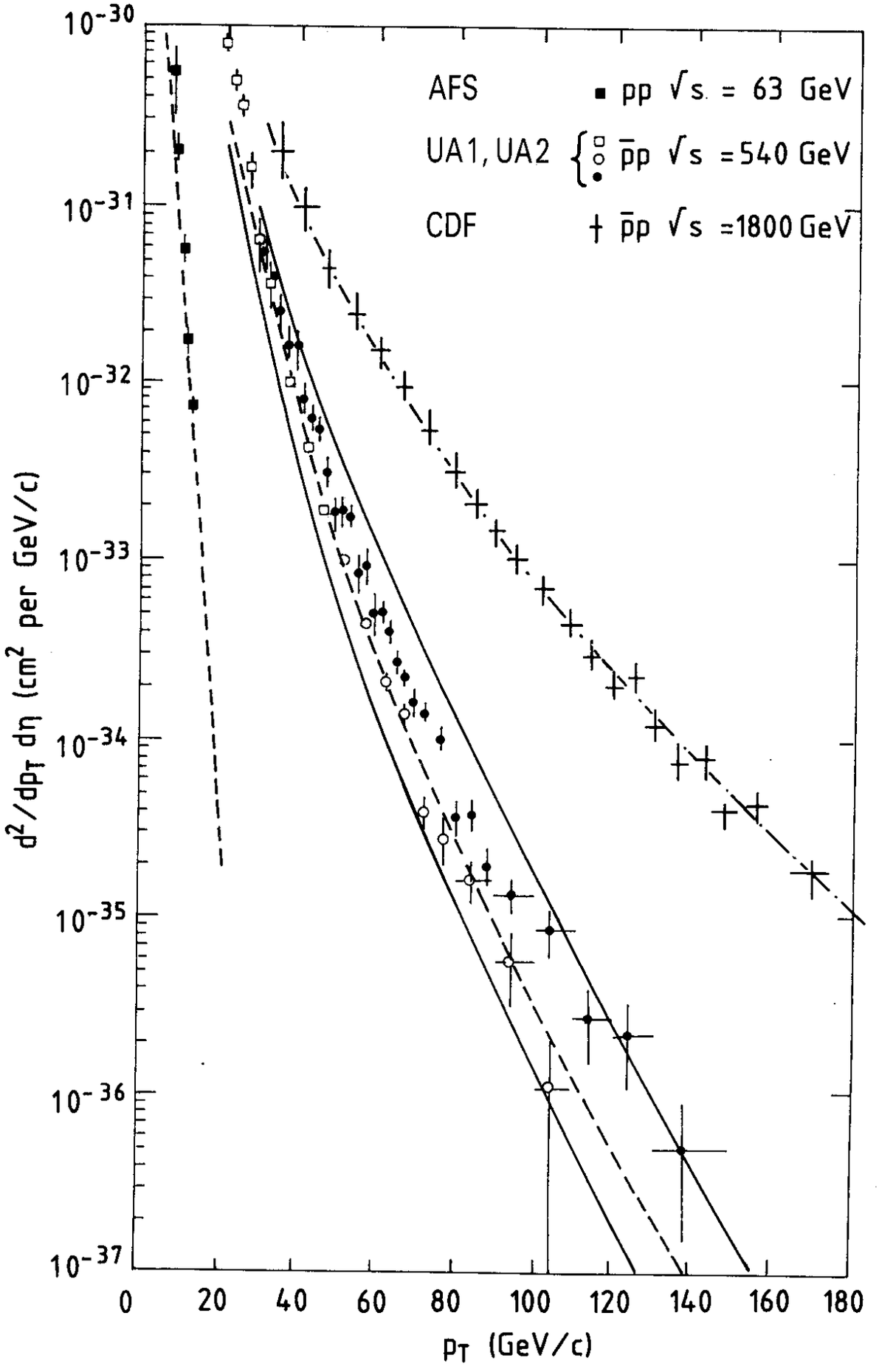
AFS
pp √s = 63 GeV
UA1, UA2
p̄p √s = 540 GeV
CDF
p̄p √s = 1800 GeV
d²/dp_T dη (cm² per GeV/c)
p_T (GeV/c)
10⁻³⁰
10⁻³¹
10⁻³²
10⁻³³
10⁻³⁴
10⁻³⁵
10⁻³⁶
10⁻³⁷
0
20
40
60
80
100
120
140
160
180

Fig. 15

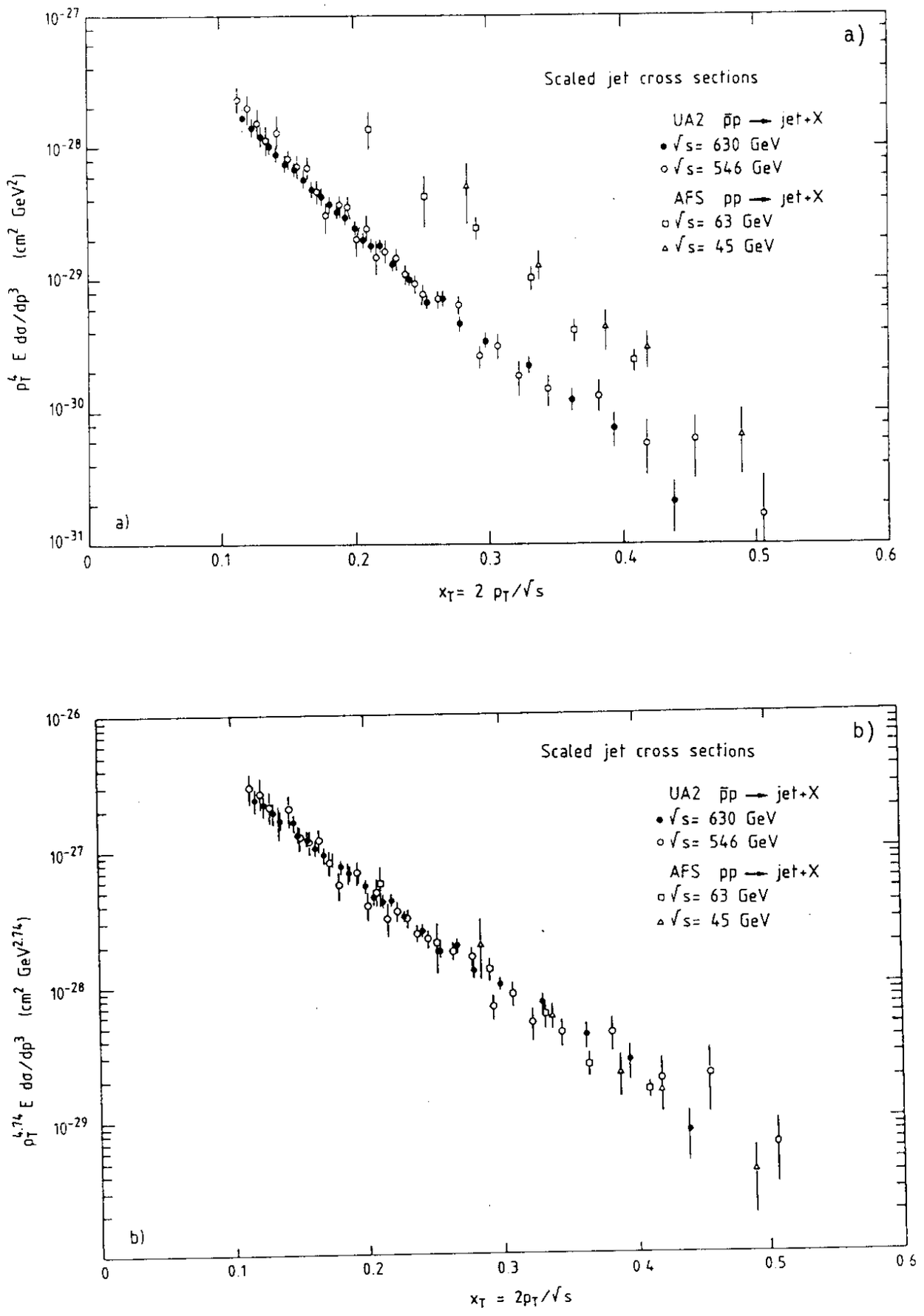
a)
Scaled jet cross sections
UA2 $\bar{p}p \rightarrow$ jet+X
• $\sqrt{s}$= 630 GeV
○ $\sqrt{s}$= 546 GeV
AFS pp → jet+X
□ $\sqrt{s}$= 63 GeV
△ $\sqrt{s}$= 45 GeV
p_T^4 E dσ/dp^3 (cm^2 GeV^2)
x_T= 2 $p_T/\sqrt{s}$
b)
Scaled jet cross sections
UA2 $\bar{p}p \rightarrow$ jet+X
• $\sqrt{s}$= 630 GeV
○ $\sqrt{s}$= 546 GeV
AFS pp → jet+X
□ $\sqrt{s}$= 63 GeV
△ $\sqrt{s}$= 45 GeV
$p_T^{4.74}$ E dσ/dp^3 (cm^2 GeV$^{2.74}$)
x_T = 2$p_T/\sqrt{s}$

Fig. 16

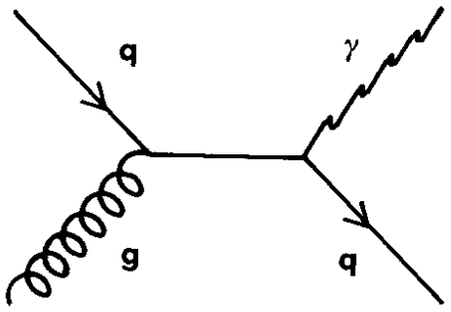

Compton

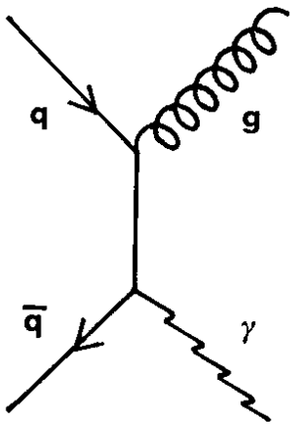

Annihilation

Fig. 17

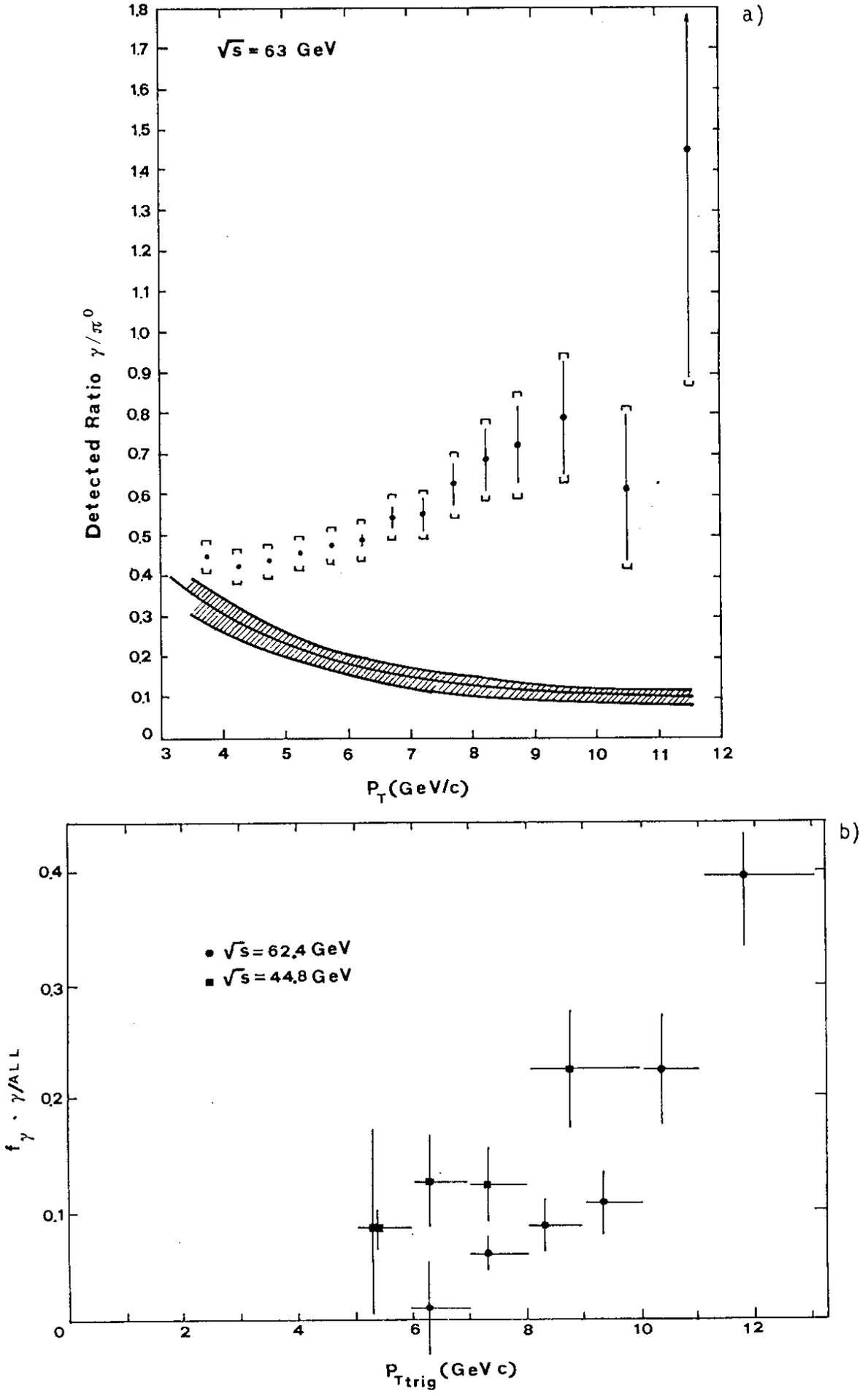
a)
$\sqrt{s}$ = 63 GeV
Detected Ratio γ/π^0
P_T(GeV/c)
b)
• $\sqrt{s}$ = 62.4 GeV
■ $\sqrt{s}$ = 44.8 GeV
$f_\gamma \cdot \gamma/ALL$
P_{Ttrig} (GeV c)

Fig. 18

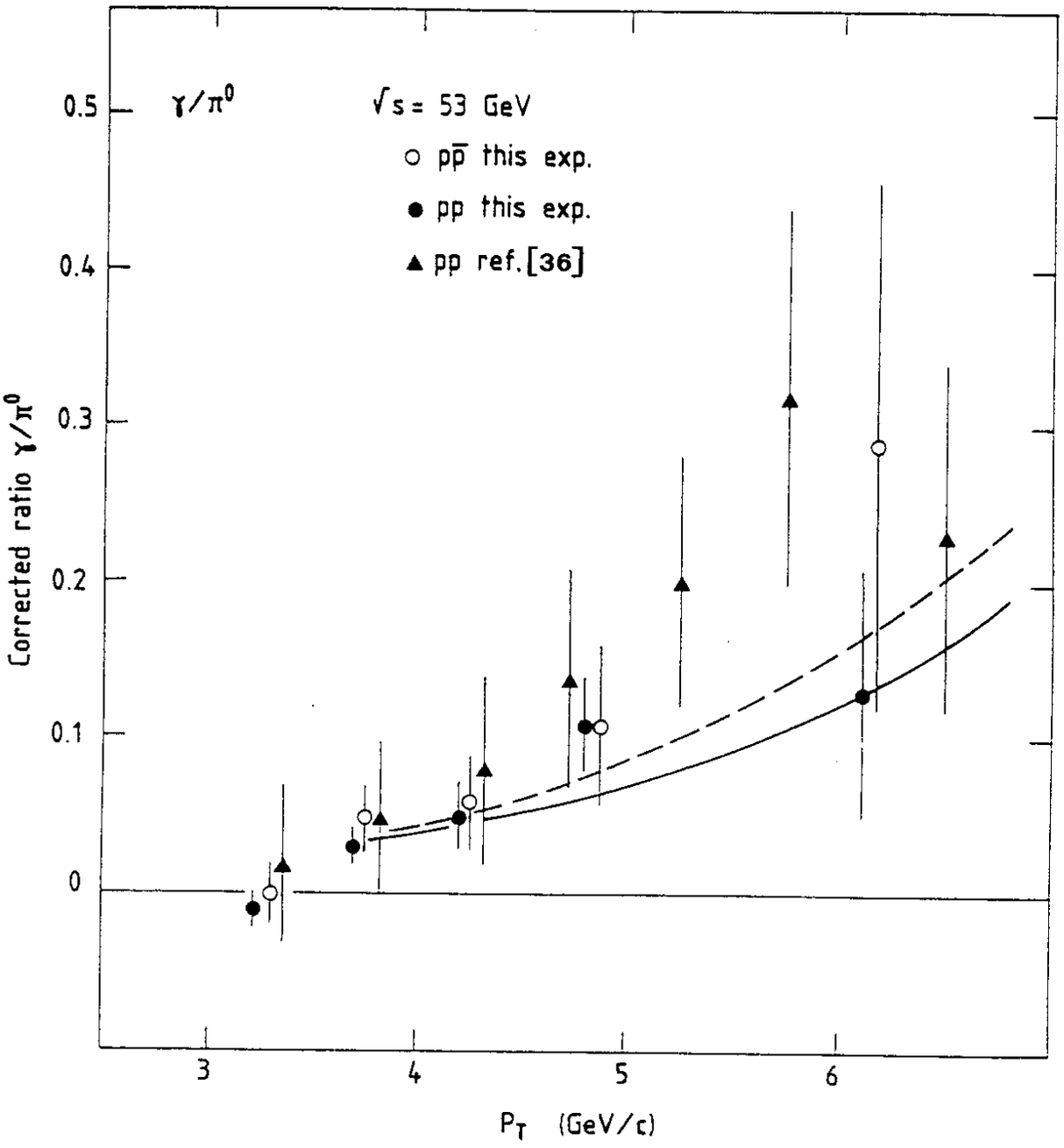
γ/π⁰
√s = 53 GeV
○ pp̄ this exp.
● pp this exp.
▲ pp ref.[36]
Corrected ratio γ/π⁰
0.5
0.4
0.3
0.2
0.1
0
3
4
5
6
P_T (GeV/c)

Fig. 19

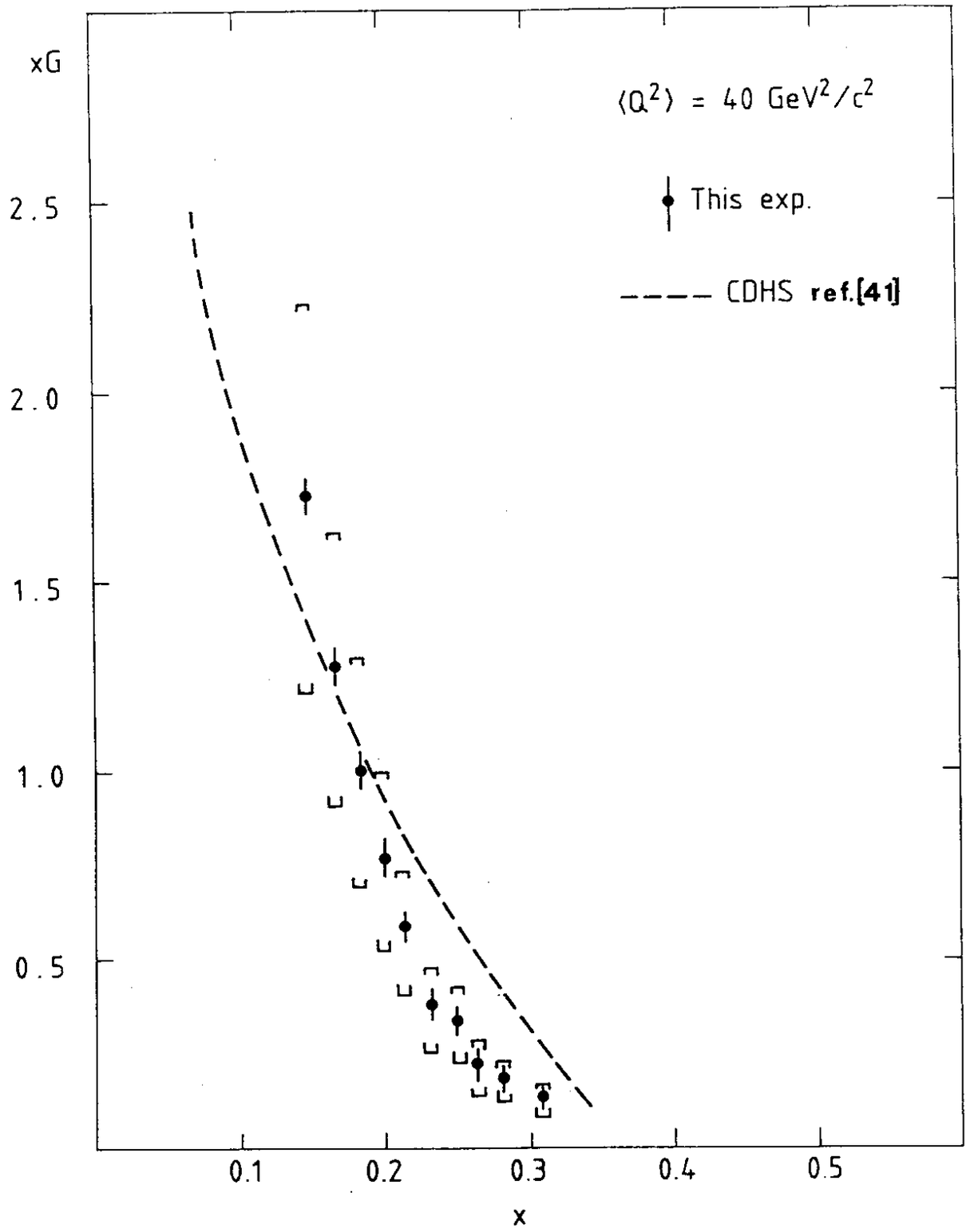
xG
$\langle Q^2 \rangle$ = 40 GeV^2/c^2
This exp.
CDHS ref.[41]
2.5
2.0
1.5
1.0
0.5
0.1
0.2
0.3
0.4
0.5
x

Fig. 20

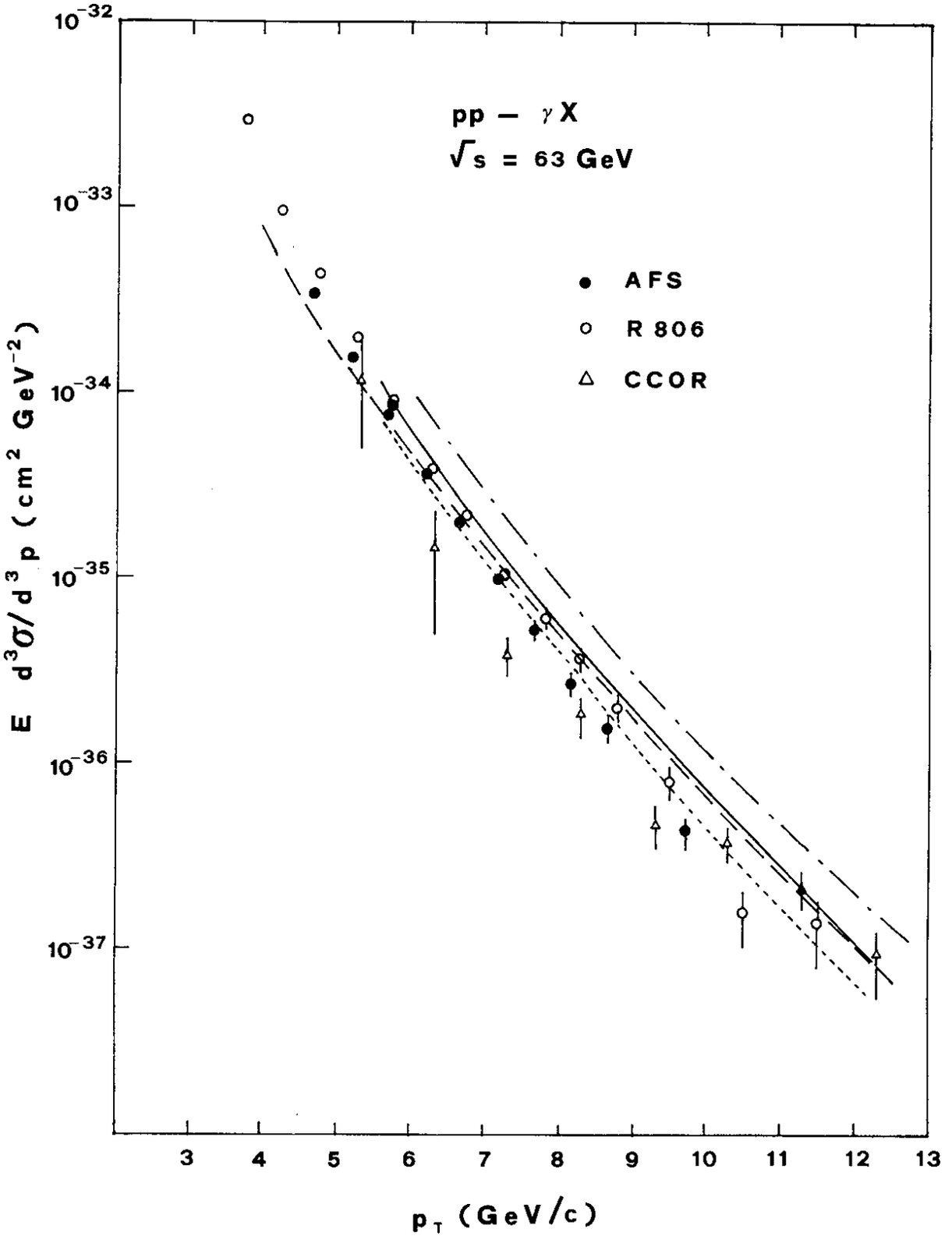
pp — γ X
√s = 63 GeV
AFS
R 806
CCOR
E d³σ/d³p (cm² GeV⁻²)
p_T (GeV/c)
10⁻³²
10⁻³³
10⁻³⁴
10⁻³⁵
10⁻³⁶
10⁻³⁷
3
4
5
6
7
8
9
10
11
12
13

Fig. 21

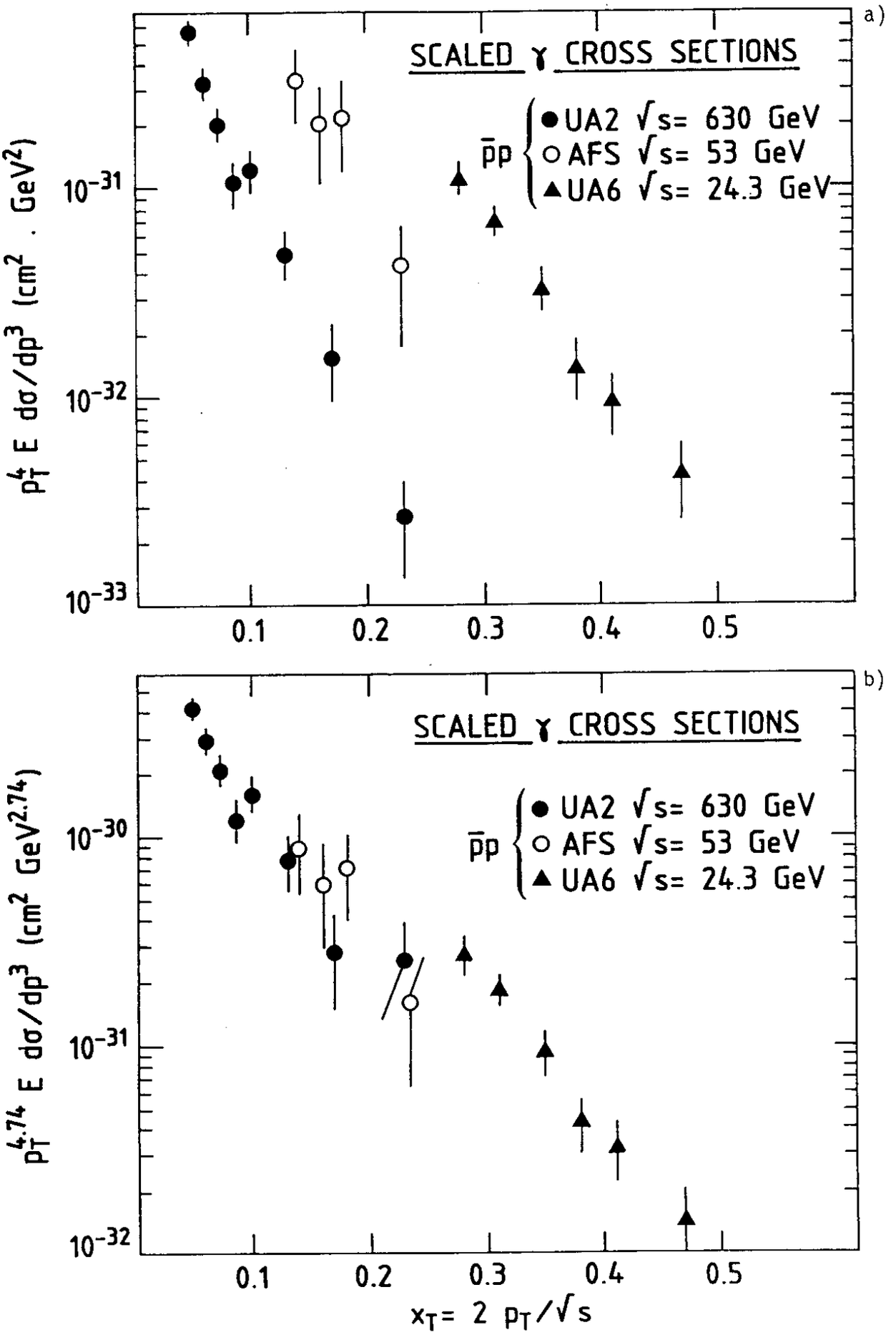
a)
SCALED γ CROSS SECTIONS
p̄p
UA2 √s= 630 GeV
AFS √s= 53 GeV
UA6 √s= 24.3 GeV
$p_T^4 E\, d\sigma/dp^3$ (cm^2 . GeV^2)
10^{-31}
10^{-32}
10^{-33}
0.1
0.2
0.3
0.4
0.5
b)
SCALED γ CROSS SECTIONS
p̄p
UA2 √s= 630 GeV
AFS √s= 53 GeV
UA6 √s= 24.3 GeV
$p_T^{4.74} E\, d\sigma/dp^3$ (cm^2 GeV$^{2.74}$)
10^{-30}
10^{-31}
10^{-32}
0.1
0.2
0.3
0.4
0.5
$x_T = 2\, p_T/\sqrt{s}$

Fig. 22

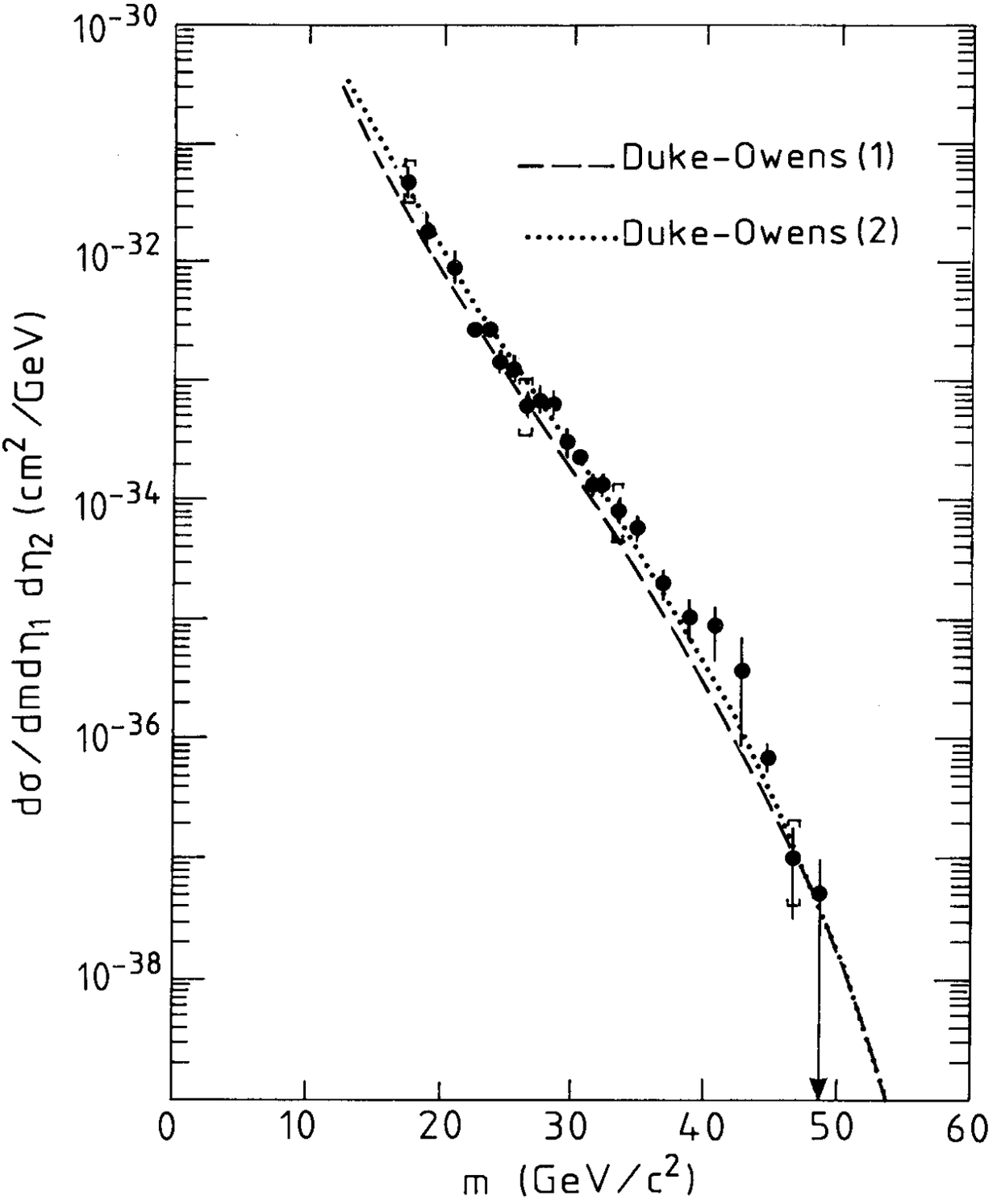
Duke-Owens (1)
Duke-Owens (2)
10^{-30}
10^{-32}
10^{-34}
10^{-36}
10^{-38}
$d\sigma/dm d\eta_1 d\eta_2$ (cm^2/GeV)
0
10
20
30
40
50
60
m (GeV/c^2)

Fig. 23

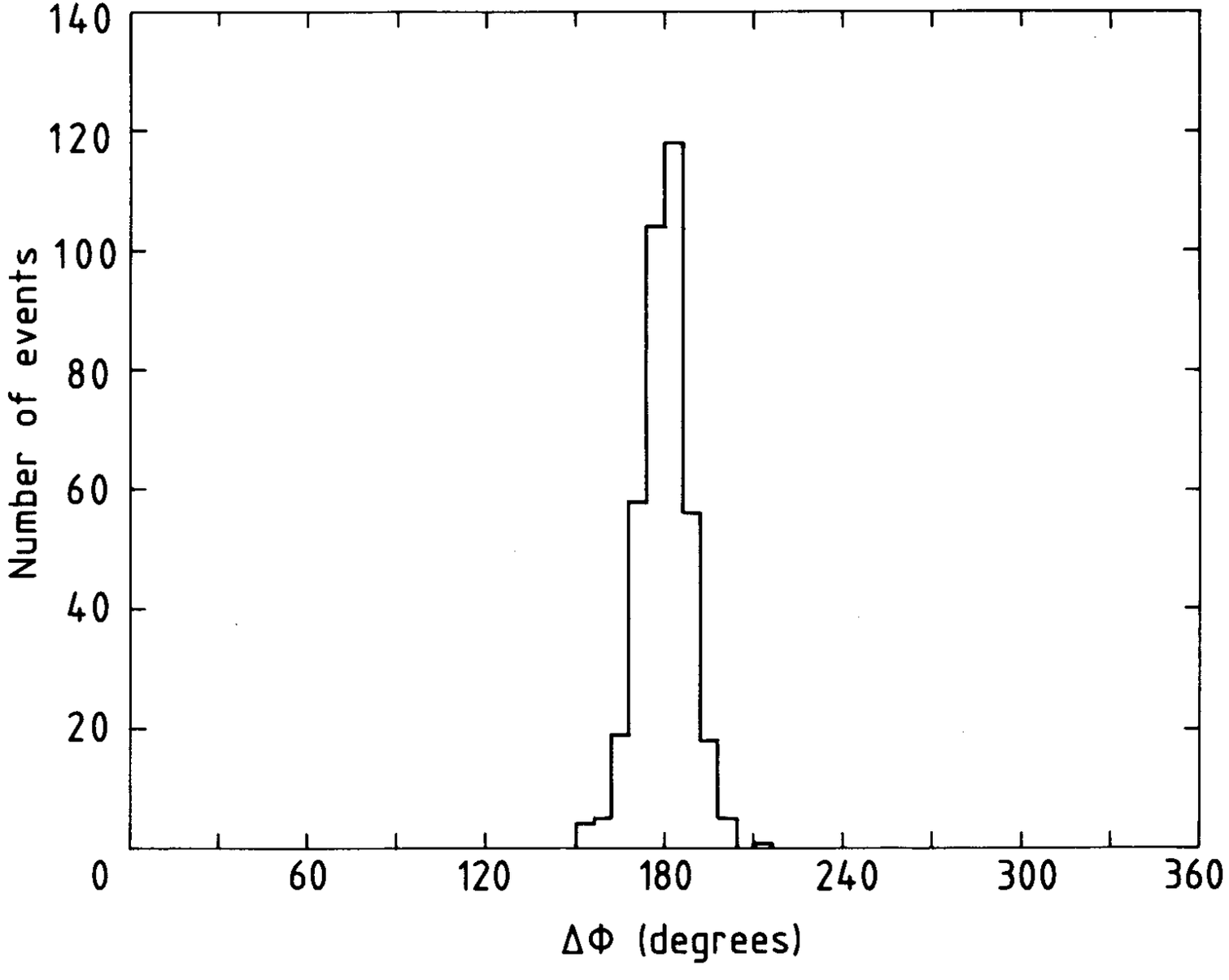
140
120
100
80
60
40
20
0
Number of events
60
120
180
240
300
360
ΔΦ (degrees)

Fig. 24

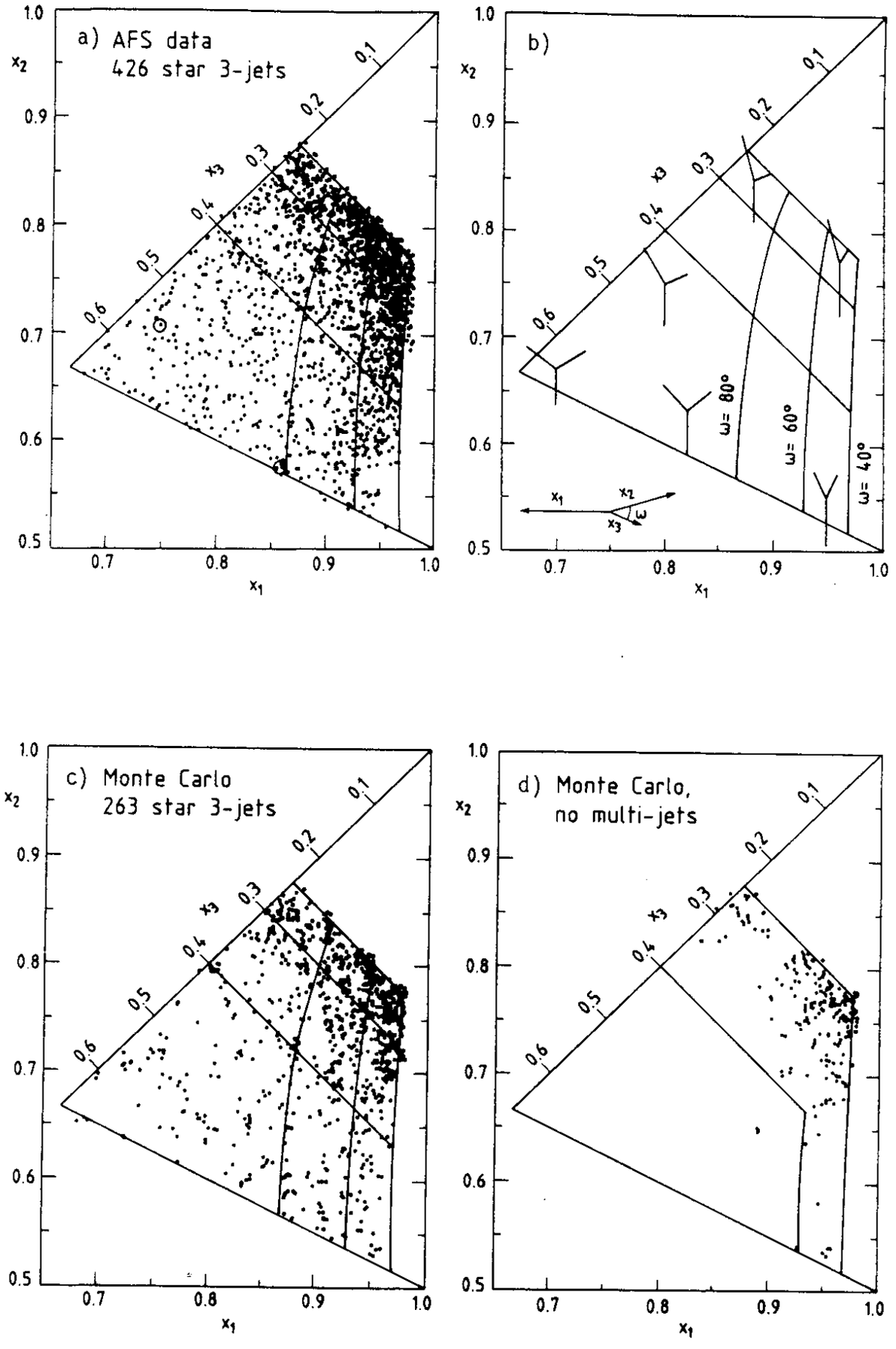
a) AFS data
426 star 3-jets
b)
c) Monte Carlo
263 star 3-jets
d) Monte Carlo,
no multi-jets
x_1
x_2
x_3
$\omega = 80°$
$\omega = 60°$
$\omega = 40°$

Fig. 25

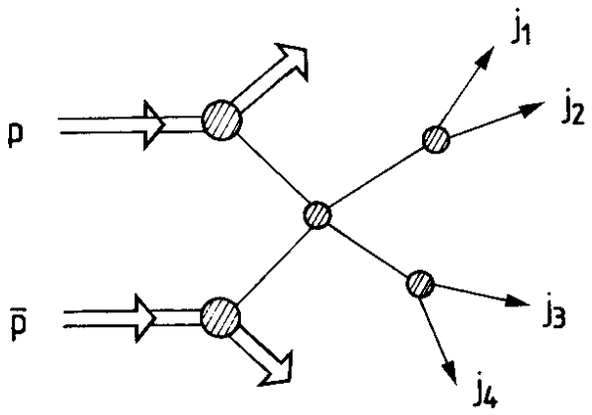

Bremsstrahlung (α_S^4)

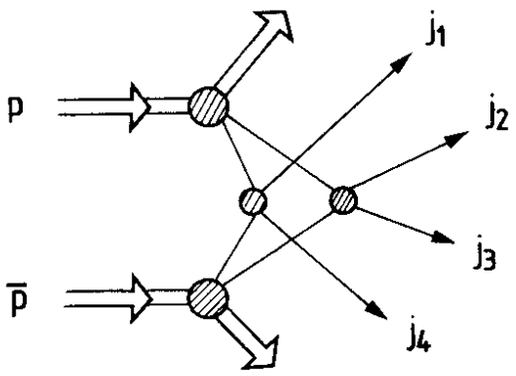

Double Parton
Scattering $2x(\alpha_S^2)$

Fig. 26

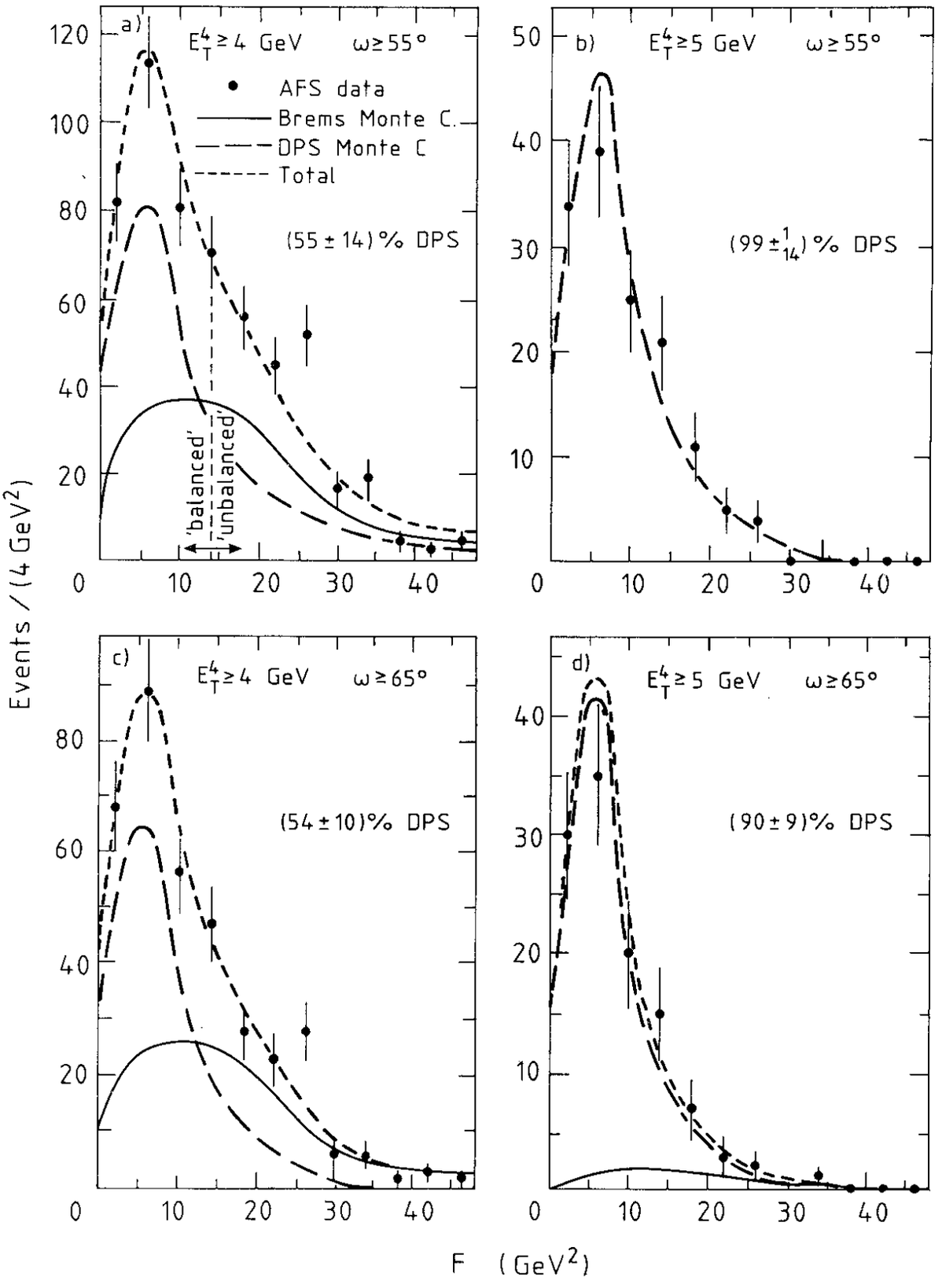
a)
$E_T^4 \geq 4$ GeV $\omega \geq 55°$
AFS data
Brems Monte C.
DPS Monte C
Total
(55 ± 14) % DPS
'balanced'
'unbalanced'
b)
$E_T^4 \geq 5$ GeV $\omega \geq 55°$
$(99 \pm {}^{1}_{14})$ % DPS
c)
$E_T^4 \geq 4$ GeV $\omega \geq 65°$
(54 ± 10) % DPS
d)
$E_T^4 \geq 5$ GeV $\omega \geq 65°$
(90 ± 9) % DPS
Events / (4 GeV^2)
F (GeV^2)

Fig. 27

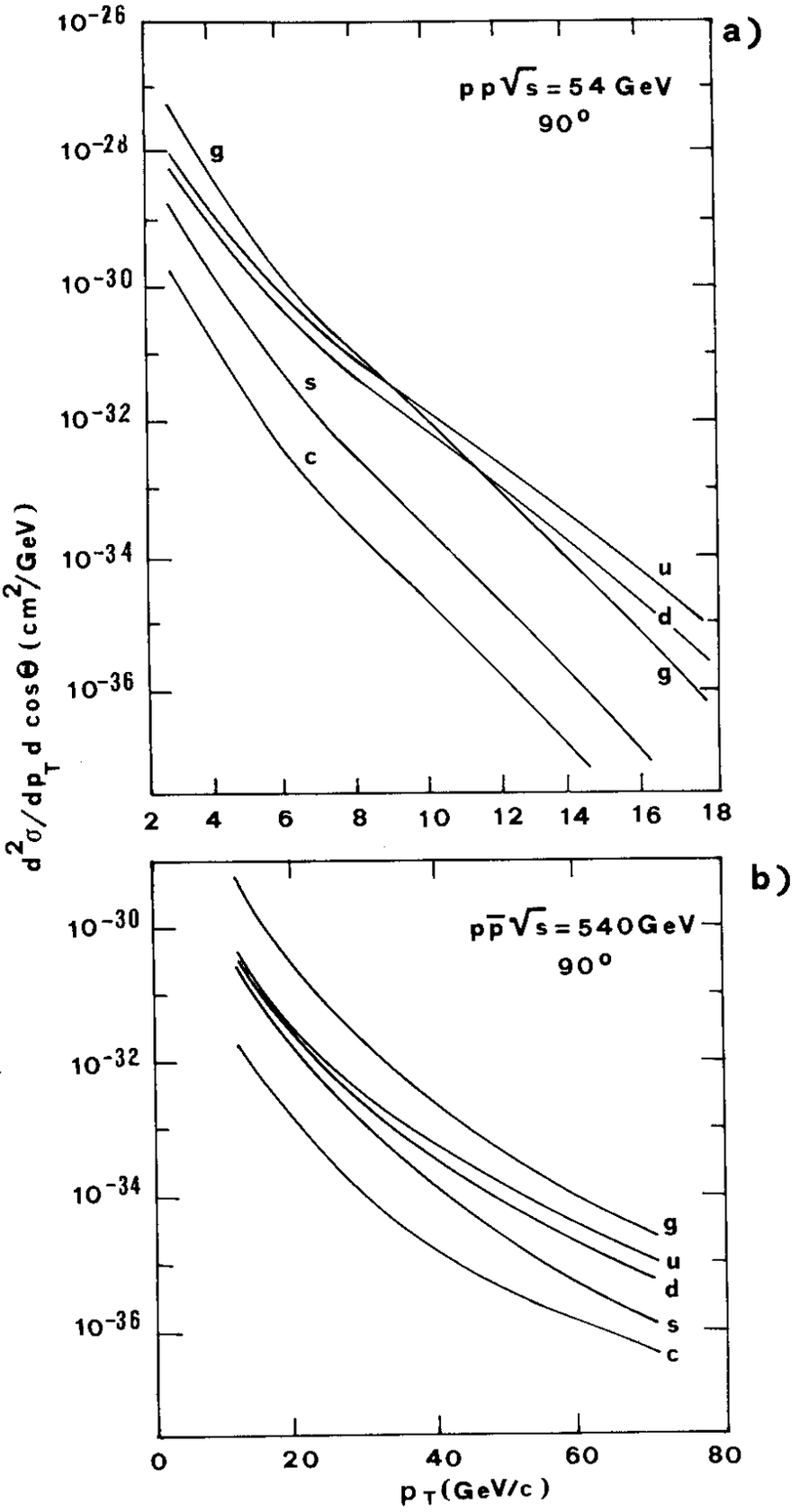
a)
$p\,p\sqrt{s} = 54$ GeV
90°
g
s
c
u
d
g
10^{-26}
10^{-28}
10^{-30}
10^{-32}
10^{-34}
10^{-36}
2 4 6 8 10 12 14 16 18
b)
$p\bar{p}\sqrt{s} = 540$ GeV
90°
g
u
d
s
c
10^{-30}
10^{-32}
10^{-34}
10^{-36}
0 20 40 60 80
p_T (GeV/c)
$d^2\sigma/dp_T\,d\cos\Theta$ (cm^2/GeV)

Fig. 28

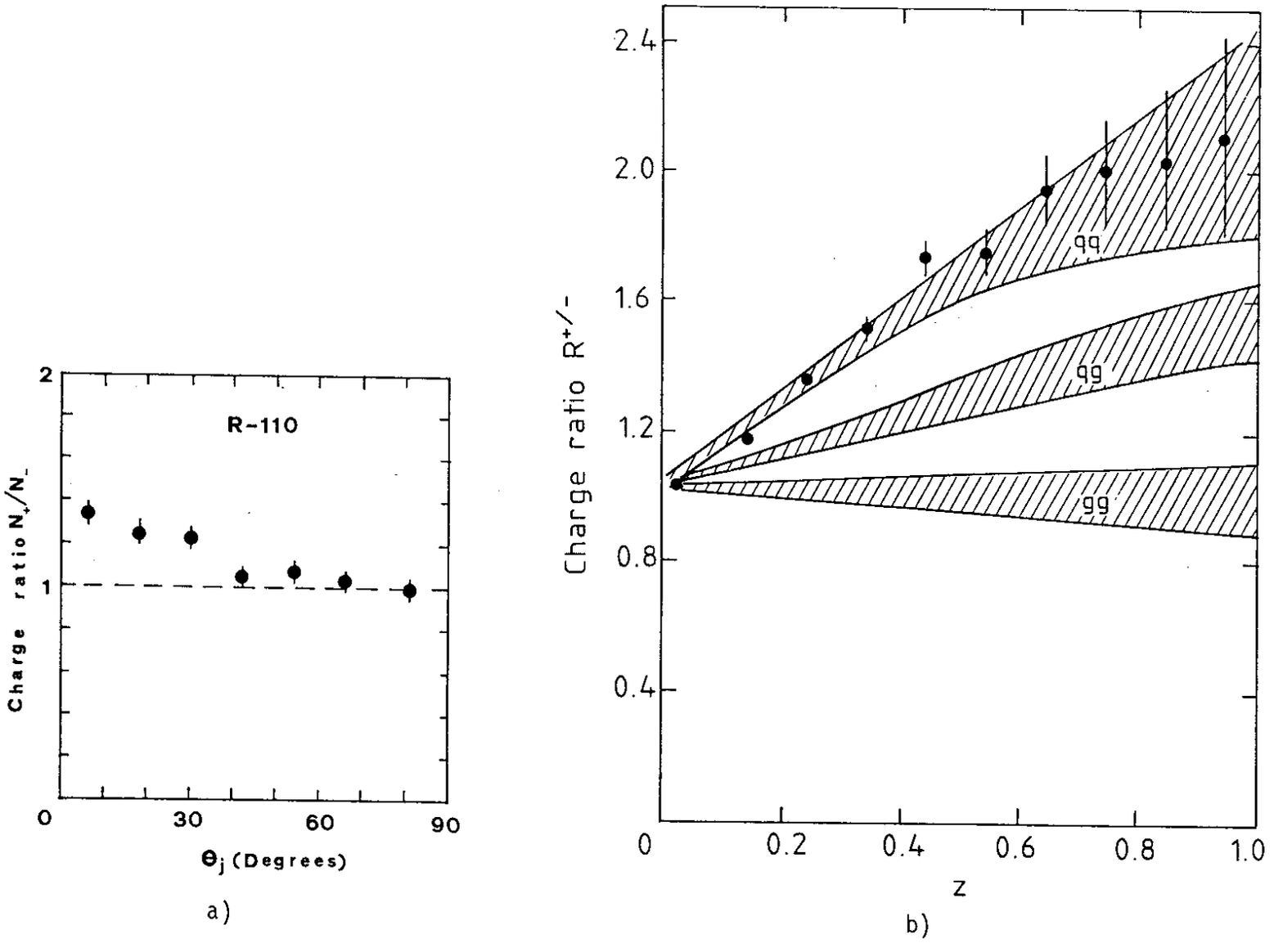
R-110
Charge ratio N_+/N_-
Θ_j (Degrees)
a)
Charge ratio $R^{+/-}$
z
qq
qq
qq
b)

Fig. 29

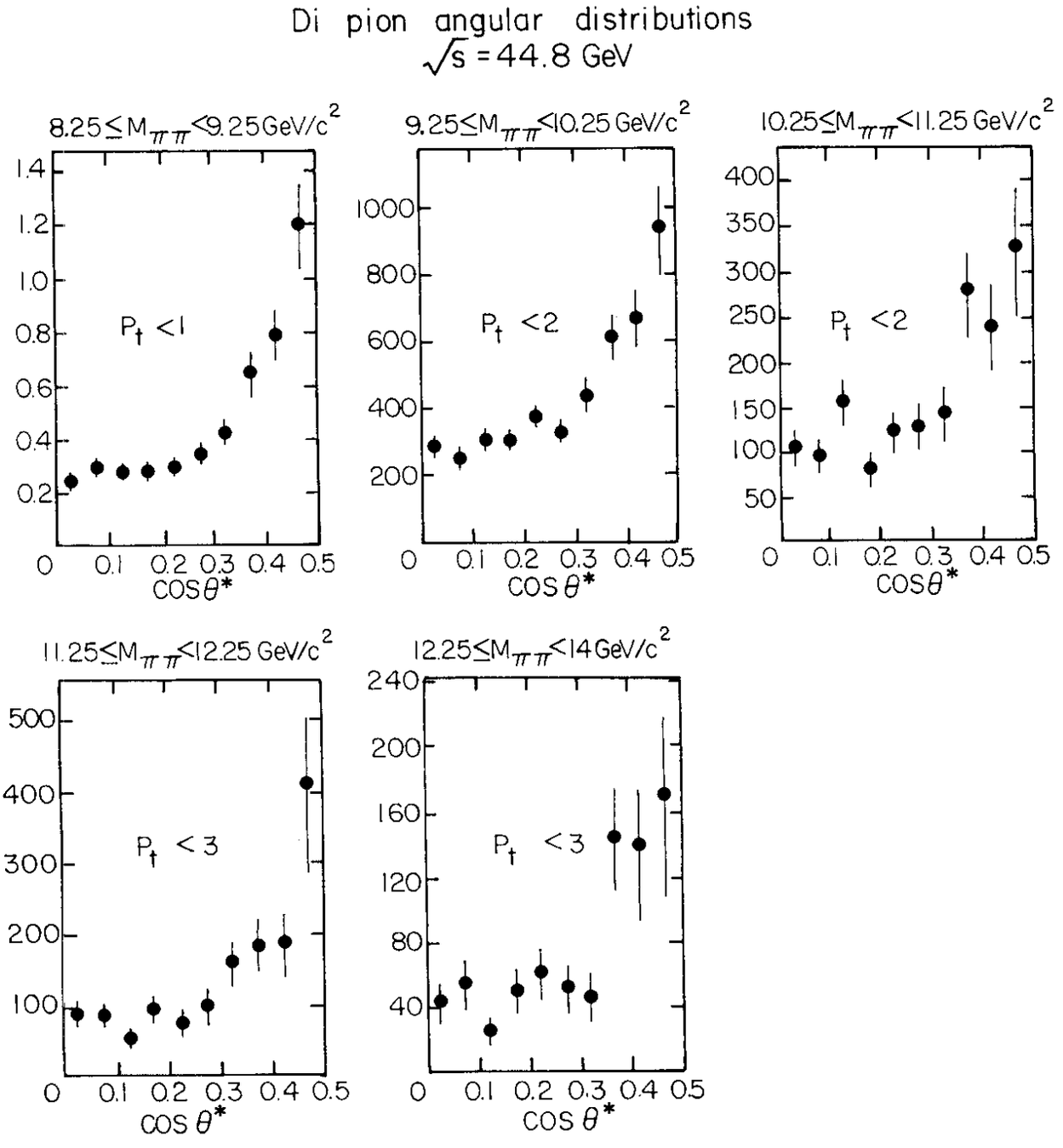
Di pion angular distributions
√s = 44.8 GeV
8.25≤M$_{\pi\pi}$<9.25 GeV/c^2
P$_t$ <1
9.25≤M$_{\pi\pi}$<10.25 GeV/c^2
P$_t$ <2
10.25≤M$_{\pi\pi}$<11.25 GeV/c^2
P$_t$ <2
11.25≤M$_{\pi\pi}$<12.25 GeV/c^2
P$_t$ <3
12.25≤M$_{\pi\pi}$<14 GeV/c^2
P$_t$ <3
COS θ*

Fig. 30

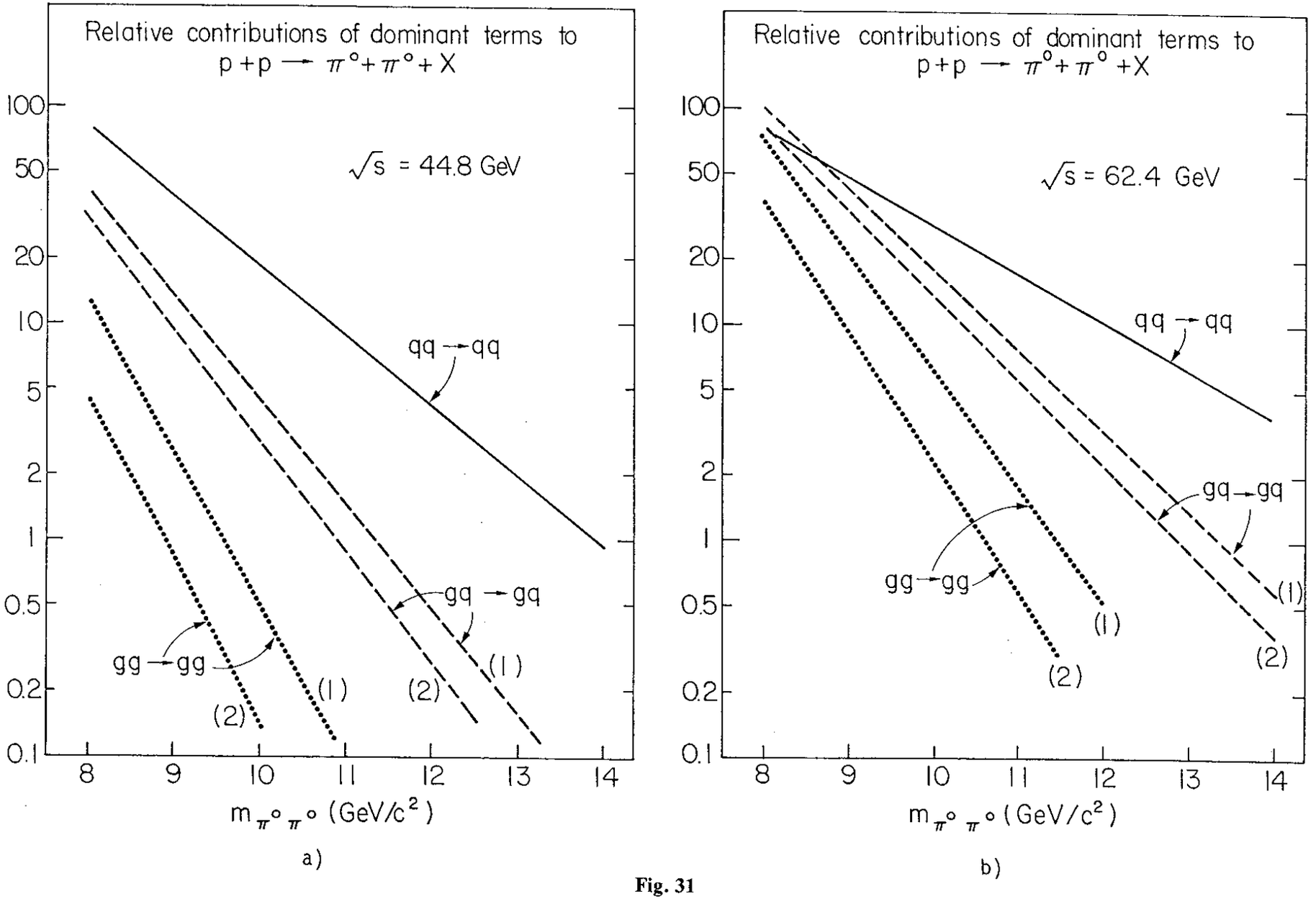
Relative contributions of dominant terms to
p + p → π° + π° + X
√s = 44.8 GeV
qq → qq
gq → gq
gg → gg
(1)
(2)
100
50
20
10
5
2
1
0.5
0.2
0.1
8
9
10
11
12
13
14
m π° π° (GeV/c²)
a)
Relative contributions of dominant terms to
p + p → π° + π° + X
√s = 62.4 GeV
qq → qq
gq → gq
gg → gg
(1)
(2)
m π° π° (GeV/c²)
b)

Fig. 31

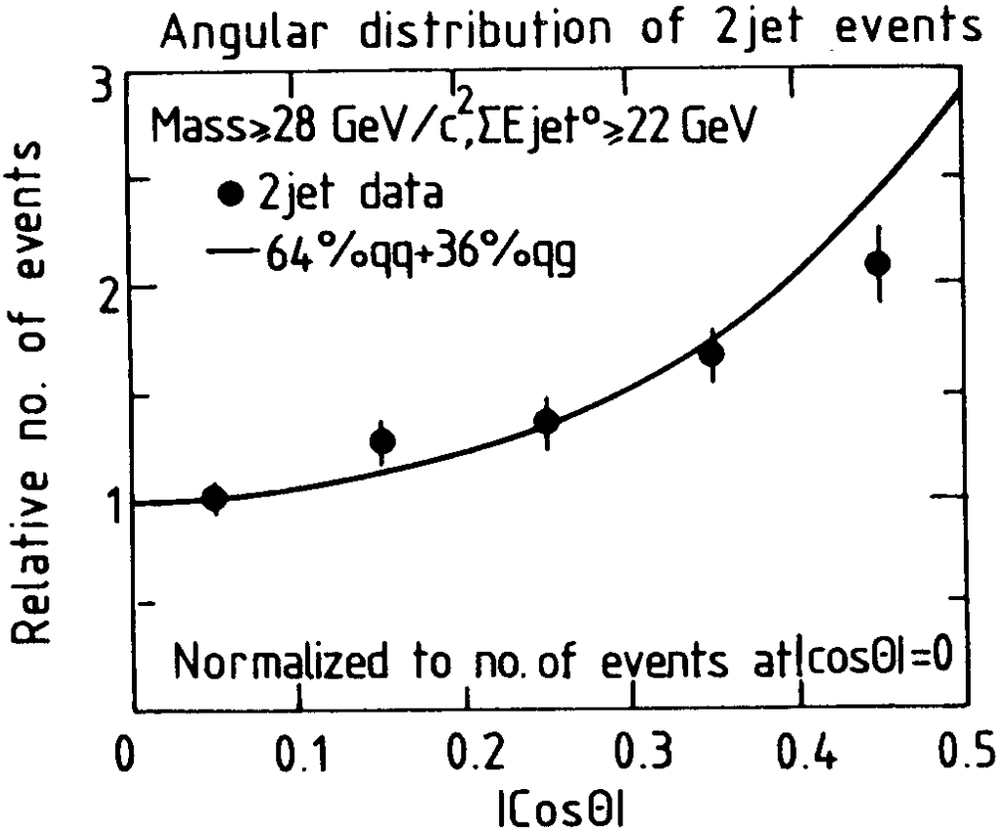
Angular distribution of 2jet events
Mass≥28 GeV/c², ΣEjet°≥22 GeV
● 2jet data
— 64%qq+36%qg
Normalized to no. of events at |cosΘ|=0
Relative no. of events
|CosΘ|
0
0.1
0.2
0.3
0.4
0.5
1
2
3

Fig. 32

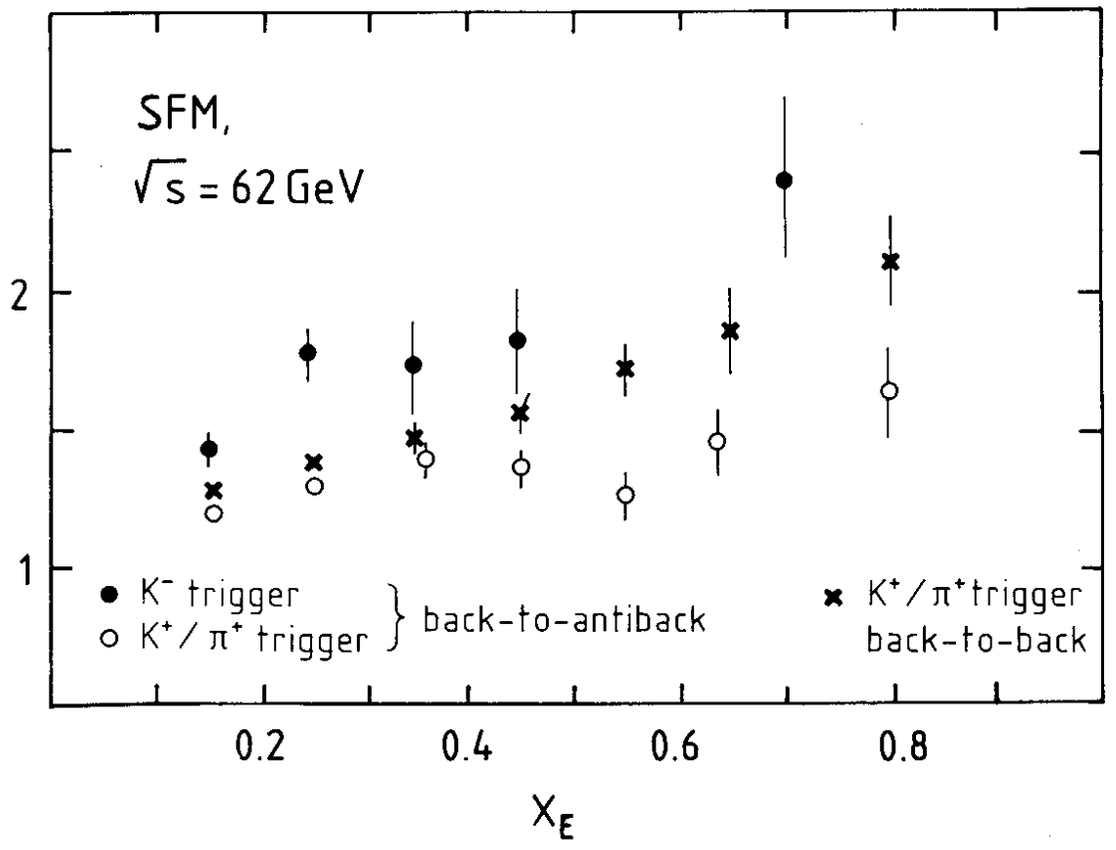
SFM,
√s = 62 GeV
2
1
K⁻ trigger
K⁺ / π⁺ trigger
back-to-antiback
K⁺ / π⁺ trigger
back-to-back
0.2
0.4
0.6
0.8
X_E

Fig. 33

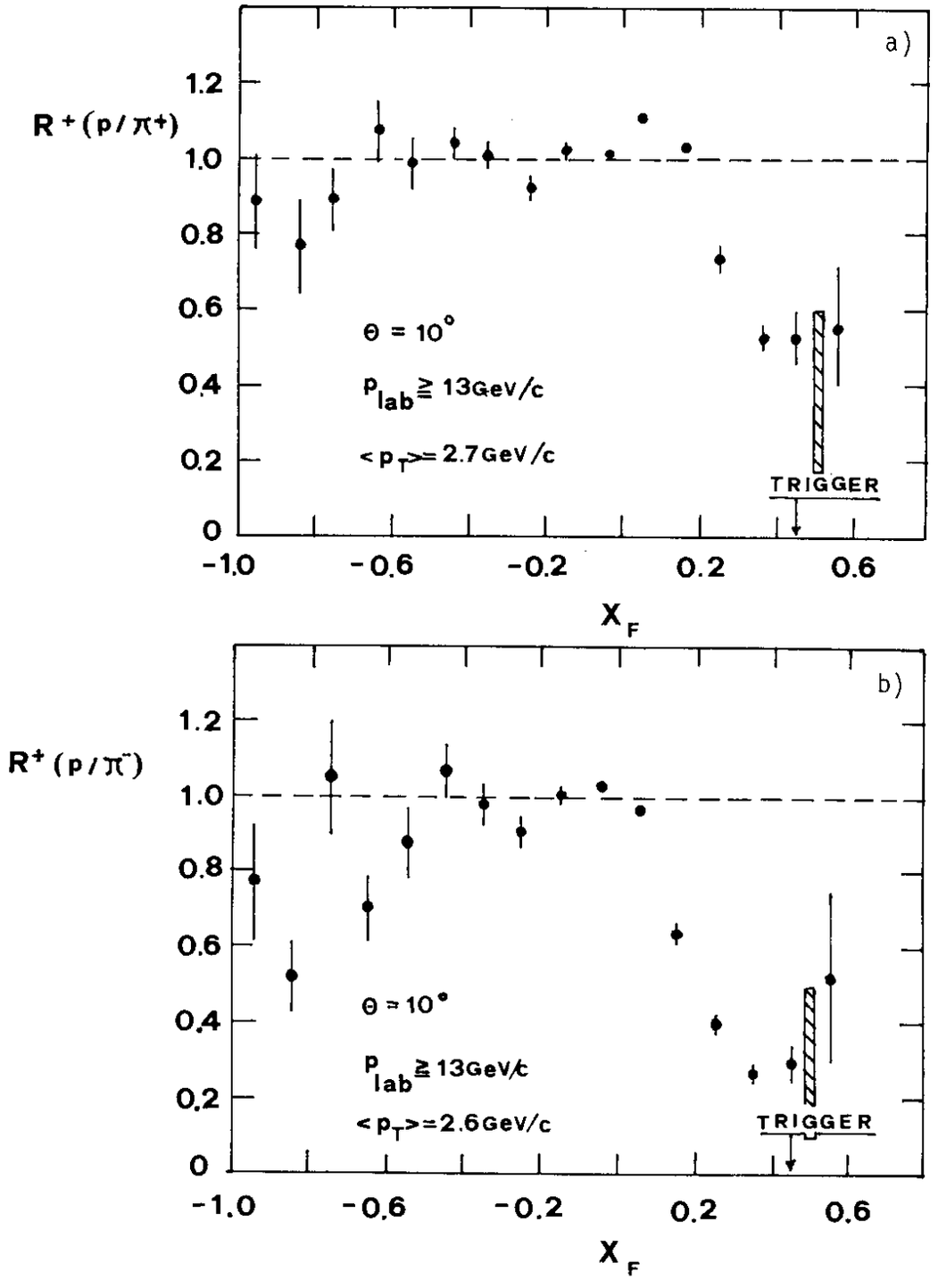
a)
$R^+(p/\pi^+)$
1.2
1.0
0.8
0.6
0.4
0.2
0
$\Theta = 10°$
$p_{lab} \geqq 13 GeV/c$
$< p_T > = 2.7 GeV/c$
TRIGGER
-1.0
-0.6
-0.2
0.2
0.6
X_F
b)
$R^+(p/\pi^-)$
1.2
1.0
0.8
0.6
0.4
0.2
0
$\Theta = 10°$
$p_{lab} \geqq 13 GeV/c$
$< p_T > = 2.6 GeV/c$
TRIGGER
-1.0
-0.6
-0.2
0.2
0.6
X_F

Fig. 34

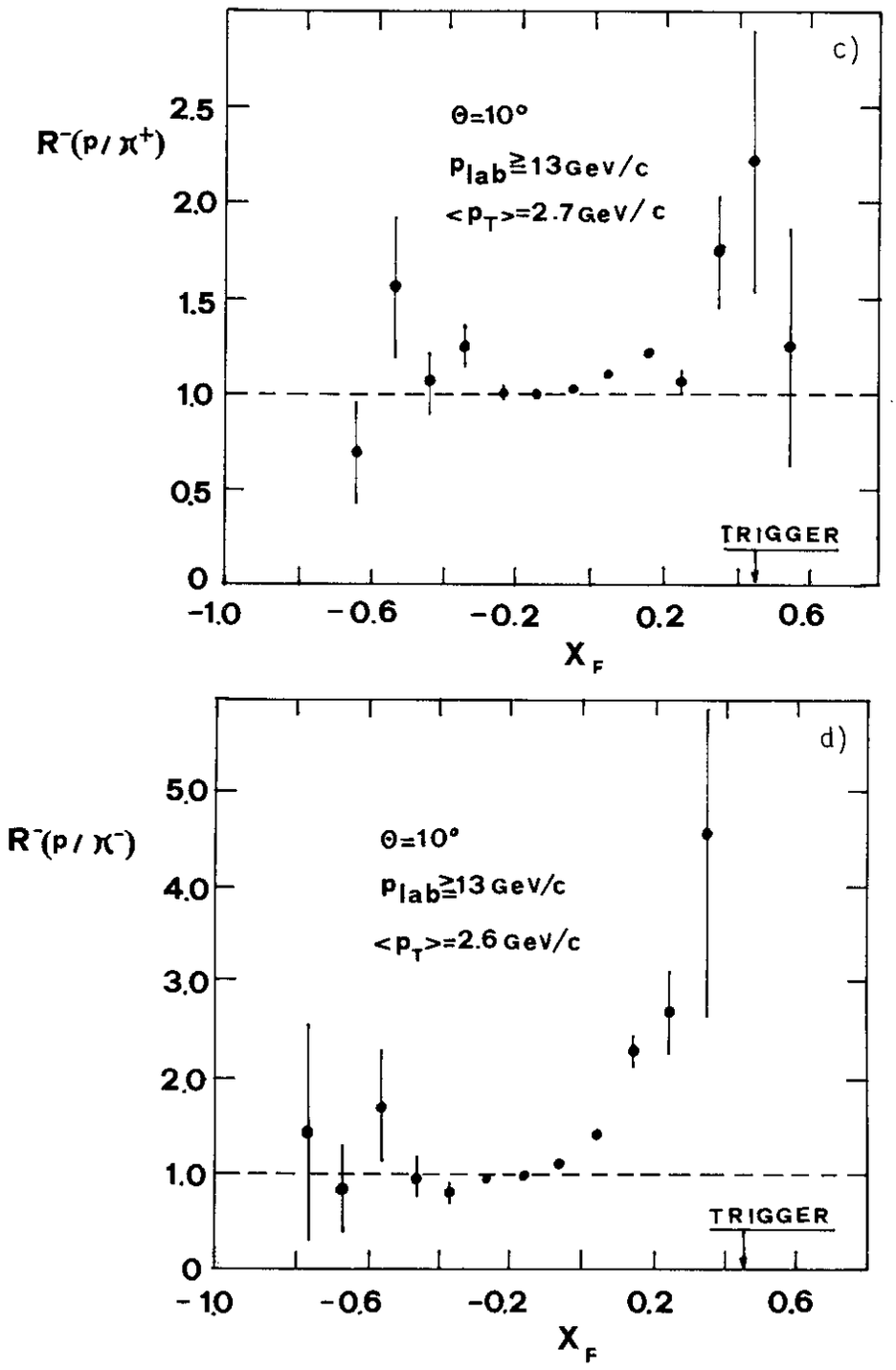
c)
Θ=10°
$p_{lab} \geqq 13$ GeV/c
$\langle p_T \rangle = 2.7$ GeV/c
$R^-(p/\pi^+)$
2.5
2.0
1.5
1.0
0.5
0
TRIGGER
-1.0
-0.6
-0.2
0.2
0.6
X_F
d)
Θ=10°
$p_{lab} \geqq 13$ GeV/c
$\langle p_T \rangle = 2.6$ GeV/c
$R^-(p/\pi^-)$
5.0
4.0
3.0
2.0
1.0
0
TRIGGER
-1.0
-0.6
-0.2
0.2
0.6
X_F

Fig. 34

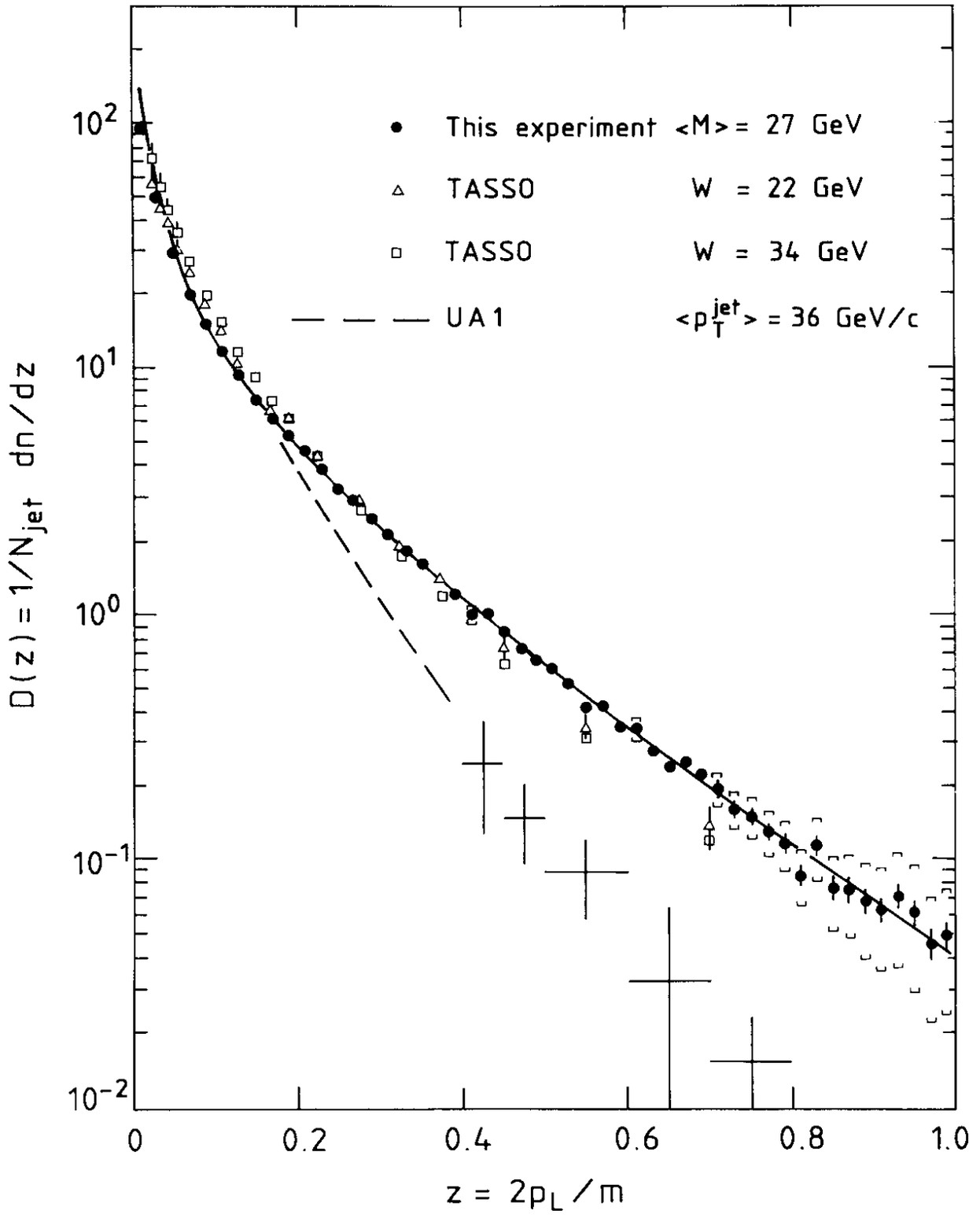
This experiment <M> = 27 GeV
TASSO W = 22 GeV
TASSO W = 34 GeV
UA1 <p_T^jet> = 36 GeV/c
D(z) = 1/N_jet dn/dz
z = 2p_L / m
10^2
10^1
10^0
10^-1
10^-2
0
0.2
0.4
0.6
0.8
1.0

Fig. 35

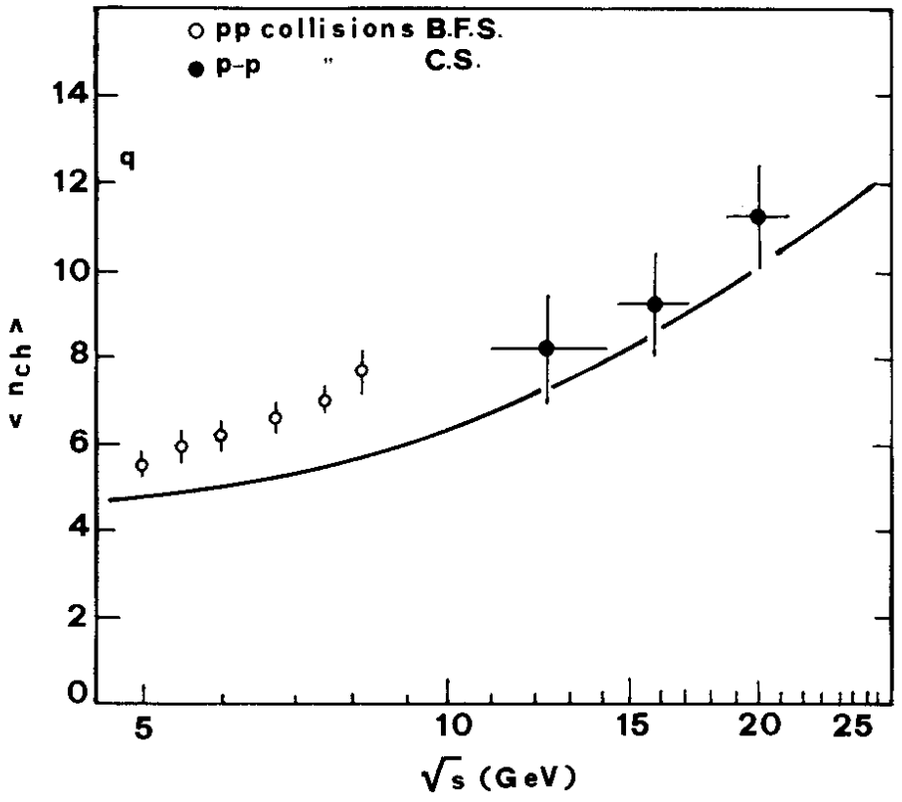

Fig. 36

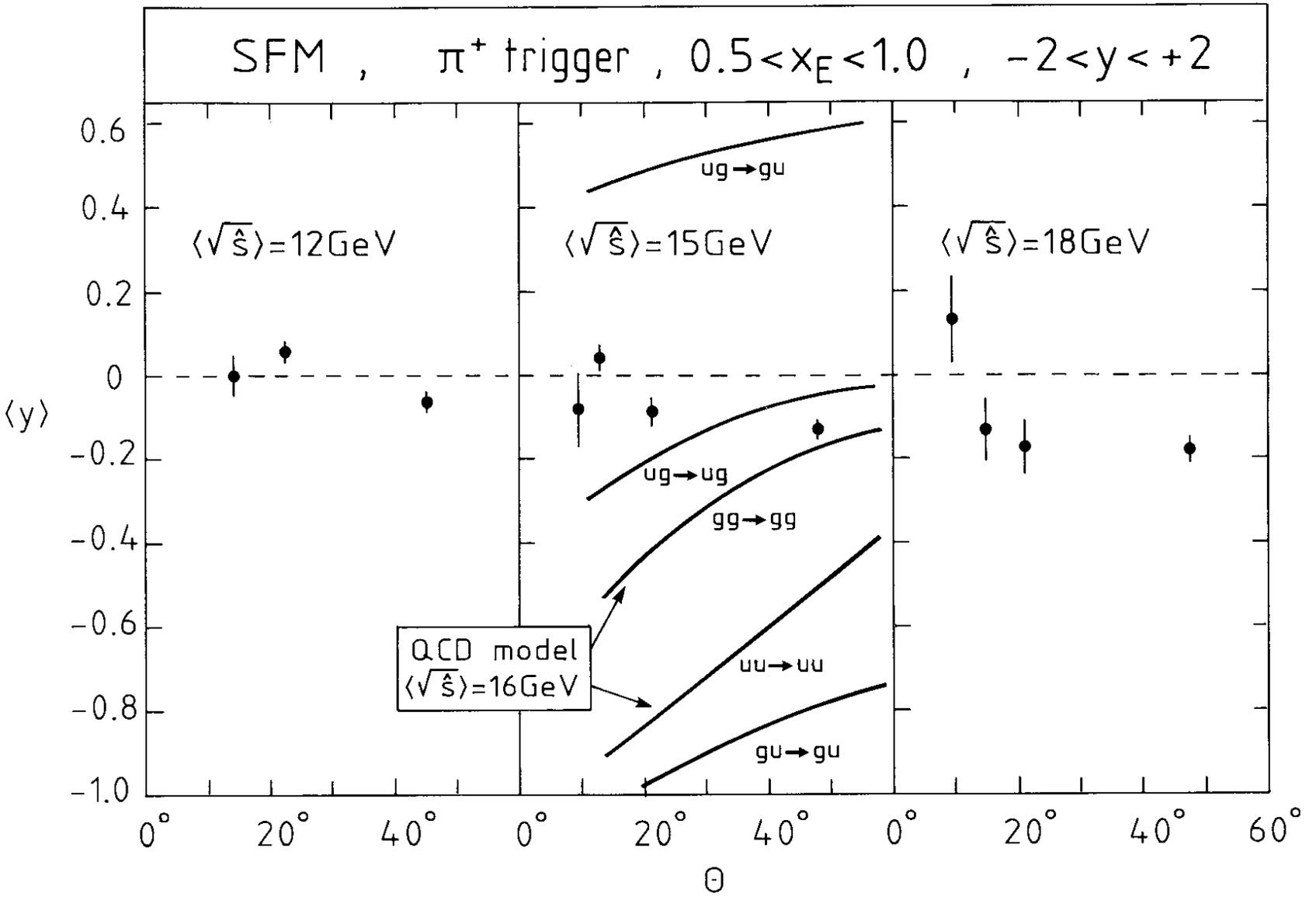
SFM , π+ trigger , 0.5<xE<1.0 , −2<y<+2
⟨√ŝ⟩=12GeV
⟨√ŝ⟩=15GeV
⟨√ŝ⟩=18GeV
ug→gu
ug→ug
gg→gg
uu→uu
gu→gu
QCD model
⟨√ŝ⟩=16GeV
⟨y⟩
Θ
0.6
0.4
0.2
0
−0.2
−0.4
−0.6
−0.8
−1.0
0°
20°
40°
60°

Fig. 37

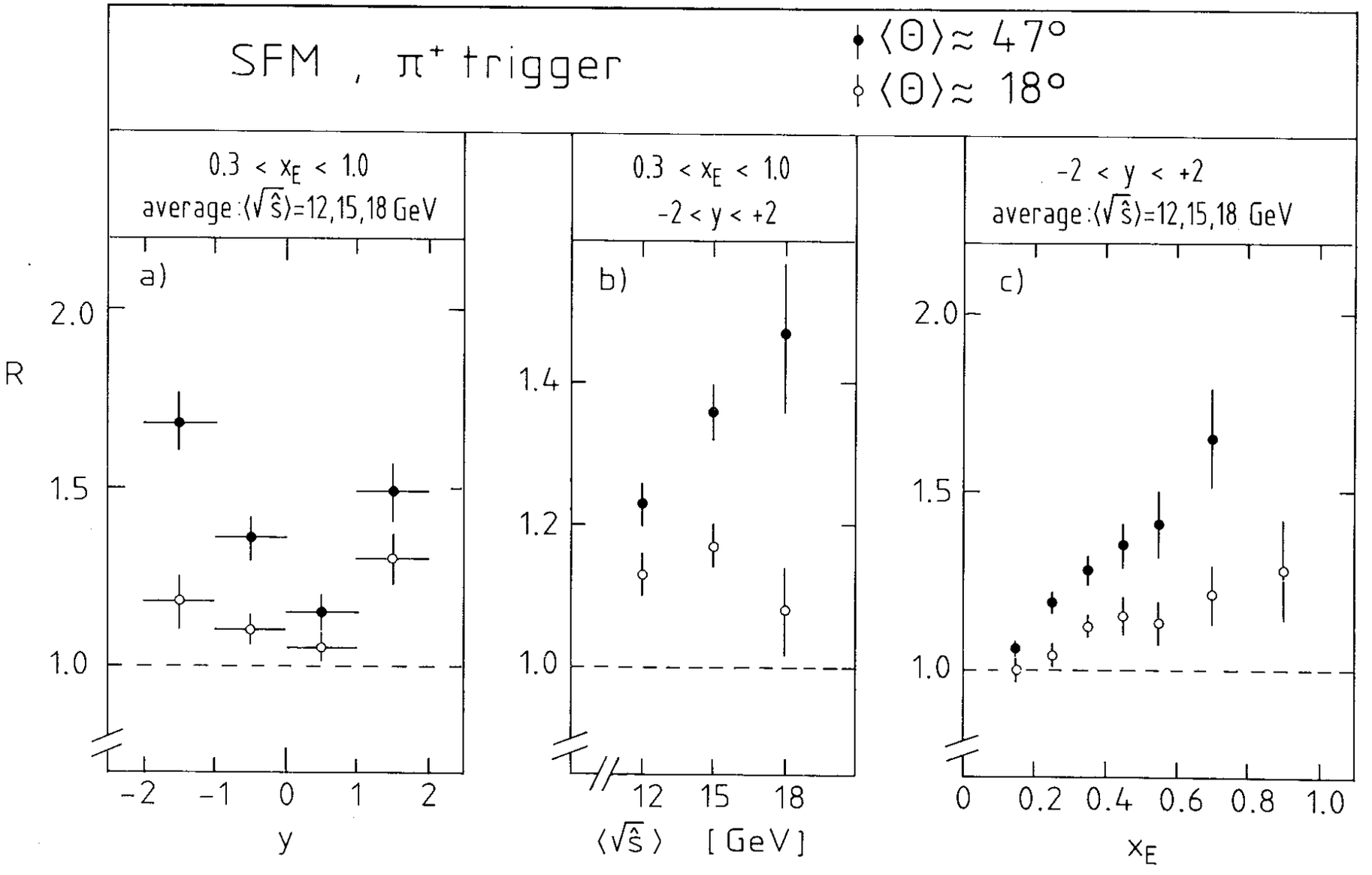
SFM , π+ trigger
⟨Θ⟩≈ 47°
⟨Θ⟩≈ 18°
0.3 < xE < 1.0
average :⟨√ŝ⟩=12,15,18 GeV
a)
b)
0.3 < xE < 1.0
-2 < y < +2
c)
-2 < y < +2
average :⟨√ŝ⟩=12,15,18 GeV
R
2.0
1.5
1.0
1.4
1.2
-2 -1 0 1 2
y
12 15 18
⟨√ŝ⟩ [GeV]
0 0.2 0.4 0.6 0.8 1.0
xE

Fig. 38

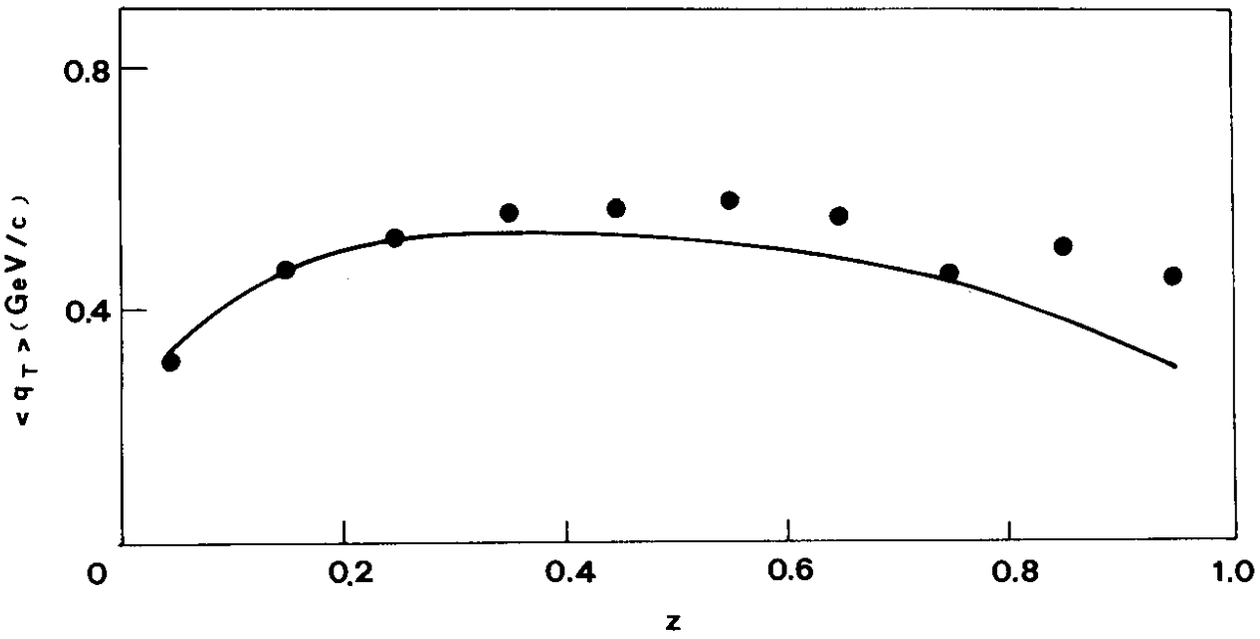

Fig. 39

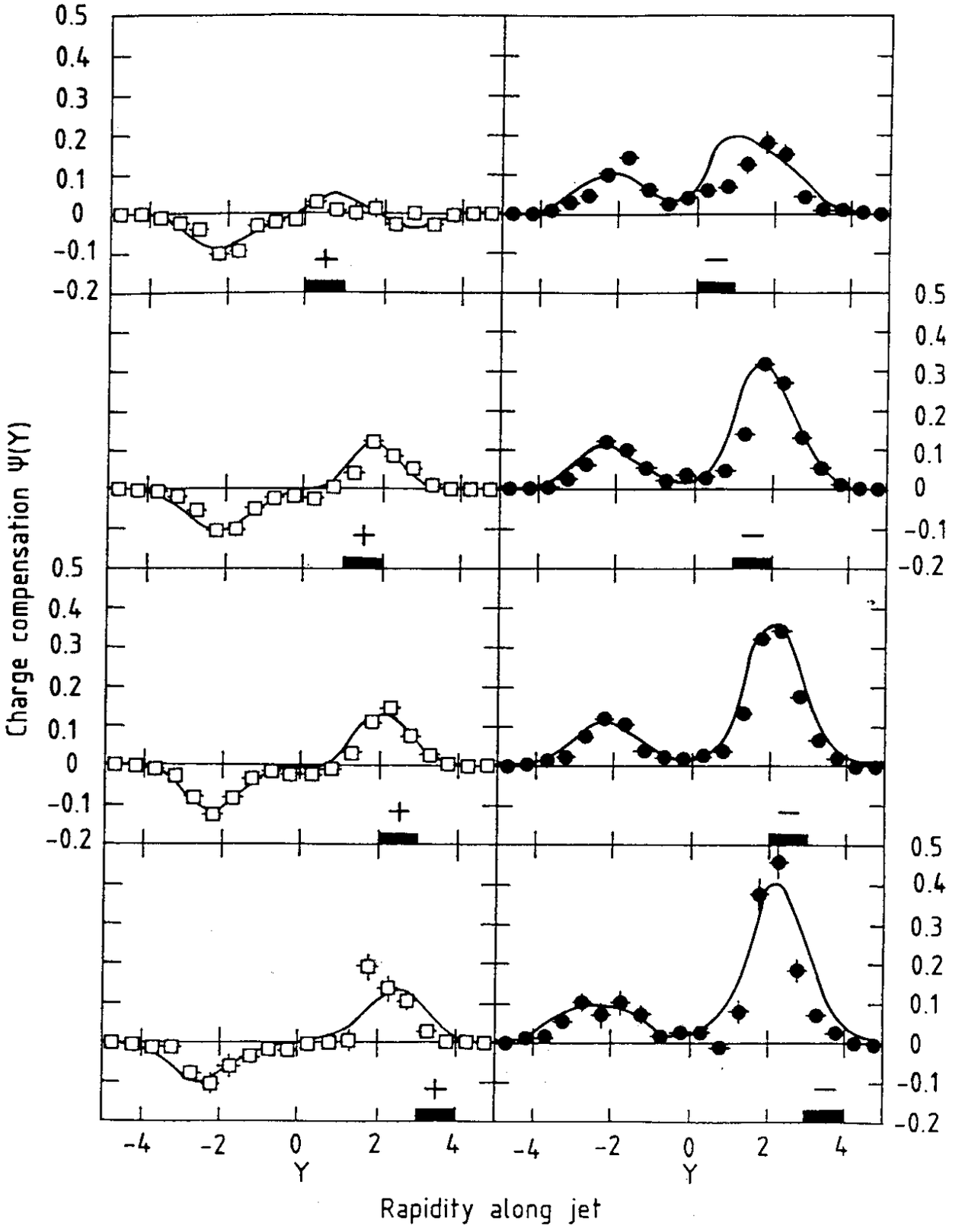
Charge compensation Ψ(Y)
0.5
0.4
0.3
0.2
0.1
0
-0.1
-0.2
+
−
-4
-2
0
2
4
Y
Rapidity along jet

Fig. 40

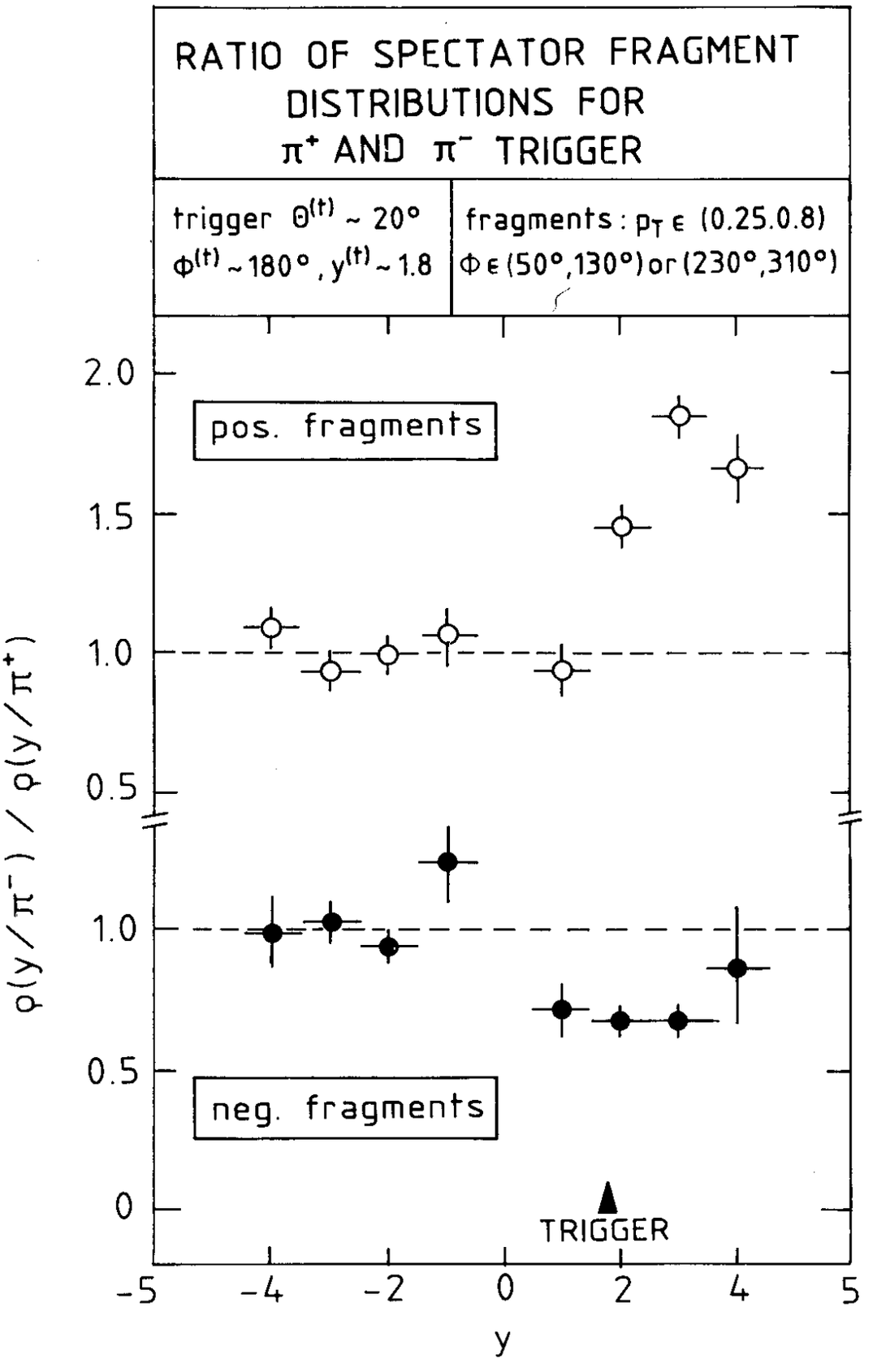
RATIO OF SPECTATOR FRAGMENT DISTRIBUTIONS FOR π+ AND π− TRIGGER
trigger Θ(t) ~ 20°
Φ(t) ~ 180°, y(t) ~ 1.8
fragments: pT ε (0.25.0.8)
Φ ε (50°,130°) or (230°,310°)
pos. fragments
neg. fragments
TRIGGER
ρ(y/π−) / ρ(y/π+)
y
2.0
1.5
1.0
0.5
1.0
0.5
0
-5
-4
-2
0
2
4
5

Fig. 41

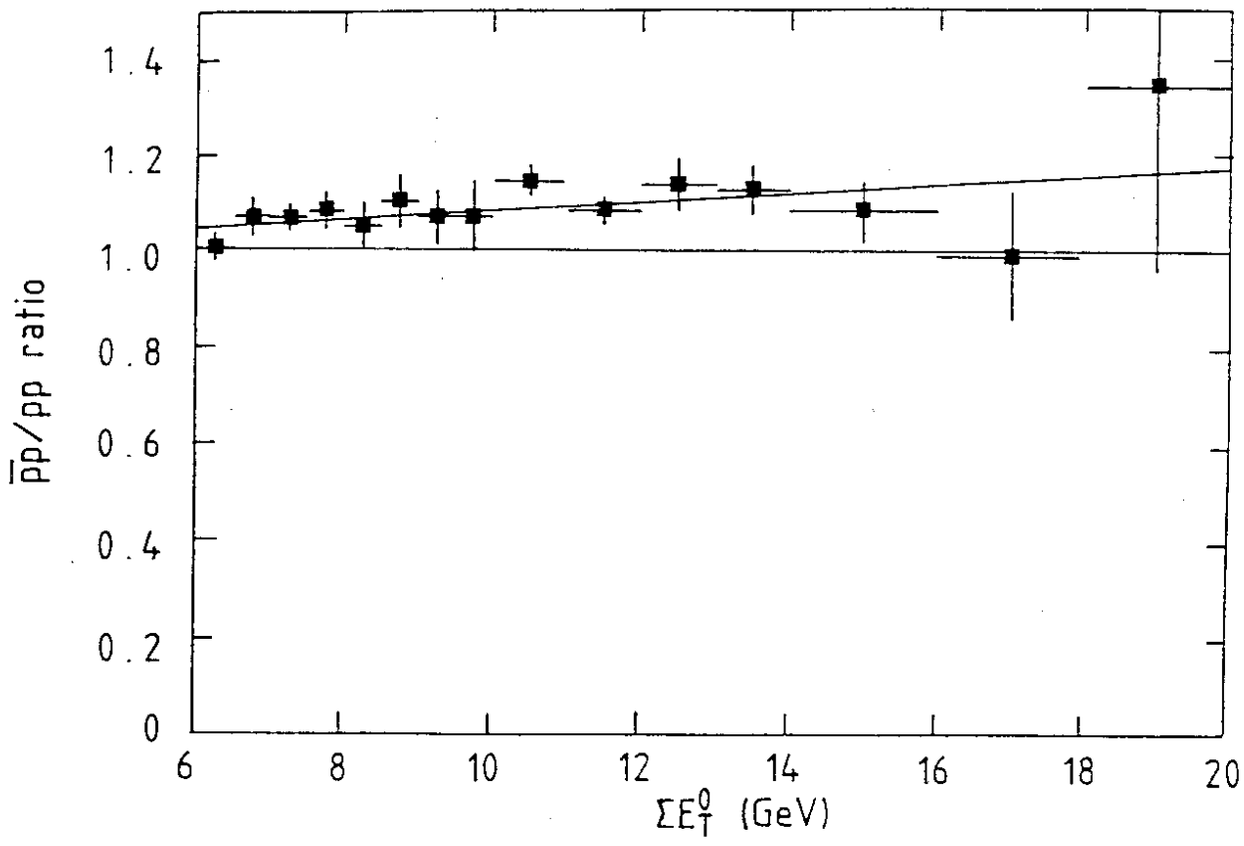
1.4
1.2
1.0
0.8
0.6
0.4
0.2
0
$\bar{p}p/pp$ ratio
6
8
10
12
14
16
18
20
ΣE_T^0 (GeV)

Fig. 42

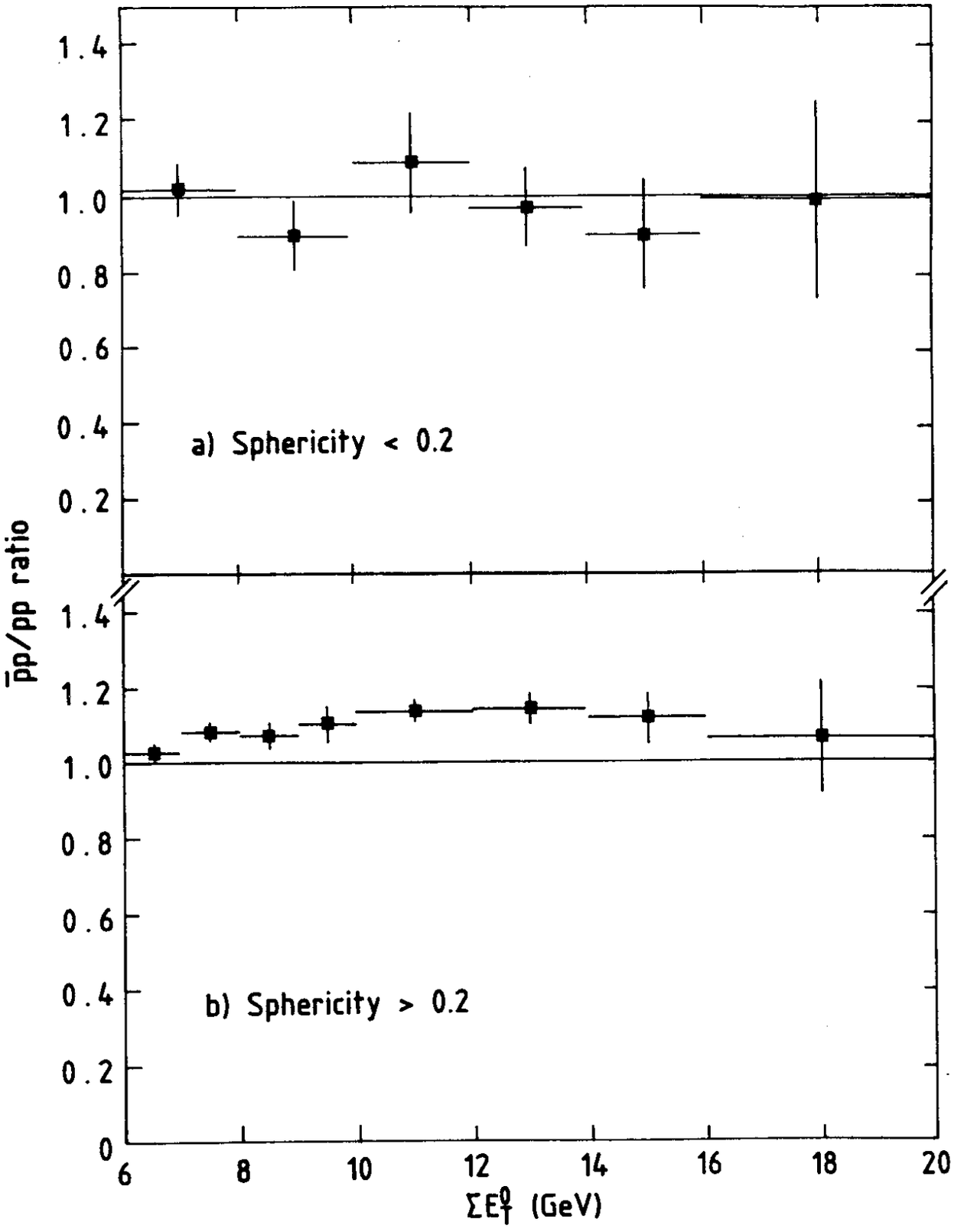
1.4
1.2
1.0
0.8
0.6
0.4
0.2
a) Sphericity < 0.2
1.4
1.2
1.0
0.8
0.6
0.4
0.2
0
b) Sphericity > 0.2
$\bar{p}p/pp$ ratio
6
8
10
12
14
16
18
20
ΣE_T^0 (GeV)

Fig. 43

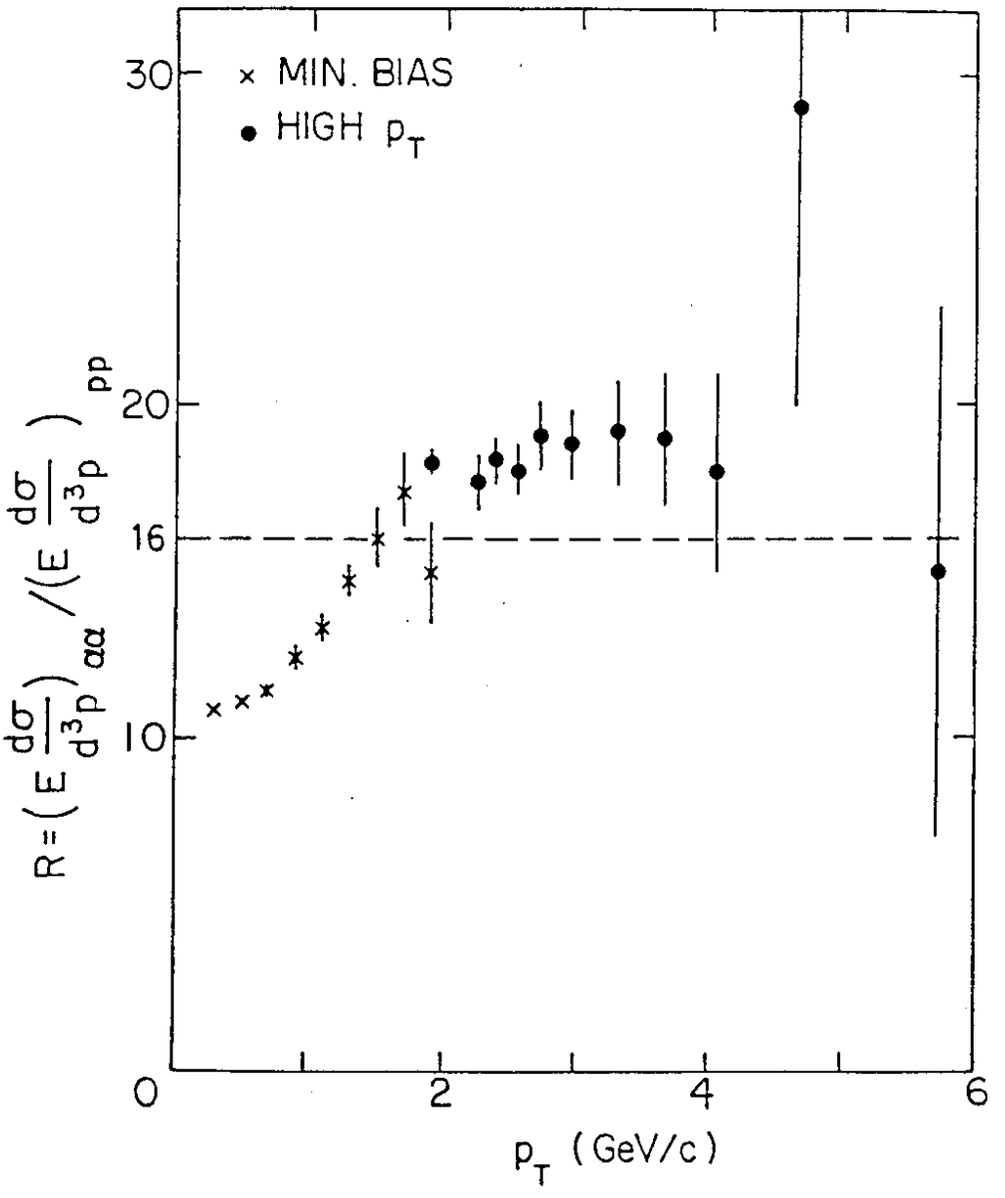
× MIN. BIAS
● HIGH p_T
30
20
16
10
0
2
4
6
p_T (GeV/c)
$R=\left(E\frac{d\sigma}{d^3p}\right)_{aa}/\left(E\frac{d\sigma}{d^3p}\right)_{pp}$

Fig. 44

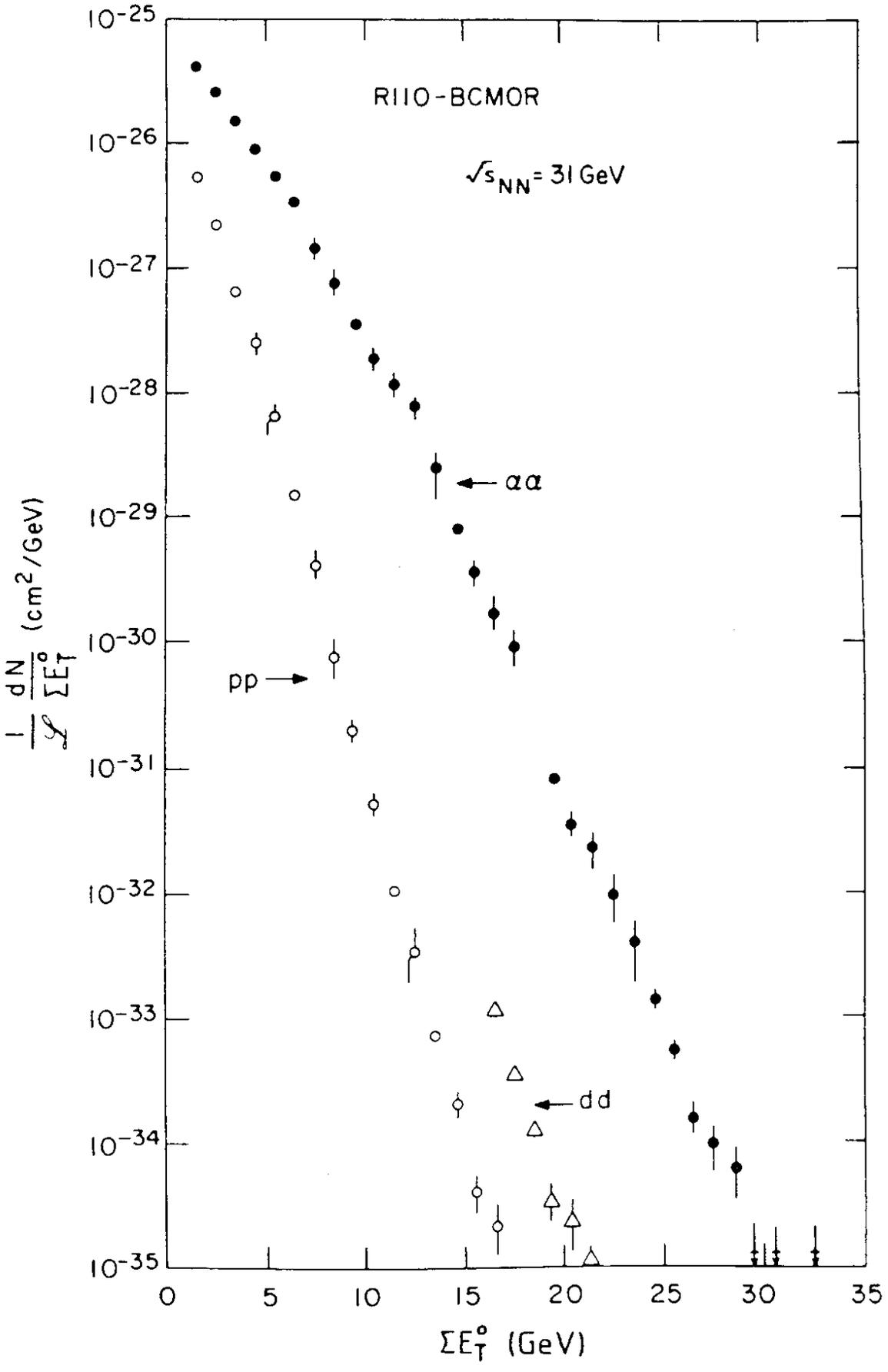
R110-BCMOR
$\sqrt{s_{NN}}$ = 31 GeV
αα
pp
dd
$\frac{1}{\mathcal{L}} \frac{dN}{\Sigma E_T^\circ}$ (cm²/GeV)
ΣE_T° (GeV)
10⁻²⁵
10⁻²⁶
10⁻²⁷
10⁻²⁸
10⁻²⁹
10⁻³⁰
10⁻³¹
10⁻³²
10⁻³³
10⁻³⁴
10⁻³⁵
0
5
10
15
20
25
30
35

Fig. 45